RICE UNIVERSITY

Strongly Interacting One-Dimensional Spinor Quantum Gases

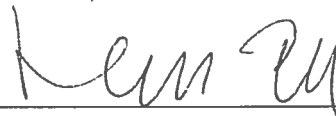by

Li Yang

A Thesis Submitted
in Partial Fulfillment of the
Requirements for the Degree

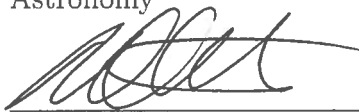## Doctor of Philosophy

Approved, Thesis Committee:

Dr. Han Pu, Chair
Professor, Associate Chair for the
Graduate Program of Physics and
Astronomy

Dr. Matthew Foster
Assistant Professor of Physics and
Astronomy

Dr. Bruce Johnson
Research Professor of Chemistry

Houston, Texas

January, 2019

Abstract

Quantum many-body physics has been studied for many decades. A lot of intriguing phenomena have been observed and theories have been developed. Yet many problems remain unsolved, which is largely due to a lack of general efficient classical computation method. One-dimensional (1D) systems have also drawn much attention over the past few decades. One reason is that many unique strongly correlated quantum phenomena only appear in low dimensions. Another reason is that many exact results can be obtained in 1D for cross benchmarking, such as the results from Bethe Ansatz, Bosonization, Bose-Fermi mapping, etc. In addition, many numerical methods, such as Matrix-Product-State based and Monte Carlo methods, work most efficiently in 1D. In recent years, 1D quantum gases have been realized in many cold atom labs, providing experimental motivation for their studies.

One of the most mysterious assumptions about a system of identical quantum particles is that the wavefunction must be symmetric (for bosons) or anti-symmetric (for fermions). This means that no two fermions can occupy the same state, while multiple occupancy is allowed for bosons. Bosons and fermions are therefore generally very different. But in 1D this distinction could become rather subtle, provided that the bosonic multiple occupancy is suppressed, which can happen if strong repulsion exists between them. However, when considering spin degrees of freedom, things become more complicated. In this work, we develop a generalized Bose-Fermi mapping theory, under which, the charge degrees of freedom is mapped to spinless fermions, while the spin degrees of freedom to an effective spin chain. This mapping works for arbitrary spin, arbitrary trapping potentials, arbitrary spin-dependent interaction potential, and for either spinor bosons or fermions. In the strong inter-

action limit, the wavefunction of the system can be represented by Strong Coupling Ansatz Wavefunctions (SCAWs), which can be mapped to direct products of spinless fermion wavefunctions and spin-chain wavefunctions. Using this mapping technique, we study the dynamics and collective modes of the system. Furthermore, we develop a very efficient method to calculate the one-body density matrix, from which we can calculate the momentum distribution of the system.

To my parents, for supporting me and encouraging me to pursue my dreams.

Acknowledgments

First and foremost, I would like to thank my Ph.D. adviser Dr. Han Pu, for his excellent guidance for me along my Ph.D. research path. I still remember the time I first come to his office in the August of 2013, since then his office become the second place that I visit the most in Brockman Hall beside my own office, for discussing any questions I had. I remember there are many times we discuss about about research details and directions during group meetings, conferences, using emails and video calls, when having lunch, or even when hiking in a national park. Han can always make complicated ideas physically very clear and intuitive, and find interesting and profound view of a theory. During my Ph.D. period, Han gave me full support and resources to establish great collaboration with other distinguished scholars around the globe. Meanwhile, he also give me plenty of freedom and encourage to explore my own research ideas, to learn new things, to develop technical tools I need to get things done, to achieve things I think to be important. Not only has Han been an excellent Ph.D. adviser but has also become a great mentor, a good friend and a spiritual leader for me throughout the past few years, and I still feel there are much more to learn from him. I am truly thankful and grateful for his guidance, intuition and mentorship.

I would like to particularly thank Dr. Xi-Wen Guan, from many discussions with him, I developed several ideas that are very important in my research. I would also like to thank Dr. Matthew Foster, from his courses and through discussions, I learnt a lot of helpful techniques about quantum many-body physics. I would like to thank my collaborators, colleagues, and people who offered me with valuable helps: Liming Guan for working out the effective spin-chain model project together; Lin Dong for

Publications

I hereby declare that except where specific reference is made to the work of others, the contents of this thesis are original and have not been submitted in whole or in part for consideration for any other degree or qualification in this, or any other university.

The following journal publications are (co-)authored and extensively reproduced by the Ph.D. candidate, **Li Yang**, in this dissertation:

[1] **L. Yang**, L. M. Guan, and H. Pu, "Strongly interacting quantum gases in one–dimensional traps", Physical Review A, **91** 043634, (2015).

[2] **L. Yang**, and H. Pu, "Bose–Fermi mapping and a multibranch spin–chain model for strongly interacting quantum gases in one dimension: Dynamics and collective excitations", Physical Review A, **94**, 033614, (2016).

[3] **L. Yang**, and H. Pu, "One–body density matrix and momentum distribution of strongly interacting one–dimensional spinor quantum gases", Physical Review A, **95**, 051602(R), (2017).

Contents

Illustrations

Tables

Chapter 1

Introduction and Outline

1.1 Quantum Gases in One Dimension

Quantum many-body physics has been studied for a long time since the invention of quantum mechanics. Many intriguing phenomenons have been observed in experiments and many theories have been developed, ranging from superfluid, superconducting, Bose-Einstein condensate, to strongly correlated quantum gases and quantum computing. However, quantum many-body problems are hard to solve, mainly due to the fact that there is no efficient classical computation method to directly solve those systems, as computational resource required is usually exponential in system size. On the other hand, in low dimensions, quantum many-body physics has drawn much attention in the past decades. One of the reasons is that in low dimensions, strongly correlated quantum effects will play an important role. By contrast in higher dimensions a lot of systems can be described by fermi liquid theory, which is a mean field theory that approximates many-body systems by non-interacting fermions. Yet another important reason is that many exact results can be obtained in low dimension, which allows benchmarking of different theories. For example in one-dimension, some translational invariant system can be solved by Bethe Ansatz method [3], Bose-Fermi mapping [4] can be used to analyze systems at strong interacting region, low energy effective theories can be constructed by Bosonization [5], etc. And also many numerical methods such as Matrix Product State (MPS) based methods (including Den-

sity Matrix Renormalization Group (DMRG) and Time-Evolving Block Decimation (TEBD)), and Variational Monte Carlo (VMC) methods can help to do benchmarks or inspire new understandings for a system.

With the development of experimental techniques, the physics of quantum many-body systems can be studied in ultra-cold atomic systems in a very clean way. Many strongly correlated quantum many-body phenomenons have been observed. In experiments, neutral atoms can be trapped by lasers, and if the trap has small aspect ratio (very long cigar shapped), the atoms can be regarded as particles moving in a 1D space. And by taking the internal level of the atoms into consideration, the particles can have arbitrary effective spins. Such systems are called spinor quantum gases. In this thesis, we focus on 1D spinor gas. The atoms in cold atom system are dilute. When considering the two-body scattering, if we are interested in low energy scale, we need only consider the s-wave scattering length, which will lead to an effective delta function contact interaction. So we start from the following Hamiltonian for dilute spinor quantum gases, in which there are only contact interactions.

$$H = \underbrace{\sum_{i=1}^{N} \left[-\frac{1}{2} \frac{\partial^2}{\partial x_i^2} + V(x_i) \right]}_{H_f} + \underbrace{\hat{g} \sum_{i<j} \delta(x_i - x_j)}_{H_{\text{int}}}. \tag{1.1}$$

Here we have set $\hbar = m = 1$. H_f is a single particle free Hamiltonian and H_{int} is the contact interaction term. $\hat{g}$ is a matrix acting on the spin state of two particles. The Hamiltonian 1.1 is general such that it is for arbitrary spins, arbitrary spin dependent contact interactions, and arbitrary trapping potentials. There is no constraint on $\hat{g}$ except that it must be symmetric under permutation of two spins: $\mathcal{E}_{i,j} \hat{g} \mathcal{E}_{i,j} = \hat{g}$ ($\mathcal{E}_{i,j}$ is an exchange operator that swap two spins indexed by i and j, Appendix A), because the Hamiltonian must be invariant under any permutation operators, since

we are considering identical particles. The Hamiltonian 1.1 is the starting point of our description of the system. For spinless Bosons, the Hamiltonian 1.1 becomes the Lieb-Liniger model [6] and for spin-1/2 Fermions, it is the Gaudin-Yang model [7, 8].

1.2 Bose-Fermi Mapping

One of the most mysterious assumptions about the quantum many-body world is the identical particle assumption: If the system is composed of many particles of the same kind, and if we use a many-body wavefunction to describe the state of the system, it must be symmetric or anti-symmetric under permutation of the indices of the particles. If the wavefunction is symmetric, the particles are Bosons, and the symmetry allows Bosons to occupy the same spatial position. If the wavefunction is anti-symmetric, the particles are Fermions, which prohibits Fermions from occupying the same spatial position. Usually Bosons and Fermions are very different. However in one-dimension, when double occupancy is suppressed, Bosons and Fermions can be mapped to each other.

Under some special conditions the Hamiltonian 1.1 can be solved by Bethe Ansatz [3, 9] method. But under general conditions, it cannot. The system can be studied from another prespective, for non-interacting Bose or Fermi gases, the eigenstates are easily solved that they are Slater permanents for Bosons and Slater determinants for Fermions. As interaction increases, the system becomes more and more correlated. For weak interaction, there are still approximation method such as effective field theories from Bosonization, or writing the Schrödinger equation into hydrodynamic equation. For strong interaction, usually there is no good theoretical method to study the properties of the system, only numerical methods such as DMRG (TEBD) works well. But there are still many constraints for numerical methods. However, if further

increase the interaction to infinity, things sometimes become simpler. At infinite interaction, there is a theory showing spinless Bosons can be mapped to spinless Fermions [4, 10]. Since spinless Fermions do not feel any contact interaction, it is much easier to solve, so Bose-Fermi mapping acts as an alternate effective method for solving infinite interaction systems. However, when considering spin degrees of freedom, things become more complicated, the spin degrees of freedom will interplay with Boson or Fermion statistics. In this thesis, we will generalize the spinless particle Bose-Fermi mapping to spinor cases, and also extend beyond infinite interaction to arbitrary finite interaction strength.

1.3 Numerical Methods

1.3.1 MPS based methods

There are many numerical methods to solve 1D strongly correlated quantum many-body systems. Among them MPS based methods are powerful for numerically solving most of the 1D systems. The MPS methods cut the system at every link, by flattening the indices for physical spins[1] to the left and right of the cut, the wavefunction can be written into a matrix. After performing a singular value decomposition of this matrix, where the singular values are just the square roots of the eigenvalues of the density matrices of the left and right subsystems[2], truncate the singular values to a certain cutoff. Performing this singular value truncation for every link, the original wavefunction can be written into a MPS form, which largely (exponentially) compresses the information of the original wavefunction. The MPS based methods by

---

[1]Or any other local degrees of freedom.

[2]It can be proved that the density matrices of the left and right subsystems have the same eigenvalues.

definition works for lattice systems, and it will work well if the entanglement spectrum at every link of the system decays fast enough, thus a finite truncation is reasonable. To use MPS methods on Hamiltonian 1.1, we discretize it into the following form:

$$H^s = -t \sum_{\sigma,i} \left(f_{i\sigma}^\dagger f_{i+1\sigma} + h.c. \right) + \sum_i \mu_i n_i + \sum_{i,\alpha,\beta,\gamma,\delta} \langle \alpha\beta | \hat{U} | \delta\gamma \rangle f_{i\alpha}^\dagger f_{i\beta}^\dagger f_{i\gamma} f_{i\delta} \,, \quad (1.2)$$

where $f_{i\sigma}^\dagger$ and $f_{i\sigma}$ are creation and annihilation operators on site i for spin σ, $n_i = \sum_\sigma f_{i\sigma}^\dagger f_{i\sigma}$ is the local density operator on site i. The parameters in Hamiltonian 1.2 is obtained by discretization

$$t = \frac{1}{2a^2}, \ \mu_i = V(ia) + \frac{1}{a^2}, \ \hat{U} = \frac{\hat{g}}{2a} \,. \quad (1.3)$$

MPS methods can be directly applied on Hamiltonain 1.2. We have studied both ground states and dynamics, and found good agreements with theoretical results.

1.3.2 Variational Monte Carlo methods

Many quantum many-body systems can be solved by Variational Monte Carlo (VMC) methods. The VMC method is quite general such that given a variational wavefunction, the parameters can be optimized by minimizing the energy functional stochastically. In the literature, variational wavefunctions are usually proposed through physical understandings of a particular system. For the 1D spinor quantum gases system, we can use Strong Coupling Ansatz Wavefunctions (Chapter 4) as variational wavefunctions. On the other hand, recent Deep Learning has been very successful in many areas. Those success involves representing multi-dimensional functions using Deep Neural Networks (DNNs) with a huge number of parameters. One of the important reasons for the success is the development of novel computer architectures [11] such as GPUs that can perform computations for large neural networks in a distributed

way. Another reason is the development of various DNN architectures with suitable representational power and efficient optimizing algorithms. The DNNs were able to automatically learn features from multi-dimensional data, which can be understood as a kind of machine intelligence. So it is natural to represent quantum many-body wavefunctions using DNNs, which are essentially multi-dimensional functions, to see what features DNNs can extract. In this thesis, we also explore using DNNs for solving spinor quantum gases. Especially at strong coupling region, the system can be described by an inhomogeneous effective spin-chain model. If the interaction is spin-independent, it is an inhomogeneous SU(N) spin-chain model. With an off-policy VMC algorithm, we are able to take advantage of the distributed hardwares and use DNNs to represent the ground state of such spin-chain models.

Chapter 2

Generalized Bose-Fermi Mapping

Strongly interacting many-body systems exhibit rich physics, but in general pose as tremendous theoretical challenges. Under certain circumstances, a system can be mapped into another one much more amenable to theoretical study. The Bose-Fermi mapping is one such example [4]. It maps a system of one dimensional (1D) spinless bosons with infinite repulsive two-body contact interaction to a system of spinless non-interacting fermions. The eigenstates are mapped by

$$\Psi_B(x_1, x_2, ..., x_N) = \sum_{P \in S_N} P(\Psi_F(x_1, x_2, ..., x_N)\theta^1(x_1, x_2, ..., x_N)), \qquad (2.1)$$

where Ψ_F is the free Fermion wavefunction, Ψ_B is the corresponding hardcore Boson wavefunction. θ^1 is a sector function (i.e., generalized Heaviside step function) of spatial coordinates and can be written into the following form:

$$\theta^1 = \theta(x_2 - x_1)\theta(x_3 - x_2)\cdots\theta(x_i - x_{i-1})\theta(x_{i+1} - x_i)\cdots\theta(x_N - x_{N-1}), \qquad (2.2)$$

whose value is one in spatial sector $x1 < x2 < ... < xN$, and zero in any other spatial sectors. P is a permutation operator, for conventions of permutation operator acting on spatial wavefunctions, see Appendix A. $(-1)^P$ is parity of the permutation operator. The idea behind it is that for N identical particles, the wavefunction in one spatial sector $x_1 < x_2 < ... < x_N$ contains complete information about the total wave function. Due to the infinite interaction, the relative wave function between two identical bosons must vanish when $x_i = x_j$, which mimics the quantum statistics

between two identical fermions. Such system has been experimentally realized using ultracold atoms [12–14]. This mapping for spinless particles at infinite interaction can be easily generalized to spinful cases, which is summarized in Section 2.1, where the Strong Coupling Ansatz Wavefunction (SCAW) is defined. This mapping was later generalized to finite interaction strength by Cheon and Shegehara [15,16] who mapped a system of s-wave contact interacting spinless bosons with interaction strength g to a system of p-wave short-range interacting spinless fermions with interaction strengh $-1/g$. This idea was further developed by Girardeau and Olshanii [17,18] who showed that 1D spinor Fermi gas and Bose gas can be mapped into each other, where the s-wave interaction (e.g., V_s) in one is mapped to the p-wave interaction (e.g., V_p) in the other. This mapping can be understood as follows. The even relative spatial wavefunction under V_s and the odd relative spatial wave function under V_p satisfy exactly the same boundary condition: $\lim_{x_{ij}\to 0^+} g\psi(x_{ij}) = 2\psi'(x_{ij})$. The key idea behind this mapping is a single particle duality, which will be discussed in Section 2.2 in detail.

Motivated by these past works, in this chapter we present a different, but related, mapping as follows: A 1D spinor gas, either Bosonic or Fermionic, interacting with s-wave contact two-body interaction, can be mapped to the direct product of a spinless Fermi gas and a spin-chain system. In this dissertation, we call this later direct product system Spin-Charge Separated Representation (SCSR). We emphasize that this mapping is exact and valid for arbitrary values of $g > 0$. However, it is particularly useful for strongly interacting systems with large g, for which the spatial wave function of the mapped system is that of a weakly interacting p-wave spinless Fermi gas, which can be calculated perturbatively. In Chapter 3, we will discuss the results of the perturbation theory, from which effective spin-chain models can be derived to

describe the physics around infinite interaction.

2.1 Infinitely Interacting Spinor Quantum Gases

Before discussing the generalized Bose-Fermi mapping for finite interaction strength for a spinor quantum gas with arbitrary spin, we first discuss the physics at infinite interaction point, which serves as a basis for the analysis of large but finite interaction strength. For spinor quantum gases at infinite contact interaction, any two particles with any spins can not occupy a same spatial position. And since we are considering contact interactions in Hamiltonian 1.1, any particle if it is not occupying a same position with other particles, then it it not feeling any contact interaction, which means it is moving freely. Now consider the spatial sector of θ^1, since the wavefunction of identical particles should be either symmetric or anti-symmetric, the many-body wavefunction in one spatial sector, for example θ^1, has the complete information of the many-body wavefunction in other spatial sectors. This is true for arbitrary spin cases, because after a permutation operator acting on the wavefunction, it will inevitably change any set of spatial coordinates from one spatial sector to another. At the boundary of this spatial sector θ^1, the wavefunction should vanish.

$$\Psi(x_1, x_2, ..., x_N)_{x_i=x_j} = 0, \forall i, j \tag{2.3}$$

Within the boundary, the wavefunction should satisfy the free schrodinger equation.

$$H_f \Psi = E\Psi, \tag{2.4}$$

Where H_f is the free Hamiltonian in Eq. (1.1). Eq. (2.3) and Eq. (2.4) forms the boundary condition and eigen equation for the many-body problem in spatial sector θ^1. And they will uniquely decide any eigenfunction's value in spatial sector θ^1,

and hence will decide the whole eigenfunction. Now the question is how to solve the eigenfunctions satisfying the eigen equation Eq. (2.4) and boundary condition Eq. (2.3). Actually slater determinants constructed by the single particle eigenstates of H_f is just designed for the solution, since they naturally satisfy the boundary condition Eq. (2.3), and by definition they will also satisfy the eigen equation Eq. (2.4). Actually for both spinless Bosons or Fermions under infinite interaction, slater determinant is the solution of Eq. (2.3) and Eq. (2.4) in spatial sector θ^1. For spinless Fermions, slater determinants are actually full eigenfunctions. For spinless Bosons the full eigenfunctions are obtain by symmetrization of slater determinants as done in Eq. (2.1).

When considering spins, we should extend the Hilbert space also including spins. We first constrain H_f to be spin independent (For a discussion of spin-dependent single particle terms, see Appendix F). For this case, we can write the eigenstates in θ^1 spatial sector in the following form.

$$\Psi^1 = \varphi^1(x_1, x_2, ..., x_N)\chi(\sigma_1, \sigma_2, ..., \sigma_N). \tag{2.5}$$

Where χ is an arbitrary spin wavefunction, such that the spin state is represented by $|\chi\rangle = \sum_{\sigma_1,\sigma_2,...,\sigma_N} \chi(\sigma_1, \sigma_2, ..., \sigma_N) |\sigma_1, \sigma_2, ..., \sigma_N\rangle$. And $\varphi^1 = \varphi\theta^1$ is a free fermion eigenfunction (slater determinant) of H_f mentioned above in θ^1 spatial sector. For the full wavefunction for infinitely interacting spinor gases in all spatial sectors, we only need to do a symmetrization or anti-symmetrization.

$$\Psi = \sum_{P \in S_N} (\pm)^P P(\Psi^1). \tag{2.6}$$

Where the permutation operator P now acting on the indices of both spatial coordinates (x_i) and spin coordinates (σ_i), for our conventions about permutation

operators acting on spatial and spin wavefunctions, see Appendix A. $(-1)^P$ is the parity of the permutation operator. In this thesis, Eq. (2.6) is called Strong Coupling Ansatz Wavefunction (SCAW), although it represents the exact eigenstates for infinitely interacting spinor quantum gases. We will discuss the properties of SCAW in Chapter 4. It it easy to show that Eq. (2.6) is an eigenstate satisfying boundary condition Eq. (2.3) and eigen equation Eq. (2.4), so it is an eigenfunction of the infinitely interacting spinor quantum gas (1.1). Note that SCAW in one spatial sector such as θ^1 is a direct product form of spatial and spin wavefunctions, but for the whole wavefunction, spatial and spin wavefunctions are entangled. Another note is that since any spin state will allow Eq. (2.6) to be an eigenstate of the infinitely interacting spinor quantum gas, the eigenstates have d^N fold degeneracy[1], where d is the number of spin component for the spinor quantum gas.

2.2 A Single Particle Hamiltonian Duality

In the following sections of this chapter, we discuss the generalize Bose-Fermi mapping for arbitrary interaction strength. Before discussing the generalized Bose-Fermi mapping theory for many particles, first consider a single particle Hamiltonian duality problem, which will play an essential role in the generalize Bose-Fermi mapping theory for arbitrary cases. Consider the following single particle Hamiltonian, a particle moving in an arbitrary symmetric potential $V(x) = V(-x)$ with a Dirac delta function barrier.

$$H^e = -\frac{1}{2}\frac{\partial^2}{\partial x^2} + V(x) + g\delta(x), , \tag{2.7}$$

---

[1]Here we ignore spatial state degeneracy, for discussions about spatial state degeneracy, see Section. 3.4.

Note that since H^e has parity symmetry, the eigenstates can be separated into even and odd subspaces. For odd eigenstates, the $\delta(x)$ barrier potential has no effect, so we first focus on the nontrivial even eigenstates. This Hamiltonian can be solved by using the boundary condition at the $\delta(x)$ barrier:

$$\phi'(0^+) = -\phi'(0^-) = g\phi(0), , \tag{2.8}$$

where $\phi'(x)$ is the derivative of $\phi(x)$ over x, and the eigen equation on the left and right of the barrier is

$$\left[-\frac{1}{2}\frac{\partial^2}{\partial x^2} + V(x) \right] \phi(x) = E\phi(x). \tag{2.9}$$

With the solution of Eq. (2.9) satisfying the boundary conditon Eq. (2.8), we can obtain all the even eigenstates of Hamiltonian 2.7.

Now consider another single particle hamiltonian:

$$H^o = -\frac{1}{2}\frac{\partial^2}{\partial x^2} + V(x) - \frac{1}{g}\frac{\overleftarrow{\partial}}{\partial x}\delta(x)\frac{\overrightarrow{\partial}}{\partial x}, \tag{2.10}$$

where $\frac{\overleftarrow{\partial}}{\partial x}$ and $\frac{\overrightarrow{\partial}}{\partial x}$ are differential operators acting on the left and right wavefunctions, they are meaningful only when calculating the matrix elements of the Hamiltonian. Same as H^e, H^o also has parity symmetry. For even states, the p-wave singular operator $\frac{\overleftarrow{\partial}}{\partial x}\delta(x)\frac{\overrightarrow{\partial}}{\partial x}$ will have no effects, since $\frac{\overrightarrow{\partial}}{\partial x}$ operators will transform an even state to a odd state and $\delta(x)$ will vanish it. Let $\phi_m(x)$ and $\phi_n(x)$ be two odd eigenstates of H^o with eigenenergies E_m and E_n, consider the following integral

$$\int_{0^-}^{0^+} dx\phi_m(x)\left[-\frac{1}{2}\frac{\partial^2}{\partial x^2} + V(x) - \frac{1}{g}\frac{\overleftarrow{\partial}}{\partial x}\delta(x)\frac{\overrightarrow{\partial}}{\partial x} \right]\phi_n(x) = \int_{0^-}^{0^+} dx\phi_m(x)E_n\phi_n(x) . \tag{2.11}$$

Using the fact that $\phi_m(x)$ and $\phi_n(x)$ are odd functions, together with integrate by parts, the above integration can be simplified to

$$\phi_m(0^+)\phi'_n(0) - \frac{1}{g}\phi'_m(0)\phi'_n(0) = 0, . \tag{2.12}$$

Note that $\phi_{m,n}$ may not continuous, but since $\phi_n(x)$ is odd, $\phi_n'(0)$ is well defined as $\phi_n'(0) = \phi_n'(0^+) = \phi_n'(0^-)$. After factoring out the $\phi_n'(0)$ term, we can arrive at a similar boundary condition as Eq. (2.8),

$$\phi'(0) = g\phi(0^+) = -g\phi(0^-) \,, \tag{2.13}$$

for any eigenstate ϕ. Comparing with Eq. (2.8) and Eq. (2.13), for $x > 0$, the boundary conditions are the same, for $x < 0$, they differ by a sign. This is because we are considering the even eigenstates of H^e and the odd eigenstates of H^o, and they dual to each other. And also to the left and right of the p-wave singular potential, $\phi_{m,n}$ satisfy the same eigen equation 2.9, which means the eigenstates and eigenenergies have one-to-one correspondence for H^e and H^o by

$$\phi^o(x) = \text{sign}(x)\phi^e(x). \tag{2.14}$$

For odd eigenstates of H^e and even eigenstates of H^o, they are trivially dual to each other, and Eq. (2.14) still holds.

For the odd Hamiltonian H^o, there are some pathological behavior for the differential operator $\frac{\partial}{\partial x}$ acting a discontinuous function $\phi^o(x)$, for now, simply regard the differentiation is acting at 0^+ or 0^-. We will discuss this with more detail in Section 2.5. And a illustration of the duality of the ϕ^o and ϕ^e wavefunctions are in Fig. 2.1. Here we want to mention that if define the derivatives at $x = 0$ as $\partial_{x=0} = \partial_{x=0^+} = \partial_{x=0^-}$, the duality between 2.7 and 2.10 can also be proved using single particle Green's function method (Appendix D).

2.3 Generalized Bose-Fermi Mapping for Two Particles

The single particle Hamiltonian duality in section 2.2 is a building block for the generalized Bose-Fermi mapping theory for arbitrary cases. Before discussing many
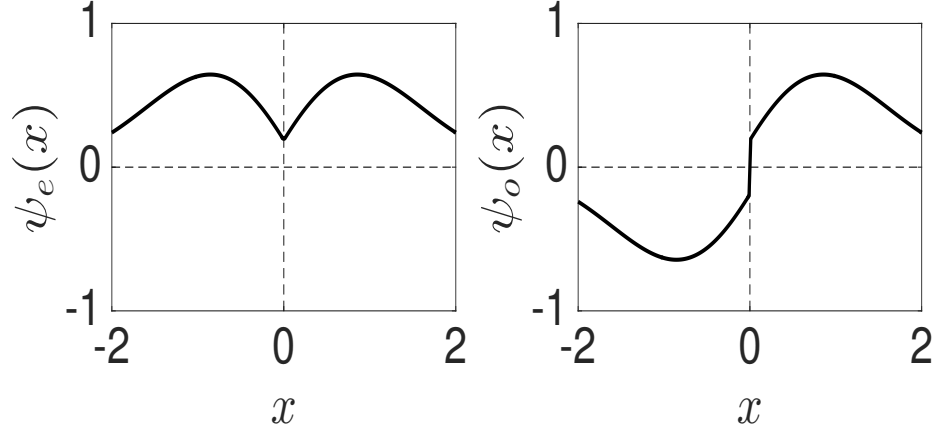
Figure 2.1 : The duality of the ϕ^o and ϕ^e single particle wavefunctions as discussed in Section 2.2. For many-body wavefunctions, this duality corresponds to relative wavefunctions around the boundaries of the θ^1 spatial sector of original (anti-)symmetric wavefunctions and that of spin-charge separated wavefunctions. Any anti-symmetric spatial wavefunctions, although discontinuous at spatial boundaries, can be expanded by slater determinants.

particle cases, first consider the case of two identical particles with arbitrary spin. The first quantized Hamiltonian in the most general form is:

$$H = \sum_{i=1,2} \left[-\frac{1}{2} \frac{\partial^2}{\partial x_i^2} + V(x_i) \right] + \hat{g}\delta(x_1 - x_2). \tag{2.15}$$

Where $\hat{g}$ is the interaction matrix that acting on the spins states of two particles. By diagonalizing $\hat{g}$, we can fix the spin states to an eigenstate of $\hat{g}$, which allows us to substitute $\hat{g}$ with the corresponding eigenvalue g. And the full wavefunction can be written as

$$\Psi(x_1, x_2, \sigma_1, \sigma_2) = \Phi(x_1, x_2)\chi(\sigma_1, \sigma_2). \tag{2.16}$$

Since it is a two identical particle system, the Hamiltonian 2.15 should be invariant under permutation of the two particles. Since $\delta(x_1 - x_2)$ is invariant under the permutation, $\hat{g}$ must also be invariant. Therefore χ can have a fixed parity. If we choose χ with a fixed parity, $\Phi(x_1, x_2)$ can also have a fixed parity, since the full eigen

wavefunction Ψ can have a fixed parity.

First consider spinor Fermions, where Ψ should be anti-symmetric. In this case, only when Φ is symmetric, it can feel the delta function interaction, which means χ must be anti-symmetric. Due to the form of the Hamiltonian 2.15, we can separate Φ into center of mass motion and relative motion.

$$\Phi(x_1, x_2) = \Phi_c(\frac{x_1 + x_2}{2})\Phi_r(x_1 - x_2), \tag{2.17}$$

where the relative motion is governed by the relative Hamiltonian,

$$H_r^e = 2\left(-\frac{1}{2}\frac{\partial^2}{\partial x^2} + \frac{g}{2}\delta(x)\right). \tag{2.18}$$

Using the single particle Hamiltonian duality discussed in Section 2.2, we can transform the relative Hamiltonian 2.18 to Hamiltonian:

$$H_r^o = 2\left(-\frac{1}{2}\frac{\partial^2}{\partial x^2} - \frac{2}{g}\frac{\overleftarrow{\partial}}{\partial x}\delta(x)\frac{\overrightarrow{\partial}}{\partial x}\right). \tag{2.19}$$

Note here g is an eigenvalue of $\hat{g}$ with eigenstate χ anti-symmetric. For symmetric χ, the relative spatial wavefunction Φ_r is odd, the original relative Hamiltonian has no delta barrier, for which we map the original relative Hamiltonian identically to the new Hamiltonian. Put the above together, we can map the full two spinor fermions Hamiltonian 2.15 to a Hamiltonian with Hilbert space constraint that no matter what parity the spin state has, the spatial state has odd parity. The new Hamiltonian has the following form:

$$H = \sum_{i=1,2}\left[-\frac{1}{2}\frac{\partial^2}{\partial x_i^2} + V(x_i)\right] - \frac{4\hat{P}^a}{\hat{g}}\frac{\overleftarrow{\partial}}{\partial x_{12}}\delta(x_{12})\frac{\overrightarrow{\partial}}{\partial x_{12}}, \tag{2.20}$$

where $\hat{P}$ is the projection operator acting on the spin states of the spins, such that $\hat{P}^a/\hat{g}$ is nonzero only when the spin state is anti-symmetric (odd parity). As discussed

earlier, $\hat{g}$ is permutation symmetric, so it will not couple spin states with different parities. The bases for the Hilbert space of the mapped p-wave Hamiltonian 2.20 are

$$\{\varphi(x_1, x_2)\chi(\sigma_1, \sigma_2) \mid \varphi \in \text{slater determinants}, \chi \in \text{spin states}\}, \qquad (2.21)$$

where $\{\varphi(x_1, x_2)\}$ is the set of all slater determinants, and $\{\chi(\sigma_1, \sigma_2)\}$ is the set of spin states without any symmetry constraint. Note that the bases of Eq. (2.21) correspond to SCAWs, for two particles. The properties of SCAWs will be discussed in Chapter 4.

For spinor Bose gases, the mapping follows the same derivation as spinor Fermi gases. The only difference is in Eq. (2.20), the anti-symmetric spin projection operator should change to symmetric spin projection operator $\hat{P}^s$.

Finally, we rewrite Eq. (2.20) as

$$H = \sum_{i=1,2} \left[-\frac{1}{2}\frac{\partial^2}{\partial x_i^2} + V(x_i) \right] - \frac{4 \cdot 2! \cdot \hat{P}^{s,a}}{\hat{g}} \frac{\overleftarrow{\partial}}{\partial x_{12}} \delta(x_{12})\theta(x_{12}) \frac{\overrightarrow{\partial}}{\partial x_{12}}. \qquad (2.22)$$

We have added an θ^1, which is valid since Eq. (2.22) acts on bases of Eq. (2.21), and the derivative $\partial\varphi_{x_1,x_2}/\partial x_{12}$ is continuous across $x_{12} = 0$. And we use this form for later convenience of deriving the generalized Bose-Fermi mapping for many particles in the Section 2.4.

2.4 Generalized Bose-Fermi Mapping for Many Particles

Now let's formulate the generalized Bose-Fermi mapping for many identical particle spinor quantum gases. The original contact s-wave interaction Hamiltonian 1.1 is $H_s = H_f + V_s$, where H_f is the free Hamiltonian, and

$$V_s = \hat{g} \sum_{i<j} \delta(x_{ij}), \qquad (2.23)$$

is the contact s-wave interaction, where $x_{ij} = x_i - x_j$. Our motivation is to use slater determinants only to describe the spatial degrees of freedom, i.e. we want to have a new Hamiltonian that uses the direct product of slater determinants and spin-chain wavefunctions

$$\{\varphi\chi|\varphi \in \text{slater determinants}, \chi \in \text{spin states}\}. \qquad (2.24)$$

as bases for the Hilbert space.

Note that the the bases of Eq. (2.24) have one-to-one mapping with the SCAWs of Eq. (2.6), since they are identical in θ^1 spatial sector, which has the complete information of the total wavefunction. However, in the SCAW, the spin state is only meaningful in one spatial sector. In other spatial sectors, the spin states are different. But we want to use only one well-defined spin state in a basis for the direct product state.

We put our focus on one spatial sector θ^1. As discuss before, the delta function contact interaction only introduces the boundary conditions of the eigenstates at spatial sector boundaries. At the region away from those boundaries, the eigenstates are governed by the free Hamiltonian H_f. So if we can have a new Hamiltonian with a pseudo interaction potential acting on the Hilbert space of Eq. (2.24), such that its eigenstates, at the boundary of one spatial sector θ^1, are one-to-one mapped to the eigenstates of the original Hamiltonian 1.1, then the new Hamiltonian is equivalent to the original Hamiltonian, since they have equivalent eigen systems.

Consider a one-dimensional (1D) spinor quantum gas with the N-body wave function

$$\Psi(x_1, x_2, ..., x_N, \sigma_1, \sigma_2, ..., \sigma_N) = \sum_P (\pm 1)^P P\left(\Psi^1(x_1, x_2, ..., x_N, \sigma_1, \sigma_2, ..., \sigma_N)\right),$$

$$(2.25)$$

where P represents permutation(Appendix A), and $\Psi^1 = \Psi\theta^1$, with θ^1 being the generalized Heaviside step function defined at Eq 2.2. Equation (2.25) is a manifestation of a special property of 1D system that the spatial domain of the wave function can be separated into $N!$ disconnected subdomains labeled by various spatial orders, and the wave function in one spatial sector (say, Ψ^1 as defined in spatial sector θ^1) has the complete information of the total wave function, as the values of the wave function in different spatial sectors are related by permutation operation. Consider the wavefunction in θ^1 spatial sector Ψ^1, we can always expand Ψ^1 into superposition of direct products of spatial function and spin function

$$\Psi^1 = \sum_\beta \Phi^1_\beta \chi_\beta \,, \tag{2.26}$$

and then for every spatial term Φ^1_β, since it is only nonzero in θ^1 spatial sector, we can always anti-symmetrize it and then expand into slater determinants:

$$\begin{aligned} \Phi^1_\beta &= \theta^1 \sum_P (-1)^P P \Phi^1_\beta \\ &= \theta^1 \sum_\alpha A_{\alpha,\beta} \varphi_\alpha \\ &= \sum_\alpha A_{\alpha,\beta} \varphi^1_\alpha. \end{aligned} \tag{2.27}$$

Combining Eq. (2.26) and Eq. (2.27), we can obtain the expansion:

$$\Psi^1(x_1, x_2, ..., x_N, \sigma_1, \sigma_2, ..., \sigma_N) = \sum_{\alpha,\beta} A_{\alpha\beta} \, \varphi^1_\alpha(x_1, x_2, ..., x_N) \chi_\beta(\sigma_1, \sigma_2, ..., \sigma_N) \,, \tag{2.28}$$

where $A_{\alpha\beta}$ are superposition coefficients, φ's are slater determinants and χ's are spin wave functions. $\varphi^1_\alpha = \varphi_\alpha \theta^1$ is the slater determinants in θ^1 spatial sector.

The expansion *Eq.* (2.28) means that we can expand any (anti-)symmetric many-body spinor wavefunction into a superposition of SCAWs with a set of complete

orthogonal slater determinants and a set of complete orthogonal spin states.

$$\Psi = \sum_{\alpha,\beta} A_{\alpha\beta} \sum_P (\pm)^P P(\varphi_\alpha^1 \chi_\beta) \,. \tag{2.29}$$

And note that any such SCAW can be one-to-one mapped to a direct product of slater determinant and spin wavefunction, i.e. a basis in Eq. (2.24). This means we can map any (anti-)symmetric spinor many-body wavefunction to a superposition of direct products of slater determinants and spin wavefunctions.

We have shown that the states of an identical spinor quantum gas system can be one-to-one mapped to (superposition)states of direct products of spatial and spin states, i.e. Spin-Charge Separated Representation (SCSR). Now we want to map the original Hamiltonian 1.1 to a new Hamiltonian acting on the SCSR.

Actually in Section 2.3, we have already obtained the new Hamiltonian for two spinor particles in Eq. (2.22), which acts on the SCSR for two particles of Eq. (2.21). Now we generalize this mapping to many-particles. Consider the boundaries of spatial sector θ^1, every boundary corresponds to two particles with neighboring indices at the same position, $x_i = x_{i+1}$. If we have a Hamiltonian acting on the SCSR that will produce the same boundary condition in θ^1 sector as the original (anti-)symmetric wavefunctions, then the Hamiltonian is the one we want to obtain. In fact, we can ensure every boundary labeled by $x_i = x_{i+1}$ has the correct boundary condition independently by applying the two particle mapping. However, we can not simply add Eq. (2.22) together for every $x_i = x_{i+1}$, because every two particle boundary individually can not ensure other particles in the θ^1 sector. Instead, we need to add a long range sector constraint for every term. Putting everything together, we can write down the full mapped potential term:

$$V_p = -\frac{4N!\hat{P}_i^{s,a}}{\hat{g}} \sum_{i=1}^{N-1} \overleftarrow{\partial}_{x_{i,i+1}} \delta(x_{i,i+1})\theta^1 \overrightarrow{\partial}_{x_{i,i+1}} \,, \tag{2.30}$$

	(anti-)symmetric representation	spin-charge separated representation
Hilbert Space	(anti-)symmetric $\Psi_{\{x\},\{\sigma\}}$	superpositions of $\varphi_{\{x\}}\chi_{\{\sigma\}}$
State	$\sum_{\alpha,\beta} A_{\alpha\beta} \sum_P (\pm)^P P(\varphi_\alpha \chi_\beta)$	$\sum_{\alpha,\beta} A_{\alpha\beta} \varphi_\alpha \chi_\beta$
Hamiltonian	$H_f + \hat{g} \sum_{i<j} \delta(x_{ij})$	$H_f - \frac{4N!\hat{P}_i^{s,a}}{\hat{g}} \sum_{i=1}^{N-1} \overleftarrow{\partial}_i \delta(x_{i,i+1}) \theta^1 \overrightarrow{\partial}_i$

Table 2.1 : Mapping from the original (anti-)symmetric representation to the SCSR. And ∂_i is $\partial_{x_{i,i+1}}$ for short.

which is a p-wave pseudopotential, where $x_{i,i+1} = x_i - x_{i+1}$ and $\partial_{x_{i,i+1}} = \frac{1}{2}\partial_i - \frac{1}{2}\partial_{i+1}$. And the full mapped Hamiltonian is $H_p = H_f + V_p$, where H_f same as before is the free Hamiltonian.

Note that the operators $\hat{P}_i^{s,a} = (1 \pm \mathcal{E}_{i,i+1})/2$ are spin projection operators that project out symmetric and antisymmetric spin states, respectively, where $\mathcal{E}_{ij}$ is the exchange operator that exchanges the ith and j^{th} spins. If the original spinor gas is bosonic (fermionic), one should take $\hat{P}_i^s$ ($\hat{P}_i^a$). This mapping is possible as the parity of the relative spatial wave function of two identical particles is directly linked to the exchange symmetry of their spin wave function.

We summarize the main result of this section in Table 2.4. The generalized Bose-Fermi mapping maps the original s-wave interacting spinor system into the SCSR. The charge part is composed of spinless fermion wavefunctions (slater determinants). The spin part is composed of spin wavefunctions.

Several points worth to mention, for the SCSR, at spatial sector boundaries, the wavefunction is always zero. However, for the original (anti-)symmetric wavefunctions, at spatial sector boundaries, the wavefunction could be non-zero. The controversy is resolved by the fact that the p-wave pseudopotential Eq. (2.30) can introduce discontinuous boundary conditions. At $x_i = x_{i+1} - 0^+$, the mapped wavefunction

in the SCSR has the same value as the original (anti-)symmetric wavefunction at $x_i = x_{i+1}$. A more intuitive example for the duality of relative wavefunctions is shown in Fig. 2.1. Around a sector boundary of SCSRs, the relative wavefunction is odd, but if the spatial wavefunction is discontinuous, it can correspond to an even relative wavefunction in the original representation with non-zero values on the boundaries. In a SCAW, for two particles, the parities of their relative spatial wavefunction and that of the spin wavefunction around the sector boundaries are linked as the total parity has be to odd (for fermions) or even (for bosons). In the SCSR, however, this link is not present as the relative spatial wavefunction is always odd around sector boundaries. The quantum statistics of the original system is taken care of by the spin parity project operator $\hat{P}_i^{s,a}$ in the mapped p-wave pseudopotential V_p.

2.5   Regularization of P-Wave Pseudopotential

As discussed at the end of Section 2.4, in the SCSR, the relative spatial wavefunction can be discontinuous, as a more illustrative figure in Fig. 2.1. So the differential operators in the p-wave pseudopotential 2.30 is ill defined at the sector boundary. In Section 2.2, we defined the derivative operator infinitely close to the boundary. However, in practice this will introduce some difficulties, since we usually need to use a truncated set of bases in the SCSR to do some practical calculation.[2] For example, we can use a truncated set of slater determinants as spatial bases, or discretize the continuous model to a lattice model. For those methods, there is a notion of shortest distance, which relates to the energy scale for the truncation of the bases. So there

---

[2]For perturbation calculations, since there is no wavefunction discontinuity, there is no such problem. And also for some method, such as Green's function method (Appendix D), the 'infinitely close to boundary' definition of the derivative operators can be directly incorporated.

is a question how to incorporate the 'infinitely close to boundary' definition of the derivative operators into the truncated bases methods. In this thesis, we call it regularization for the p-wave pseudopotential in mimic of the regularization in high energy physics.

Here we give one example of the regularization for discretization methods. Consider if we want to discretize the SCSR and Hamiltonian $H_p = H_f + V_p$, where V_p is in Eq. (2.30). The lattice model can be written as:

$$H^p = -t \sum_{\sigma,i} \left(a^\dagger_{i\sigma} a_{i+1\sigma} + a^\dagger_{i+1\sigma} a_{i\sigma} \right) + \sum_i \mu_i n_i + \sum_{i,\alpha,\beta,\gamma,\delta} \langle \alpha\beta | \hat{B} | \delta\gamma \rangle a^\dagger_{i\alpha} a_{i\delta} a^\dagger_{i+1\beta} a_{i+1\gamma} \,,$$

$$(2.31)$$

where a's are now hardcore fermion operators. $n_i = \sum_\sigma a^\dagger_{i\sigma} a_{i\sigma}$ is the local density operator. The parameters are related with the continuous model by

$$t = \frac{1}{2a^2}, \ \mu_i = V(ia) + \frac{1}{a^2}, \ \hat{B} = -\frac{2}{a^3} \frac{1}{\hat{g} + \frac{2}{a} - Ea} \,. \qquad (2.32)$$

Note that in the relation of $\hat{B}$ and $\hat{g}$, there is a counter term $2/a - Ea$, where a is the lattice constant. This counter term is obtained by comparing the eigenstates of relative motion of two particles for the discretized s-wave model Eq. (1.2) and p-wave model Eq (2.31) in every spin channel, for the derivation for the spinless Fermion case see [19].

Chapter 3

Effective Spin-Chain Models

In this section, we focus on the strongly interacting region of 1D spinor quantum gases. To be specific, we start from the spinor quantum gases Hamiltonian 1.1, and assume the interaction matrix can be factored out by a very large magnitude $\hat{g} = g\hat{\tilde{g}}$, where g is large scaler and $\hat{\tilde{g}}$ is a matrix that is finite and invertible. Without interaction, the ground state of 1D system can be easily obtained. For Bose gases, particles with the same spin are on the same lowest energy state. For Fermi gases, particles with the same spin form a Dirac Fermi sea. And particles with different spins can be regarded as distinguishable particles. The problem has essentially no more difficulty from single-particle problems. For weak interaction, some effective low energy theories can be constructed. For example mean-field theories (Gross-Pitaevskii equations [20]) approximates the many-body wavefunctions with direct product wavefunctions, hydrodynamic equations [21] writes the many-body Schrödinger equation into hydrodynamic differential equations, Bosonization [5] constructes low energy effective field theories around Fermi surface, which is also a 1D counterparts of Fermi liquid theories in higher dimensions, and so on. As interaction strength increases, many methods will become invalid, and the ground state wavefunctions become more strongly correlated and more complicated. Strongly correlated quantum many-body problems are well-known to be hard to solve.

On the other hand, if the interaction strength further increases towards infinity, under certain cases, things become easier. In Chapter 2, it has been show that we

can map Hamiltonian 1.1 to a p-wave interacting Hamiltonian with the interaction strength inversed. This allows us to construct perturbation theory using the mapped p-wave pseudopotential as perturbation term.

In the following sections in this chapter, we first discuss the perturbation theory results for a single charge branch. A emergent spin-chain model can be understood as super-exchange process of neighboring particles. One can intuitively understand the emergence of the super-exchange term as follows [22]. At $g = \infty$, particles are impenetrable in 1D and they cannot exchange positions with their neighbors. Away from $g = \infty$, there will be small but finite probability that two neighboring particles can exchange positions, which gives rise to the effective super-exchange interaction. The effective spin-chain Hamiltonian takes a form of a non-translational-invariant Sutherland model [23]. For spin-1/2 Fermions, the exchange operator can be written in terms of spin operators, and the Sutherland model reduces to the Heisenberg model. It immediately follows that the ground state of spin-1/2 Fermions is a Heisenberg anti-ferromagnetic (AFM) state in the strongly repulsive limit, and a ferromagnetic (FM) state in the strongly attractive limit (we exclude the tightly bound molecular states on the attractive side, i.e., we consider the upper branch of the system). We investigate the properties of such a system and demonstrate experimental signatures that allow us to distinguish the AFM and the FM states. using both the effective model and several unbiased methods, and show that the former is indeed valid in the strongly interacting regime.

The main advantages of the effective model are two fold. First, from a conceptual point of view, the effective model provides new insights to the quantum magnetic properties of strongly interacting particles in 1D. Second, from a practical point of view, the effective model is much easier to handle in comparison to unbiased meth-

ods. As a result, the effective model allows us to deal with more particle numbers and to investigate the dynamics to longer time scales. To this end, we benchmark our effective model against several unbiased methods and show that the former is indeed valid in the strongly interacting regime. These benchmark calculations also demonstrate that calculations based on the effective model are much more efficient and take much less time than those based on unbiased methods.

3.1   Single Branch Effective Spin-Chain Models

Consider the trapped spinor gas with N total atoms governed by Hamiltonian 1.1. Although our theory is valid for arbitrary V, we will focus on harmonic trapping potential $V(x) = x^2/2$, which not only is the most experimentally relevant, but also possesses special symmetry properties that we will exploit later. We have adopted a dimensionless unit system where $\hbar = m = \omega = 1$, with m and ω being the atomic mass and the trap frequency, respectively. The interaction Hamiltonian of the mapped system is given by V_p in Eq. (2.30).

For large g, we work on this mapped system, and treat V_p as a perturbation to the free Hamiltonian H_f. The unperturbed system is simply an ideal Fermi gas, whose ground state is formed by putting one atom in each of the lowest N single-body states, as schematically shown in Fig. 3.1(a), with energy $E^{(0)} = N^2/2$, and the ground state wave function is a Slater determinant which we denote as φ_0. In the context of the original spinor system, this corresponds to the Tonks-Girardeau (TG) limit with $g = \infty$, for which the ground state possess spin degeneracy as its energy is completely independent of the spin configuration. For large but finite g (Here we focus on the case with repulsive interaction, i.e., $g > 0$, although the spin-chain model is also valid for the upper branch in the strongly attractive regime.), to first order in
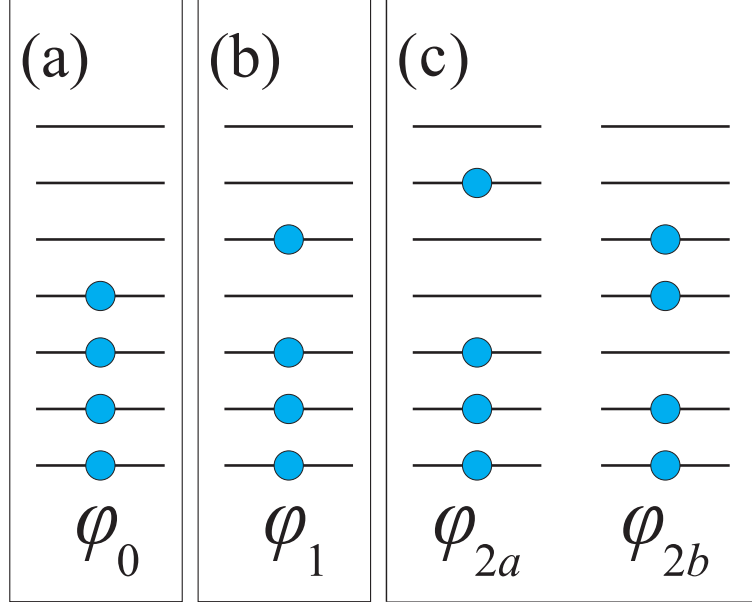
Figure 3.1 : (color online) Schematic representation of the ground state (a), the first excited state (b), and the second excited states (c) of an ideal spinless Fermi gas.

V_p (i.e., in $1/g$), we can readily derive an effective Hamiltonian:

$$H_{\text{sc}}^{(0)} = E^{(0)} + \langle \varphi_0 | V_p | \varphi \rangle = E^{(0)} - \frac{1}{g} \sum_{i=1}^{N-1} C_i^{(0)} \left(1 \pm \mathcal{E}_{i,i+1} \right), \qquad (3.1)$$

with the coefficients $C_i^{(0)}$ given by

$$C_i^{(0)} = 2N! \int dx_1 ... dx_N \, |\partial_i \varphi_0|^2 \, \delta(x_i - x_{i+1}) \theta^1 \,. \qquad (3.2)$$

This is the inhomogeneous spin-chain Hamiltonian for a 1D strongly interacting quantum gas, where E^0 is the first order ground state energy. In Eq. (3.1) plus sign means the original gas is Bosonic and minus sign means it is Fermionic.

3.2   Applications of Single Branch Spin-Chain Models

The effective spin-chain model discussed in Section 3.1 holds for spinor quantum gases with arbitrary spins, arbitrary (permutation symmetric) interaction matrix $\hat{g}$,

and Bosonic or Fermionic statistics. In this section, we discuss a special case of spin-1/2 Fermi gases. The exchange operator can be written in terms of the spin operators:

$$\mathcal{E}_{i,j} = (1 + \vec{\sigma}_i \cdot \vec{\sigma}_j)/2 \,, \tag{3.3}$$

where $\vec{\sigma}_i$ are the Pauli spin matrices for the i'th atom. With Eq. (3.3) we can rewrite the effective spin-chain Hamiltonian 3.1 for Fermions as

$$H_{\text{eff}} = -\frac{1}{g} \sum_{i=1}^{N-1} C_i (1 - \vec{\sigma}_i \cdot \vec{\sigma}_{i+1})/2 \,, \tag{3.4}$$

which takes the form of the non-translational-invariant Heisenberg model with $C_i/(2g)$ plays the role of the super exchange coefficient between the i'th and the $(i+1)$'th spin. The effective spin-spin interaction is ferromagnetic (FM) for $g < 0$, and anti-ferromagnetic (AFM) for $g > 0$. Note that as the number of atoms in each spin species are individually conserved, the spin configuration for the FM state here can be written as $(S^-)^{N_\downarrow} |\uparrow\uparrow \cdots \uparrow\rangle$ and is fully symmetric, with $S^- = \sum_i \sigma_i^-/2$ being the total spin lowering operator.

3.2.1 Energy Spectrum of 3 Strongly Interacting Spin-1/2 Fermions.

To benchmark the spin-chain model, we show in Fig. 3.2(a) the low energy spectrum of a three-body system. Similar benchmarks were also performed in Refs. [24, 25]. In this work, we focus on spin-1/2 Fermions, and label the two spin species as $\uparrow$ and $\downarrow$. The external potential is chosen to be a harmonic potential with frequency ω. In our calculation, we take $\hbar = m = \omega = 1$, and the observables are normalized to dimensionless values: $x \sim x/\sqrt{\hbar/(m\omega)}$, $p \sim p/\sqrt{\hbar m\omega}$, and $E \sim E/\hbar\omega$. The main figure of Fig. 3.2(a) is obtained by the unbiased Green's function method based on the original many-body Hamiltonian 1.1 [26]. For more details about using Green's
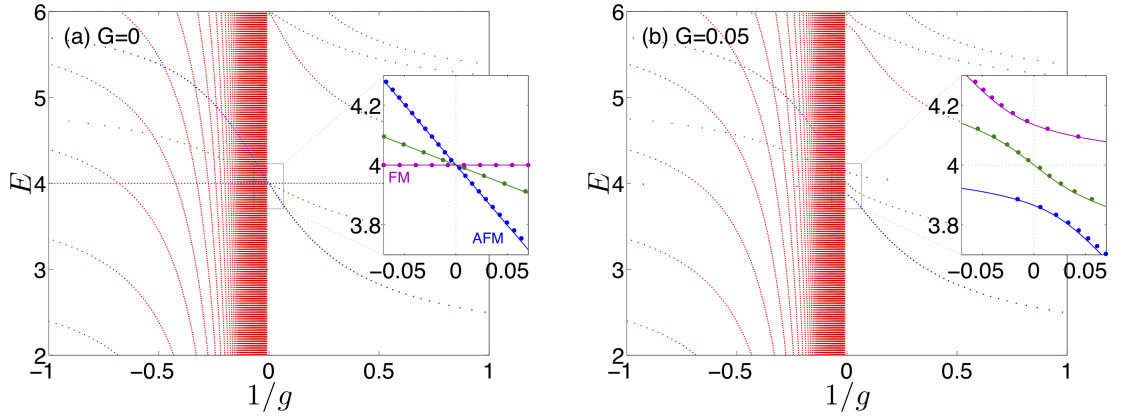
Figure 3.2 : (Color online) Energy spectrum of the relative motion as a function of $1/g$ for three Fermions with $(N_\uparrow, N_\downarrow) = (1, 2)$, without (a) and with (b) the spin-dependent magnetic gradient. For (b), we have $G = 0.05$. The main figures are obtained using the Green's function method (Appendix D). The red dotted lines in negative g area represent the tightly bound molecular states. The inset figures show the comparison between the spectrum obtained from the Green's function method (dots) and that from the effective spin-chain model (solid lines) near $1/g = 0$. In all the figures presented in this paper, we have adopted the trap units with $\hbar = m = \omega = 1$. Consequently, the energy E is in units of $\hbar\omega$, and the interaction strength g is in units of $\sqrt{\hbar^3\omega/m}$.

function method for solving few-body spinor quantum gas systems, see Appendix D. In the inset, we compare this exact spectrum (dots) with the spectrum obtained from the spin-chain Hamiltonian H_{eff} (solid lines). As one can see, in the strong interaction regime with $1/|g| \ll 1$, the spin-chain model faithfully reproduces the exact spectrum of the upper branch when the tightly bound molecular states on the attractive ($g < 0$) side are ignored. We can gain some insights into the spectrum of H_{eff} by noting that the eigenvalues of the exchange operator $\mathcal{E}_{i,i+1}$ are ± 1. Therefore, for $g > 0$, the spectrum of H_{eff} has a lower bound of $-(2/g)\sum_{i=1}^{N-1} C_i$ (corresponding to a fully anti-symmetric spin configuration with $\mathcal{E}_{i,i+1} = -1$ for any i), and an upper bound of 0 (corresponding to a fully symmetric spin configuration with $\mathcal{E}_{i,i+1} = 1$ for any i).

We remark that the fully anti-symmetric spin configuration can only be realized for $2s + 1 \geq N$. For not too small N, this requires a Fermionic species with large spin s. Recent cold atom experiments have witnessed realization of high spin Fermi gases in alkali-earth atoms [27–30]. For $g < 0$, the spectrum is inverted and bound between 0 and $|2/g| \sum_{i=1}^{N-1} C_i$. From Eq. (3.4), we know the effective spin-spin interaction is ferromagnetic (FM) for $g < 0$, and anti-ferromagnetic (AFM) for $g > 0$. We therefore label the corresponding ground state FM for $g < 0$ and AFM for $g > 0$, as shown in the inset of Fig. 3.2(a), which is consistent with the Bethe ansatz result for the homogeneous case [31, 32].

3.2.2 Density Profiles in Real and Momentum Spaces

In cold atom experiments, density profiles in real and momentum spaces can be directly measured, which serve as an effective tool to study the state of the quantum gases system. Let us now examine in detail the density profiles in both real and momentum spaces for the ground state of H_{eff}. To find the density profiles in both real and momentum spaces, let us first introduce the one-body density matrix element for spinor quantum gases system defined as

$$\rho_{\sigma'\sigma}(x', x) = \sum_{\sigma_2...\sigma_N} \int dx_2, ..., dx_N \, \Psi^*(x', x_2, ..., \sigma', \sigma_2, ...) \Psi(x, x_2, ..., \sigma, \sigma_2, ...), \quad (3.5)$$

from which the real-space and momentum space density profiles can be calculated as

$$\begin{aligned}
\rho_\sigma(x) &= N\rho_{\sigma,\sigma}(x, x), \\
\rho_\sigma(p) &= \frac{N}{2\pi} \int dx \int dx' \, e^{-ip(x-x')} \rho_{\sigma,\sigma}(x', x).
\end{aligned}$$

In Appendix E, we provide the details of calculating the one-body density matrix element given a SCAW of Eq. (2.6).

In Fig. 3.3, we present the density profiles for $N = 2$ spin-1/2 Fermions with $(N_\uparrow, N_\downarrow) = (1, 1)$. For this two-body problem, exact analytic solutions for arbitrary interacton strength g can be found [33]. Results displayed in Fig. 3.3 are obtained from the exact method. As a result, we are not limited to large $|g|$. Note that the FM state corresponds to a fully symmetric spin configuration χ, and its density profiles, which are g-independent, are identical to a system of N spinless Fermions. More specifically, $\rho_\sigma(x) = (N_\sigma/N) \sum_{i=0}^{N-1} |\phi_i(x)|^2$, where $\phi_i(x)$ is the ith eigen-wave function of the single particle Hamiltonian; and $\rho_\sigma(p)$ decays as $\exp(-p^2)$ in the large p limit.

The AFM state, on the other hand, possesses a fully anti-symmetric spin configuration and its density profiles are sensitive to the value of g. As $1/g \to 0$, the real-space density profile of the AFM state approaches that of the FM state, whereas the momentum space density profile remains distinct for these two states. Hence, in the strongly interaction limit, the density profiles for the AFM and the FM states are indistinguishable in real space, but distinguishable in momentum space. This statement remains true for $N > 2$.

As a further example, we consider a system of $(N_\uparrow, N_\downarrow) = (4, 4)$ spin-1/2 Fermions in the strongly interacting limit. In Fig. 3.4 we show the momentum space density profiles. The black dashed line corresponds to the momentum distribution of the FM state (which is the same as the momentum distribution of N spinless Fermions), and the red solid line to that of the AFM state. The AFM state has a nonzero Tan contact K, and in the large momentum limit, we have $\rho(p) = K/(2\pi p^4)$ [34]. This is confirmed by our numerics as shown in the inset of Fig. 3.4. For comparison, we also show the momentum distribution of a fully anti-symmetric spin state, which coincides with the momentum distribution of N spinless Bosons in the Tonks-Girardeau limit.
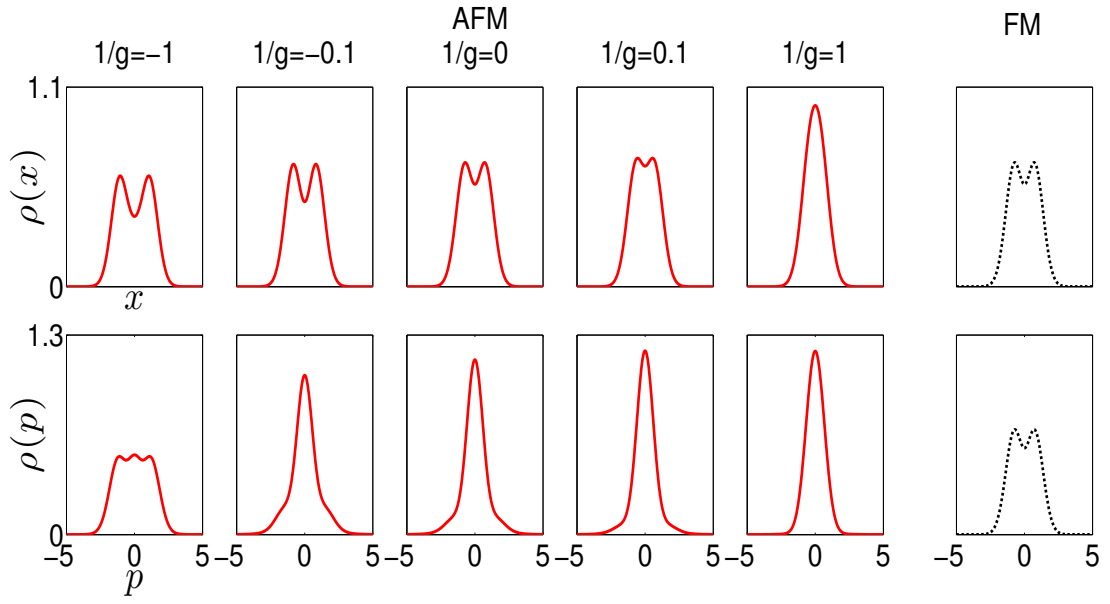
Figure 3.3 : (Color online) Real space density profiles (upper panel) and momentum space density profiles (lower panel) for $(N_\uparrow, N_\downarrow) = (1, 1)$ versus $1/g$ for AFM (red solid lines) and FM (black dotted lines) states. In our trap units, position x is units of $\sqrt{\hbar/(m\omega)}$, the real space density $\rho(x)$ is in units of $\sqrt{m\omega/\hbar}$, the momentum p is in units of $\sqrt{\hbar m\omega}$, and the momentum space density $\rho(p)$ is in units of $1/\sqrt{\hbar m\omega}$.

As we mentioned earlier, the fully anti-symmetric spin state is only possible when $2s + 1 \geq N$ [35]. We emphasize again that these different states have identical real space density profile, but can be distinguished from their distinctive momentum distribution.

3.2.3 Response to Spin-Dependent Magnetic Gradient

The form of the spin-chain effective Hamiltonian H_{eff} makes it clear that a quantum phase transition is induced as $1/g$ is tuned across zero, which can be achieved using the technique of confinement induced resonance [36, 37]. In practice, however, more effort is required to observe this phase transition. The AFM ground state for $g > 0$ can be straightforwardly prepared. Such is not the case for the FM state on the attractive side with $g < 0$. This is due to the fact that, for $g < 0$, there exist many bound molecular states with lower energies than the FM state, as can be seen from Fig. 3.2(a). If one simply prepare the system on the attractive side, these molecular states, not the FM state, will be realized. Hence to create the FM state, one needs to start from the AFM state on the repulsive side and adiabatically tune the interaction strength to the attractive side. However, the spin states are protected by symmetry: If we start from the AFM state and tune $1/g$ across zero, the system will remain as an AFM state and realize a Fermionic super-Tonks-Girardeau state [38, 39], as there is no coupling between the AFM and the FM states. To overcome this problem, we need to add a spin symmetry breaking term. One possibility is to add a spin-dependent gradient term. We will consider in detail how to realize the FM state in the next section. Here we first investigate how the AFM and the FM states respond to such a gradient term.

To this end, we introduce a weak spin-dependent magnetic gradient which adds
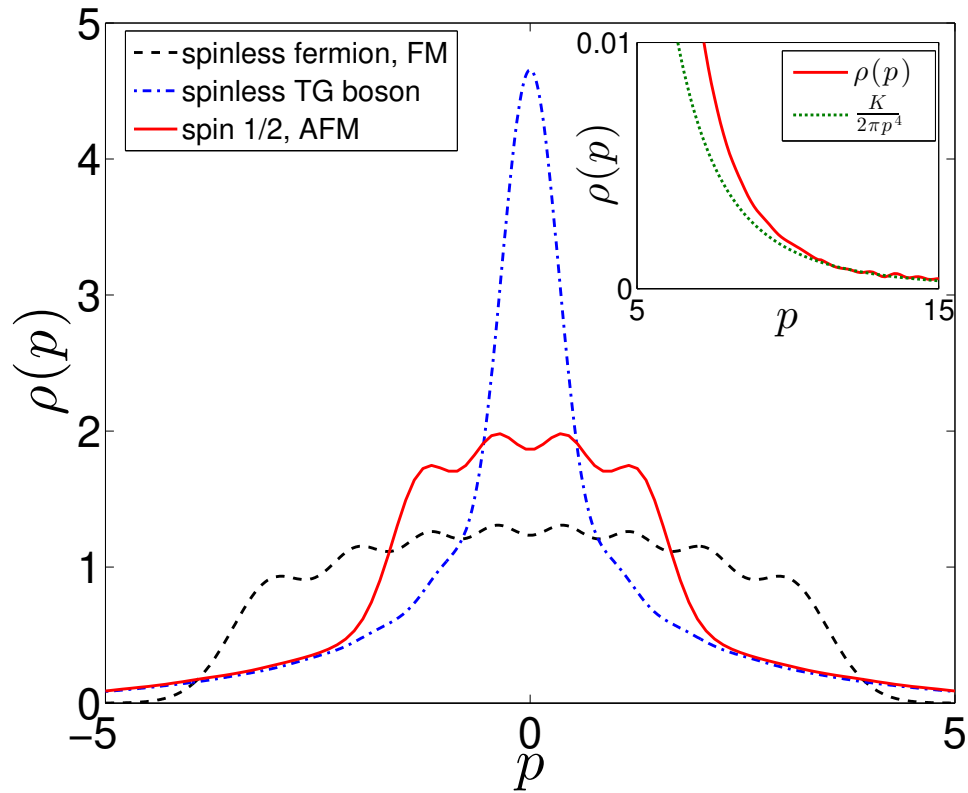
Figure 3.4 : (Color online) Momentum distribution for $(N_\uparrow, N_\downarrow) = (4, 4)$. The black dashed curve is for the fully spin symmetric FM state, which has the same momentum distribution as N spinless Fermions. The red solid curve is for the AFM state. The blue dash-dotted curve is for the fully spin anti-symmetric state, which has the same momentum distribution as N spinless Tonks-Girardeau Bosons. The inset shows the momentum distribution for the AFM state in the large momentum limit, in comparison to the theoretical prediction $K/(2\pi p^4)$ (green dotted curve), where K is Tan contact.

a term $-G \sum_i x_i \sigma_i^z$ to the Hamiltonian (1.1), where G, which we will take to be non-negative, characterizes the magnitude of the magnetic gradient. The effective spin-chain Hamiltonian will be modified correspondingly as

$$H_{\text{eff}} = -\frac{1}{g} \sum_{i=1}^{N-1} C_i(1 - \vec{\sigma}_i \cdot \vec{\sigma}_{i+1})/2 - G \sum_{i=1}^{N} D_i \sigma_i^z \,, \tag{3.6}$$

where $D_i = N! \int x_i |\varphi_A|^2 \theta^1 \prod_{j=1}^{N} dx_j$ represents the position of the ith atom. For more details about how to calculate D_i coefficients and a general discussion about magnetic gradients, see Appendix F. In Fig. 3.2(b), we plot the energy spectrum for a three particle system in the presence of weak spin gradient, obtained from both the Green's function method and the effective model. Again we see excellent agreement in the strongly interacting regime. Comparing the insets of Fig. 3.2(a) and (b), one can easily see that the gradient term lifts the spin degeneracy at $1/g = 0$, and the ground state is now separated from excited states by a finite gap, which facilitates the adiabatic preparation of the FM state to be discussed later.

The spin gradient tends to separate the two spin species [40]. To quantify this effect, we define

$$\Delta = \frac{1}{N} \sum_{i=1}^{N} \langle x_i \sigma_i^z \rangle \,, \tag{3.7}$$

which measures the center-of-mass separation between the two spin species. Here the expectation value is taken with respect to the ground state of the effective Hamiltonian (3.6). In the absence of the gradient ($G = 0$), $\Delta = 0$ for both the FM and the AFM states. Under the effective spin-chain model, Δ is a function of Gg only.

As a first example, we again consider a two particle system with $(N_\uparrow, N_\downarrow) = (1,1)$. For this simple system, Hamiltonian (3.6) can be easily diagonalized, and Δ has an

analytic expression:

$$\Delta = \sqrt{\frac{2}{\pi}} \frac{\left[2G|g| + \sqrt{1 + 4(G|g|)^2}\right]^2 - 1}{\left[2G|g| + \sqrt{1 + 4(G|g|)^2}\right]^2 + 1}.$$

Note that since Δ only depends on $|g|$, we conclude that the FM and the AFM state respond identically to the gradient in the two-body case. We plot Δ as a function of $G|g|$ in Fig. 3.5(a). In the figure, we also plot the result obtained from an exact solution using the Green's function method with $g = \pm 20$, which are in good agreement with the effective model. The details of this solution can be found in Appendix D.

By contrast, for $N > 2$, the ground states for $g > 0$ and $g < 0$ will response differently to the gradient. In Fig. 3.5(b) and (c), we plot Δ as a function of $G|g|$ for the cases $(N_\uparrow, N_\downarrow) = (1, 2)$ and (2,2), respectively. The dashed and solid curves correspond to the ground state of negative and positive g, respectively. In general, the ground state on the attractive side will have a stronger response. To benchmark the effective model, we studied this problem using the Time-Evolving Block Decimation (TEBD) method [41–44]. In TEBD, a many-body wave function is represented by a Matrix-Product state (MPS), which approximates a many-body wave function by making a truncation of the entanglement spectrum. For 1D gaped system, whose entanglement is short-ranged, the truncation error is well controlled, and the TEBD method therefore represents an unbiased method and has been implemented widely to study 1D systems. The symbols in Fig. 3.5(c) are the TEBD results for positive g. One can see that for large g, the results obtained from TEBD and the effective model agree with each other very well.

To further quantify the response to the gradient and show the difference between the AFM and the FM states, we define the magnetic gradient susceptibility as

$1/|g|(d\Delta/dG)_{G=0}$, and the following relation can be readily derived:

$$\frac{1}{|g|}\frac{d\Delta}{dG}\bigg|_{G=0} = \frac{2}{|g|N^2}\sum_{n\neq 0}\frac{\left|\langle 0|\sum_{i=1}^{N}x_i\sigma_i^z|n\rangle\right|^2}{E_n - E_0}, \tag{3.8}$$

where $|n\rangle$ represents the nth eigenstate of the spin-chain Hamiltonian with $G = 0$, and E_n is the corresponding eigen-energy. $|0\rangle$ represents the ground state, which is the AFM (FM) state for positive (negative) g. In Fig. 3.5(d) we plot this susceptibility as a function of the total particle number N for the case with $N_\uparrow = N_\downarrow = N/2$. One can see that, as long as $N > 2$, the FM state possesses a larger susceptibility, i.e., is more prone to spin segregation under the gradient, than the AFM state. Furthermore, the susceptibility for the FM state grows rather rapidly as N increases, whereas that for the AFM state is not very sensitive to N.

3.2.4 Adiabatic Preparation of Ferromagnetic State

In the previous section, we suggested a method of applying weak spin-dependent magnetic gradient to approach the FM state in experiment. Here we will discuss the method in detail. The experimental protocol is in the following: (1) The system is initially prepared in the ground state with strong repulsion ($g > 0$) and a relatively large magnetic gradient. In the example presented in Fig. 3.6, we choose the initial values $1/g = 0.01$ and $G = 0.1$. (2) From $t = 0$ to T_1, G is fixed at the initial value while the interaction strength is tuned to the attractive side as $1/g(t) = 0.01\cos(\pi t/T_1)$, which can be achieved with confinement-induced-resonance method. (3) Finally, from $t = T_1$ to $T_1 + T_2$, g is fixed at its value at T_1, while the gradient strength G is slowly turned off. We vary G such that the instantaneous spin separation Δ follows the form

$$\Delta(t) = \Delta[G(t)] = \Delta(T_1)\cos^2\left[\frac{\pi(t - T_1)}{2T_2}\right]. \tag{3.9}$$
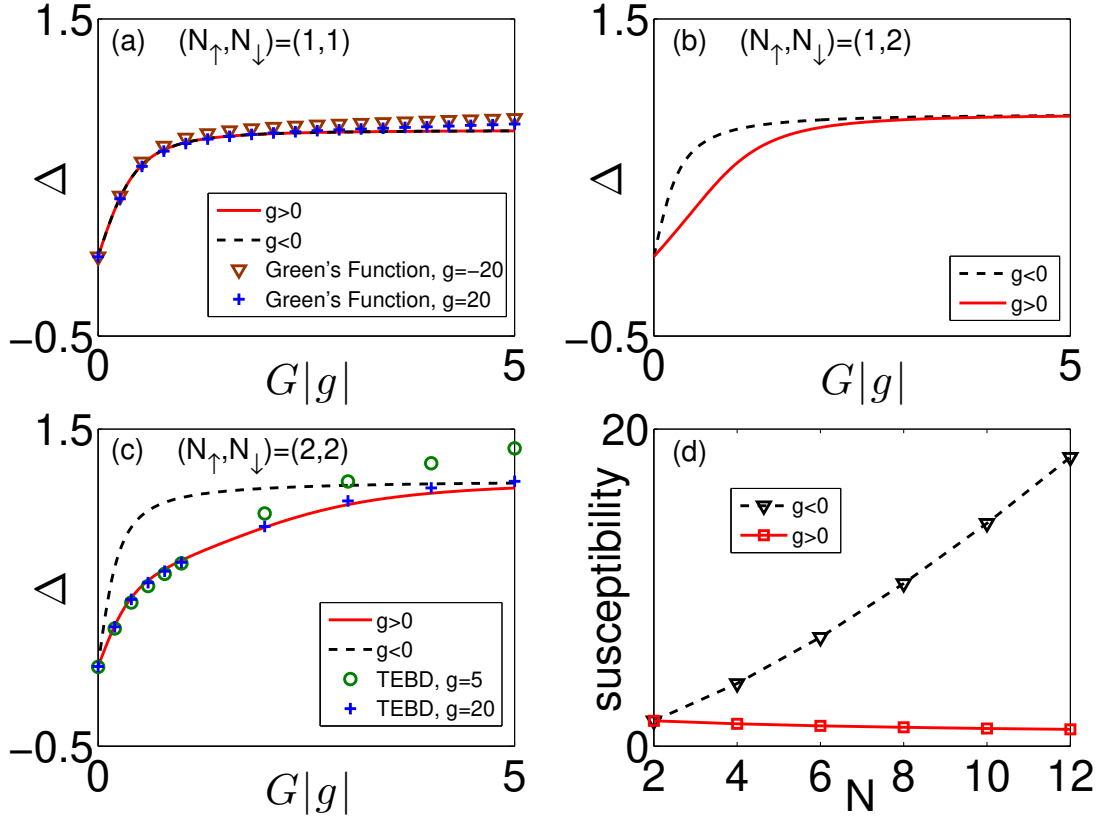
Figure 3.5 : (Color online) Separation between the two spin species as a function of $G|g|$ for (a) $(N_\uparrow, N_\downarrow) = (1,1)$, (b) $(N_\uparrow, N_\downarrow) = (1,2)$, (c) $(N_\uparrow, N_\downarrow) = (2,2)$. The black dashed curves are for the ground state with negative g, and the red solid curves are for the ground state with positive g. The symbols in (a) are obtained from the analytic solution detailed in Appendix D. The symbols in (c) are TEBD results. (d) The susceptibility $\left. \frac{d\Delta}{|g|dG} \right|_{G=0}$ as functions of N for $N_\uparrow = N_\downarrow = N/2$. In our trap units, Δ is in units of $\sqrt{\hbar/(m\omega)}$, and Gg in units of $\hbar^2\omega^2$.

The experimentally controlled parameters are plotted in Fig. 3.6(a) for $T_1 = 20\,T_{\text{ho}}$ and $T_2 = 280\,T_{\text{ho}}$, where $T_{\text{ho}} = 2\pi/\omega$ is the harmonic trap period.

In Fig. 3.6(b) we display the evolution of the spin separation parameter Δ in an example system with $(N_\uparrow, N_\downarrow) = (2, 2)$, $T_1 = 20\,T_{\text{ho}}$, and $T_1 + T_2 = 100\,T_{ho}$, $200\,T_{ho}$, and $300\,T_{ho}$. The dashed curves represent the targeted instantaneous value as shown in Eq. (3.9); while the solid curves are obtained by solving the time-dependent Schrödinger equation under the effective Hamiltonian H_{eff}. As expected, the larger the T_2, the better agreement between the solid and dashed curves. In the inset, we also show the fidelity, which is the overlap between the calculated wave function from evolving the Schrödinger equation and the instantaneous ground state wave function given the values of g and G at the moment, for the case $T_1 + T_2 = 300\,T_{\text{ho}}$. One can see that an FM state can be realized with very high fidelity. For a shorter total evolution time with $T_1 + T_2 = 100\,T_{\text{ho}}$, we still obtain a fidelity higher than 94%.

Although we have proposed to use a spin-dependent magnetic gradient to break the spin symmetry and facilitate the adiabatic preparation of the FM state, in reality any spin symmetry breaking term can do the job. Experimentally, this means one needs to introduce some perturbation to the system to which the two atomic spin states will respond differently. A possibility is to apply an off-resonant light with proper polarization such that it induces different light shift to different atomic spin states. This idea has been recently implemented to create spin-dependent optical lattices for cold atoms [45, 46].

Finally, we comment on the stability of the FM state. Due to presence of the tightly bound molecular states on the attractive side, the FM can only be metastable. In 2009, Haller *et al.* realized such a metastable state in a system of spinless Bosons [12], and the resulting state is the so called super Tonks-Girardeau (sTG) gas. In that

experiment, a typical lifetime of about 100 ms is found. We expect the lifetime of the FM state in a spin-1/2 Fermi gas should be longer than the bosonic sTG gas. This is because the low-lying molecular states for Fermions must be spin singlet. Therefore the spin symmetric FM state will be protected by spin symmetry against decaying into the molecular states.

3.2.5 Quench Dynamics without Spatial Degrees of Freedom

In Fig. 3.7 we present another example. Here we consider a quench dynamics in which the system is initially prepared in the ground state with $1/g = 0.01$ and $G = 0.05$. At $t = 0$, the spin gradient is suddenly turned off and the evolution of the center-of-mass separation between the two spin species Δ is calculated by solving the time-dependent Schrödinger equation. We solve the Schrödinger equaton using both the effective spin-chain model governed by H_{eff}, and the TEBD method governed by the original many-body Hamiltonian. As can be seen from Fig. 3.7, the effective model nicely reproduces the TEBD result. We therefore demonstrated that the spin-chain model can be applied to study the dynamics of the system. This example also serves to showcase the advantages of the effective model in the dynamical situation: due to its smaller Hilbert space, it can capture much longer time scale behavior of the system. Furthermore, it takes a few days to obtain the TEBD result as displayed in Fig. 3.7, in comparison to a few tens of seconds for the spin-chain result.

3.3 Multi-Branch Spin-Chain Models

In single-branch spin-chain models, the charge (spatial) degrees of freedom is fixed to a certain free fermion eigenstate (slater determinant) of the free Hamiltonian H_f in Eq. (1.1), the spin degrees of freedom is governed by an effective spin-chain model.
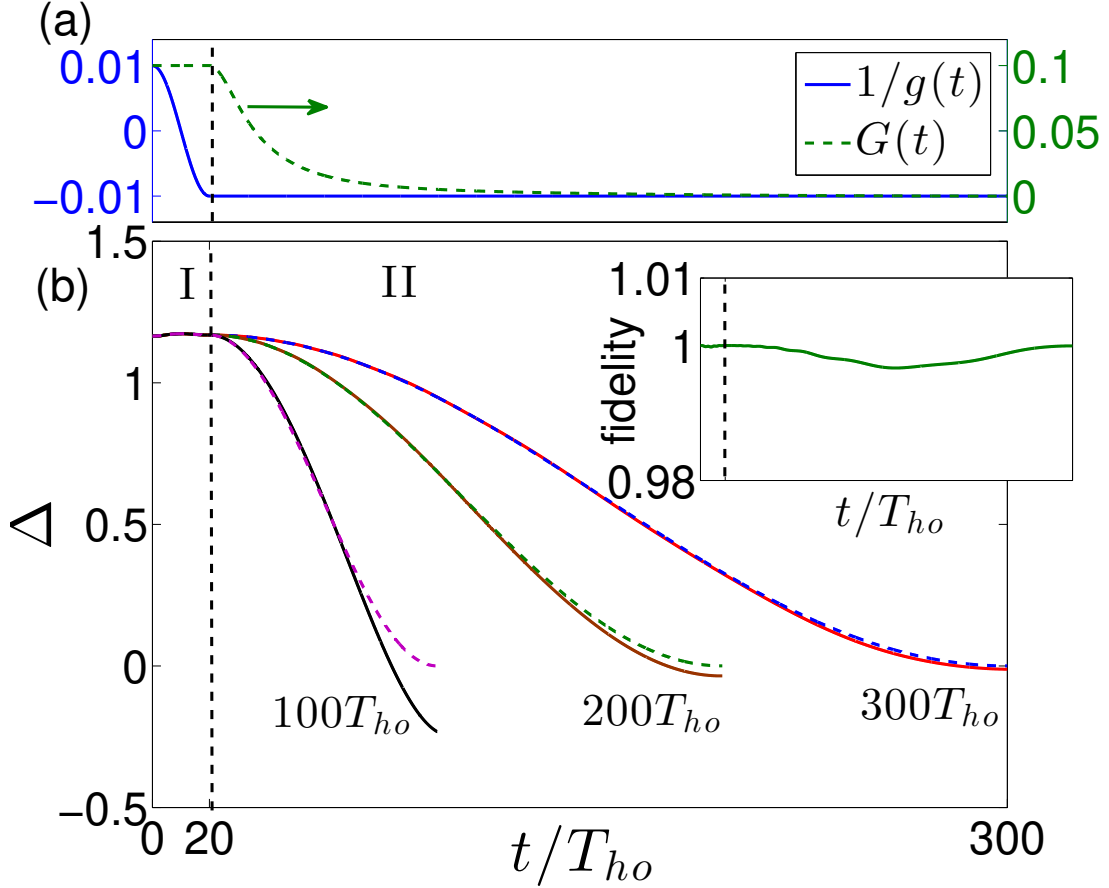
Figure 3.6 : (Color online) Adiabatic preparation of the FM state. At $t = 0$, the system is prepared in the ground state with $1/g = 0.01$ and $G = 0.1$. (a) The value of experimentally controlled parameters $1/g(t)$ and $G(t)$ for a total adiabatic evolution time $300T_{\text{ho}}$. (b) The solid lines represent $\Delta(t)$ obtained by solving the time-dependent Schrödinger equation under the effective Hamiltonian H_{eff}. The dashed lines represent Eq. (3.9), which is the $\Delta(t)$ of the instantaneous ground state for the given values of $g(t)$ and $G(t)$. Three different total adiabatic evolution time is calculated, $100\,T_{\text{ho}}$,$200\,T_{\text{ho}}$, and $300\,T_{\text{ho}}$. The inset shows the fidelity of the adiabatically prepared state for the total evolution time $300\,T_{\text{ho}}$.
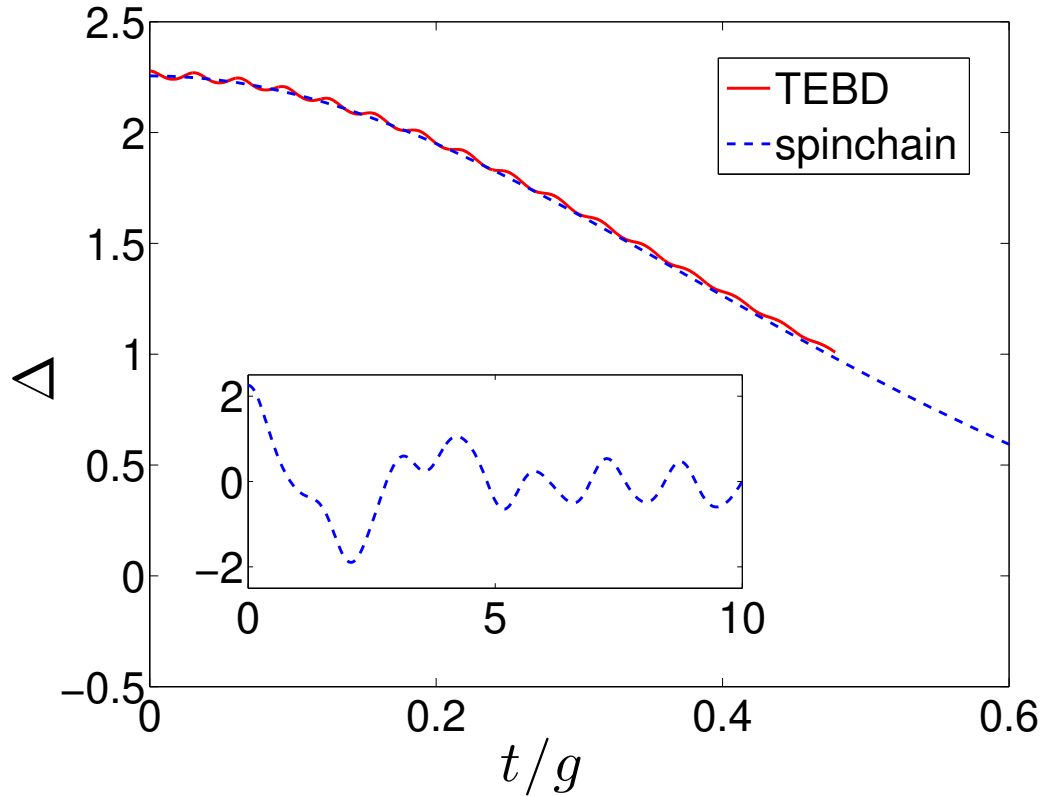
Figure 3.7 : (Color online) Quench dynamics without spatial degree of freedom for $(N_\uparrow, N_\downarrow) = (2, 2)$. The initial state is prepared as the ground state with $1/g = 0.01$ and $G = 0.05$. At $t = 0$, G is set to zero, and the system starts to evolve in time. The red solid line is $\Delta(t)$ calculated using the TEBD method, and the blue dashed line is calculated using the effective spin-chain model. The inset figure shows the evolution for much longer time under the spin-chain model. In our trap units, t/g is in units of $\sqrt{m/(\hbar^3 \omega^3)}$.

The perturbation theory is constructed around the infinite interaction point. So when the interaction strength is away from the infinite interaction point, the system may be not able to be described by an effective spin-chain model, the charge degrees of freedom and spin degrees of freedom may be coupled with each other. In this section, we still discuss under perturbation theory, but take into account the charge degrees of freedom. We develop a multi-branch spin-chain model through the generalized Bose-Fermi mapping for spinor quantum gases. Then we analyze the role of charge degrees of freedom around infinite interaction by calculating the system's response to a perturbation that will couple spin and charge degrees of freedom.

With the generalized Bose-Fermi mapping for spinor quantum gases, we can map both spinor Bose and Fermi gases to spin-charge separated representation governed by the Hamiltonian $H_p = H_f + V_p$, where V_p is the p-wave interaction Eq. (2.30). This mapping transform the interaction strength to its inverse, so is very useful for strong interactions. In this section, we focus on strong interaction again, but comparing with Section 3.1, we consider a more complete picture such that we also introduce the charge degrees of freedom in the perturbation theory.

Previous works have established that the spin-chain model represented by Hamiltonian 3.1 describes rather accurately many of the ground state properties of the original strongly interacting spinor gas to order $1/g$. In order to provide a more complete description of the system, and in particular of the *dynamical* properties of the system, we now extend the calculation to include excited eigenstates of the unperturbed Hamiltonian H_f to construct a multi-branch spin-chain model.

The excited eigenstates of the non-interacting system governed by H_f can be easily constructed. The first excited state, with wave function denoted as φ_1 and represented in Fig. 3.1(b), is obtained by promoting the atom at the Fermi level

in the ground state φ_0 to the next single-particle state. For harmonic traps with equal spacing single-particle energy levels, the second excited state, as represented in Fig. 3.1(c), is two-fold degenerate with wave functions denoted as φ_{2a} and φ_{2b}, respectively. We can now carry out a similar first-order perturbation calculation and construct the corresponding spin-chain Hamiltonian for each excited manifold. For example, for the first excited state, we obtain the following spin-chain Hamiltonian:

$$H_{\text{sc}}^{(1)} = E^{(1)} - \frac{1}{g} \sum_{i=1}^{N-1} C_i^{(1)} \left(1 \pm \mathcal{E}_{i,i+1}\right), \tag{3.10}$$

where $E^{(i)} = E^{(0)} + i$ is the energy of the ith excited state of the ideal Fermi gas, and the coefficients $C_i^{(1)}$ are given by Eq. (3.2) with φ_0 replaced by φ_1. Similarly, the spin-chain Hamiltonian for the second excited manifold can be written as

$$H_{\text{sc}}^{(2)} = E^{(2)} - \frac{1}{g} \sum_{i=1}^{N-1} \mathbf{C}_i^{(2)} \left(1 \pm \mathcal{E}_{i,i+1}\right), \tag{3.11}$$

where, due to the two-fold degeneracy of this manifold, $\mathbf{C}_i^{(2)}$ is a 2×2 matrix whose elements are given by

$$\left(\mathbf{C}_i^{(2)}\right)_{\alpha\beta} = 2N! \int dx_1...dx_N \, \partial_i \varphi_\alpha \delta(x_i - x_{i+1}) \theta^1 \partial_i \varphi_\beta \,, \tag{3.12}$$

with $\alpha, \beta = 2a, 2b$. Strictly speaking, Hamiltonian 3.11 is no longer a pure spin Hamiltonian, as we now have two spatial wave functions $\varphi_{2a,2b}$, which leads to a spin-orbit coupling between the spatial and the spin sectors.

In principle, one can construct the effective Hamiltonian for any other excited manifold in a similar manner as long as we plug in the corresponding Slater determinant(s) to evaluate the coefficients C_i. In the following sections, we will show that the special symmetry properties of harmonic trapping potential allows us to write down the spin-chain model for low-lying excited manifolds from that of the ground

state spin-chain Hamiltonian (3.1) without any extra calculations. This also provides significant insights into the low-lying collective excitation modes for harmonically trapped spinor quantum gases.

3.4 Applications of Multi-Branch Spin-Chain Models

In this section, we show several applications of the multi-branch spin-chain model for spin-1/2 fermions in a harmonic trap. Those include how the multi-branch spin-chain model can help analyzing the symmetry properties of the harmonic trap, breathing modes, and quench dynamics with spatial degree of freedom.

3.4.1 SO(2, 1) Symmetry for fermions in Harmonic Trap

Consider first an ideal gas of harmonically trapped N spinless fermions under Hamiltonian H_f. The center-of-mass (COM) motion can be separated from the relative internal motion. The COM dipole mode can be excited by the operator $Q^\dagger = (K-iP)/\sqrt{2}$, where K and P correspond to the COM position and momentum operators, respectively. (For the detailed definition and properties of these operators, see Appendix B.) On the other hand, one can also construct an operator $B^\dagger$ which excites a breathing mode which is an excitation in the internal motion. We can further define the internal Hamiltonian as $H_f^i = H_f - \{Q, Q^\dagger\}/(2N)$, which together with B and $B^\dagger$ form a closed SO(2,1) algebra [47–50]. The internal states can then be classified into irreducible representations of this SO(2,1) algebra. The first excited state φ_1, represented by Fig. 3.1(b), represents the lowest COM dipole excitation and is generated from the ground state φ_0 (Fig. 3.1(a)) by applying $Q^\dagger$ once, i.e., $\varphi_1 = Q^\dagger \varphi_0$. Whereas the second excited manifold can be generated from the ground state in two different

ways:

$$\varphi_Q = (Q^\dagger)^2 \, \varphi_0 \,, \quad \varphi_B = B^\dagger \, \varphi_0 \,, \tag{3.13}$$

where φ_Q represents the second COM dipole excitation and φ_B the first internal breathing excitation. φ_Q and φ_B have the same energy and are in fact linear superpositions of φ_{2a} and φ_{2b} represented by Fig. 3.1(c). By repeatedly applying $Q^\dagger$ and $B^\dagger$ to the ground state, we can generate two families of excited states correspond to the COM dipole excitations and internal breathing excitations, respectively. In our dimensionless units, the nth COM dipole mode $(Q^\dagger)^n \, \varphi_0$ has excitation frequency n, and the nth internal breathing mode $(B^\dagger)^n \, \varphi_0$ has excitation frequency $2n$.

For the mapping we discussed earlier, the charge degrees of freedom of a strongly interacting harmonically trapped spinor gas is mapped to a spinless Fermi gas interacting with the p-wave pseudo-potential V_p given in Eq. (2.30). Since V_p only affects in the internal degrees of freedom, the separation of the COM motion and internal motion discussed above remains valid. An immediate conclusion one can draw is that V_p would not affect the energies of the COM dipole states generated by $Q^\dagger$ as $[V_p, Q^\dagger] = 0$. Consequently, the COM dipole excitation frequencies are not shifted by the interaction. This is simply the manifestation of the Kohn-Sham theorem for a system of harmonically trapped particles. A direct consequence of this is that the coefficients in the spin-chain Hamiltonian $H_{\text{sc}}^{(1)}$ for the first excited state (see Eq. (3.10)) are the same as the corresponding coefficients in $H_{\text{sc}}^{(0)}$ for the ground state (see Eq. (3.1)), i.e., $C_i^{(1)} = C_i^{(0)}$. Hence the two spin-chain Hamiltonians, $H_{\text{sc}}^{(1)}$ and $H_{\text{sc}}^{(0)}$, only differ by a constant shift of $E^{(1)} - E^{(0)} = 1$, which is the frequency of the lowest COM dipole mode.

Now let us turn to the second excited manifold which contains two degenerate states φ_Q and φ_B defined in Eq. (3.13). Due to the fact that $Q^\dagger$ is a COM operator,

and both $B^\dagger$ and V_p affect only the internal motion, the interaction does not couple φ_Q and φ_B. As a result, we can write down the effective spin-chain Hamiltonians for these two states separately:

$$H_{\mathrm{sc}}^{Q,B} = E^{(2)} - \frac{1}{g} \sum_{i=1}^{N-1} C_i^{(Q,B)} \left(1 \pm \mathcal{E}_{i,i+1}\right). \tag{3.14}$$

Furthermore, for the same reason that $C_i^{(1)} = C_i^{(0)}$, we also have $C_i^{(Q)} = C_i^{(0)}$. Hence $H_{\mathrm{sc}}^{(Q)}$ and $H_{\mathrm{sc}}^{(0)}$ also differ only by a constant shift of $E^{(2)} - E^{(0)} = 2$, which is the frequency of the second COM dipole mode. Quite amazingly, there also exists a simple relation between C_i^B and $C_i^{(0)}$ which can be proved using a recursion relation for the SO(2,1) algebra [25, 50](See Appendix B for more discussion):

$$\frac{C_i^B}{C_i^{(0)}} = 1 + \frac{3}{2(N^2 - 1)}, \tag{3.15}$$

which means that $H_{\mathrm{sc}}^{(B)}$ and $H_{\mathrm{sc}}^{(0)}$, apart from a constant shift of $E^{(2)} - E^{(0)} = 2$, only differ by a constant factor given in Eq. (3.15). The energy difference between the ground states of $H_{\mathrm{sc}}^{(B)}$ and $H_{\mathrm{sc}}^{(0)}$, which gives the frequency of the lowest breathing mode ω_B, is therefore

$$\omega_B = 2 + \frac{3}{2(N^2 - 1)} E_g, \tag{3.16}$$

where $E_g = \langle H_{\mathrm{sc}}^{(0)} \rangle - E^{(0)}$ is the ground state energy of the spin-chain Hamiltonian $H_{\mathrm{sc}}^{(0)}$ measured with respect to $E^{(0)}$. Hence, unlike the COM dipole mode, the breathing mode frequency receives an interaction-dependent shift away from the non-interacting value of 2. In the strongly interaction regime, this shift $\delta\omega_B \equiv \omega_B - 2 \propto 1/g$ and vanishes exactly in the TG limit of $g = \infty$.

3.4.2 Collective Modes

Let us now take a further look at the breathing mode, which is the first collective excitation mode whose frequency ω_B, given in Eq. (3.16), has a nontrivial interaction

dependence. ω_B is completely determined by the ground state energy of the spin-chain Hamiltonian $H_{\text{sc}}^{(0)}$. For a system of spinor Bose gas with *arbitrary* spin and arbitrary population distribution among spin components, it is quite obvious that the ground state of $H_{\text{sc}}^{(0)}$ is obtained by arranging the atoms into a fully spin symmetric configuration such that $\langle \mathcal{E}_{i,i+1} \rangle = 1$, and correspondingly the ground state energy is given by

$$E_g^{\text{boson}} = -\frac{2}{g} \sum_{i=1}^{N-1} C_i^{(0)} , \tag{3.17}$$

which, for a given trapping potential, only depends on the total number of atoms N. Under the local density approximation (LDA), we can obtain semi-analytic expressions for $C_i^{(0)}$, from which, we can show(For more details see Appendix C) that, for $N \gg 1$

$$E_g^{\text{boson}} = -\frac{1}{g}\frac{128\sqrt{2}}{45\pi^2}N^{5/2} \approx -\frac{1}{g}0.408N^{5/2} , \tag{3.18}$$

which is consistent with the result obtained previously for spinless bosons near the TG limit [39, 51, 52]. Correspondingly, the interaction-induced shift of the breathing mode frequency is

$$\delta\omega_B^{\text{boson}} = \frac{3}{2(N^2 - 1)} E_g^{\text{boson}} \approx -\frac{1}{g}\frac{64\sqrt{2}}{15\pi^2} N^{1/2} . \tag{3.19}$$

The fermionic case is more complicated. For a spin-s Fermi gas with a fully spin antisymmetric configuration, its ground state energy is the same as in the bosonic case, given by Eq. (3.17), as the two systems possess the same spatial wave function. This spin configuration, however, can only occur if the number of spin components $2s + 1 \geq N$ and no more than 1 fermions occupy the same spin component [35]. Otherwise the fully spin antisymmetric configuration cannot be reached and thus the ground state energy E_g^{fermion} for a spinor Fermi gas satisfies $E_g^{\text{boson}} \leq E_g^{\text{fermion}} \leq 0$.
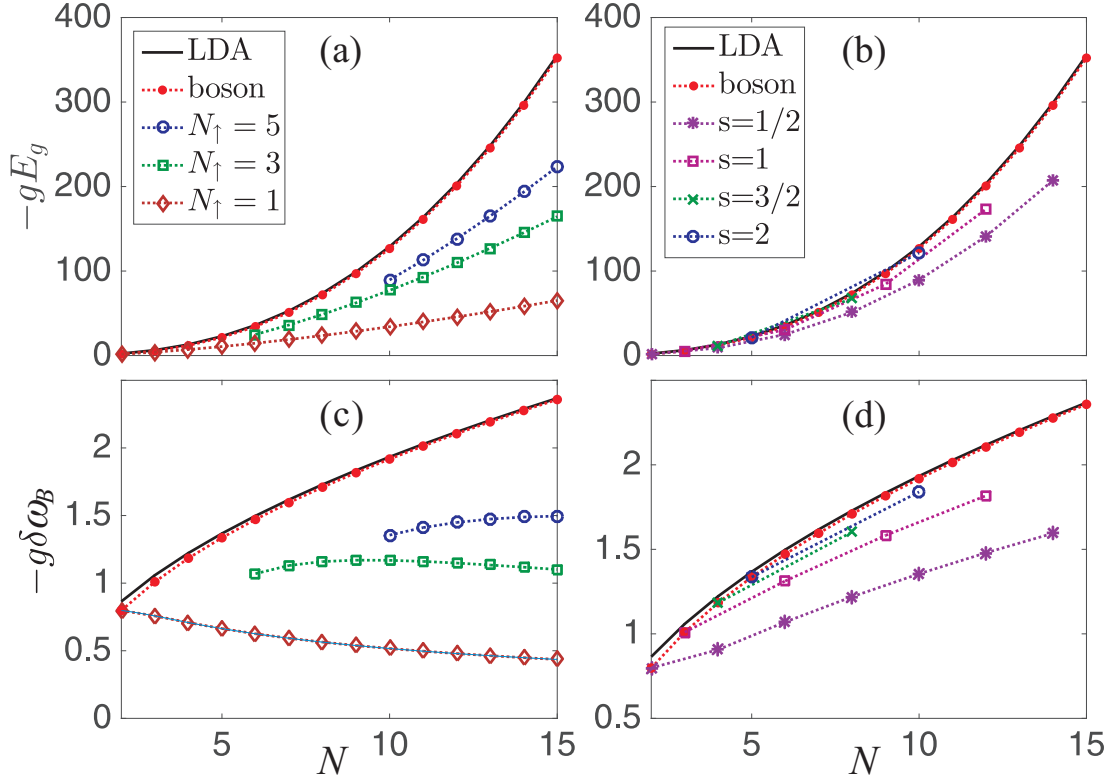
Figure 3.8 : (color online) Ground state energy (a, b) and breathing mode frequency shift (c, d) as functions of N. In (a) and (c), we present results for bosons and spin-1/2 fermions with various $N_\uparrow/N$. In (b) and (d), we present results for bosons, and fermions with different spin s and equal population in each spin component. For bosons, the ground state energy and the breathing mode frequency shift are independent of spin. The black solid lines represent the analytic LDA results for bosons given in Eqs. (3.18) and (3.19).

In Fig. 3.8(a), we plot the spin-chain ground state energy E_g as functions of total atom number N, with the corresponding breathing mode frequency shift $\delta\omega_B$ plotted in Fig. 3.8(c). The symbols are obtained by numerically calculate the coefficients $C_i^{(0)}$ and then diagonalize the spin-chain Hamiltonian $H_{\text{sc}}^{(0)}$. The red dots are the results for bosons. We also plot the analytical results based on LDA (Eqs. (3.18) and (3.19)) as black solid lines. As one can see, the LDA results agree very well with the numerical results even for small N. Other symbols in the figure correspond to E_g and $\delta\omega_B$ for spin-1/2 Fermi gas with different population distribution in the two spin components. In Fig. 3.8(b) and (d), we plot respectively E_g and $\delta\omega_B$ as functions of N for Fermi gases with different spin s and equal population in each spin component. As one can see, for fixed N, as s increases, the fermionic results approach the bosonic ones. As $2s+1 \geq N$, the two results matches exactly. This behavior has been recently seen in the experiment [30].

3.4.3 Quench dynamics with Spatial Degrees of Freedom

Finally, we demonstrate the application of multi-branch spin-chain model to simulate the dynamics of the system. To this end, we consider a spin-1/2 Fermi gas ($N_\uparrow = N_\downarrow = 2$) initially prepared in a harmonic trap subject to a spin-dependent magnetic gradient that separates the COM position of the two spin components, see the inset in Fig. 3.9. The presence of the magnetic gradient will modify the spin-chain Hamiltonian accordingly (See Appendix F). At $t = 0$, the magnetic gradient is quenched to zero and we plot the COM separation between the two spin components, Δ, in Fig. 3.9 as a function of time. This situation is examined in Section 3.2.5 using the single-branch spin-chain Hamiltonian $H_{\text{sc}}^{(0)}$, benchmarked with the numerically unbiased TEBD calculation. These are reproduced in Fig. 3.9 as green dotted line and
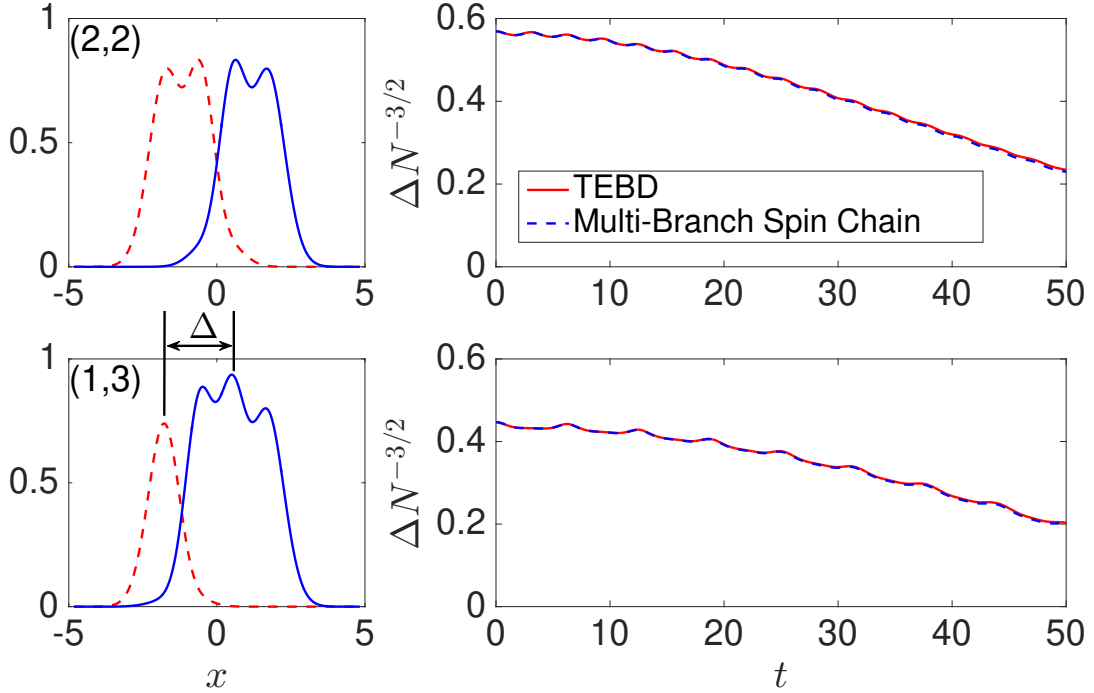
Figure 3.9 : (color online) Evolution of the spin separation after a sudden quench of the spin-dependent magnetic gradient for a harmonically trapped spin-1/2 Fermi gas with $N_\uparrow = N_\downarrow = 2$ and $g = 100$. The green dotted line is obtain from the ground state spin-chain model under Hamiltonian $H_{\text{sc}}^{(0)}$. The blue dashed line, shifted down by 0.05 for clarity, is obtained from the multi-branch spin-chain model by including 8 excited branches. The red solie line is the TEBD result. The inset shows the initial density profiles for spin-up (dashed line) and spin-down (solid line) components.

red solid line, respectively. For the short time scale we plotted, Δ decreases in time. The single-branch spin-chain result captures this behavior, but could not produce the small-amplitude oscillations that can be clearly seen in the TEBD simulation. The blue dashed line (shifted for clarity) is obtained by the multi-branch spin-chain simulation, in which we included 8 excited branches. The multi-branch spin-chain result shows excellent agreement with the TEBD calculation. Further analysis shows that the small-amplitude oscillation is mainly due to the coupling to the lowest breathing mode which can only be captured if the second excited manifold is included in the spin-chain model.

3.5 Advantages of the Effective Spin-Chain Models

We have shown here, for large interaction strength $|g|$, the original Hamiltonian 1.1 can be map into a spin-chain model governed the by the effective Hamiltonian H_{eff} in the form of Eq. (3.1), Eq. (3.10) or Eq. (3.11) which is expected to completely describe the physics of the upper branch in the strongly interacting regime. The great advantage of the effective model is that (1) it provides valuable insights into the quantum magnetic properties of strongly interacting one dimensional quantum gases, and (2) it is much easier and more efficient to solve in comparison to the original many-body Hamiltonian. We have benchmarked the static properties of the effective model with several unbiased methods (see Fig. 3.2 and Fig. 3.5).

As we have mentioned earlier, several other groups have obtained the same spin-chain effective Hamiltonian using a variational method [24, 25, 53, 54]. Our perturbational approach [22] is originally inspired by the similar technique used to construct effective spin models from Hubbard Hamiltonian in the large-U limit. Using this technique, the super-exchange interaction arises naturally. The Hubbard Hamilto-

nian describes lattice systems. Our work thus broadens this approach to a continuum model. From the perturbation calculation presented in this work, we may readily obtain many-body wave functions accurate to order $1/g$. Furthermore, it is in principle possible to extend the perturbation approach to higher orders to obtain more accurate results. These features will be exploited in the future to study more detailed properties of the system.

Another great advantage of the spin-chain model is its wide applicability [53]. The effective Hamiltonians 3.1, 3.10, 3.11 are valid for spinful Bosons or Fermions. The coefficients C_i, as given in Eq. (3.2), only depend on the total number of atoms and the external trapping potential, and are independent of whether the particles are Bosons or Fermions, nor are they dependent on the single particle spin s. The formalism to derive the effective Hamiltonian is independent of particle numbers N. Hence it works for any N.

3.6   Super-Exchange Interactions in Lattice Models

In the derivation of the spin-chain model Eq. (3.1, 3.10, 3.11) in above sections, we used the continuous models. As we have mentioned earlier, our perturbational approach is inspired by the similar technique used to construct effective spin models from Hubbard Hamiltonian in the large-U limit. The Hamiltonian for 1D Fermi Hubbard model is:

$$H = -t \sum_{i=1,\sigma}^{N} (c_{i,\sigma}^{\dagger} c_{i+1,\sigma} + h.c. + V_i n_i) + U \sum_{i=1}^{N} n_{i,\uparrow} n_{i,\downarrow}. \tag{3.20}$$

Where $c_{i,\sigma}^{\dagger}(c_{i,\sigma})$ are Fermionic creation(annihilation) operators on site i for spin σ, $n_{i,\sigma} = c_{i,\sigma}^{\dagger} c_{i,\sigma}$ is the local spin density operator, and $n_i = \sum_{\sigma} n_{i,\sigma}$ is the local density operator. It is helpful to point out here that by discretizing the continuous Hamilto-

nian 1.1, we can obtain a discretized form for the continuous model, which has the same form as Eq. (3.20) with a conversion of model parameters between continuous and discretized model as in Eq. (1.3).

For the lattice Hubbard model Eq. (3.20), at strong coupling region $U \to \infty$, an effective t-J model [55], can be derived

$$
\begin{aligned}
H_{t-J} = & -t \sum_{i,\sigma} (a_{i,\sigma}^{\dagger} a_{i+1,\sigma} + h.c. + V_i n_i) + \frac{2t^2}{U} \sum_i \left[\vec{S}_i \vec{S}_{i+1} - \frac{1}{4} n_i n_{i+1} \right] \\
& + \frac{t^2}{U} \sum_{i,\sigma} \left[a_{i,\sigma}^{\dagger} n_{i+1,\sigma} a_{i+2,\sigma} - a_{i,\sigma}^{\dagger} a_{i+1,\bar{\sigma}}^{\dagger} a_{i+1.\sigma} a_{i+2,\bar{\sigma}} \right] ,
\end{aligned}
\tag{3.21}
$$

where $a_{i,\sigma}^{\dagger} = c_{i,\sigma}^{\dagger} (1 - n_{i,\bar{\sigma}})$ is the projected Fermion operator, i.e. hard core Fermion operator, where $\bar{\sigma} = -\sigma$ is the opposite of spin σ. These hard core Fermion operators will ensure that the Hilbert space of the $t-J$ model does not include double occupancy states. And $\vec{S}_i$ are local spin operators in second quantized form.

$$
\vec{S}_i = \sum_{\alpha,\beta} \vec{S}_{\alpha,\beta} a_{i,\alpha}^{\dagger} a_{i,\beta}.
\tag{3.22}
$$

Where $\vec{S}_{\alpha,\beta} = \frac{1}{2} \vec{\sigma}_{\alpha,\beta}$ is the matrix elements of Pauli matrices. And $n_i = \sum_{\sigma} n_{i,\sigma}$ is the local density operator. The first term in Eq. (3.21) is the hopping term, the second term is the super-exchange interaction for two sites, and the third term is the super-exchange interaction for three sites. For Hubbard model at half-filling, the number of particles equals to the number of sites. In this case, for hardcore Fermions, the first and third term will vanish. This means the spatial degrees of freedom will vanish, and only the spin degrees of freedom remains. The second term is a spin Hamiltonian, which is just the Heisenberg model with nearest neighbor interaction. Here we want to mention that the t-J model and the discretized p-wave Hamiltonian 2.31 are consistent at large interaction and small lattice constant, but the discretized p-wave Hamiltonian can be used for arbitrary interaction strength,

since it is regularized by a counter term.

We expect the same results as in Section 3.1 and 3.4 will be obtained by first discretizing the continuous model of Eq. (1.1) and then apply the technique of obtaining the $t - J$ model on the discretized model. Actually, we can use perturbation theory on the t-J model to obtain an effective spin-chain model, especially when there is a large charge gap due to the trapping potential $V_i n_i$. When t^2/U is very small, first diagonalize the kinetic term, and an eigenfunction can be written as

$$\Psi(i_1, \sigma_1, ..., i_N, \sigma_N) = \varphi(i_1, i_2..., i_N)\chi, \tag{3.23}$$

where

$$\varphi(i_1, i_2..., i_N) = \det \begin{bmatrix} \varphi_{i_1}^0 & \varphi_{i_2}^0 & \cdots & \varphi_{i_N}^0 \\ \varphi_{i_1}^1 & \ddots & & \\ \vdots & & \ddots & \\ \varphi_{i_1}^{N-1} & & & \varphi_{i_N}^{N-1} \end{bmatrix}, \tag{3.24}$$

where $\varphi(i_1, i_2..., i_N)$ is a slater determinant with φ_i^m being single particle eigenstates of the free Hamiltonian. Eq. (3.23) can be regarded as a SCAW for lattice models. We write it into a direct product form, because for lattice Fermion models we label the direct product basis as

$$|i_1\sigma_1, i_2\sigma_2, ..., i_N\sigma_N\rangle = a_{i_1,\sigma_1}^\dagger a_{i_1,\sigma_1}^\dagger \cdots a_{i_N,\sigma_N}^\dagger |0\rangle \tag{3.25}$$

with spatial indices only in one spatial sector $i_0 < i_1 < ... < i_{N-1}$. Same as continuous case, χ is a spin wavefunction. Here we also first ignore charge state degeneracies. In first order perturbation in t^2/U, We can obtain the effective spin-chain model for the lattice model as

$$H_{eff} = -\frac{t^2}{U} \sum_{l=1}^{N-1} C_l(1 - \mathcal{E}_{l,l+1}), \tag{3.26}$$

with the coupling coefficients calculated by

$$C_l = \langle\varphi| \sum_{j=1}^{L} \delta_{\sum_{i=1}^{j-1} n_i, l-1} \left[2n_j n_{j+1} - a^\dagger_{j+2} n_{j+1} a_j - a^\dagger_{j-1} n_j a_{j+1} \right] |\varphi\rangle \,, \qquad (3.27)$$

where φ is the spatial wavefunction defined in Eq. (3.24). $\delta_{\sum_{i=1}^{j-1} n_i, l-1}$ projects the state that there are $l-1$ particles on the left of site j to ensure consistency with the spin-chain system with respect to site l and $l+1$. And the spin labels of $a^\dagger_j$ and a_j are eliminated since they only act on spatial states.

Similarly, we can also obtain the spin-charge separated form of one-body density matrix, $\rho_{\sigma',\sigma}(x',x) = \frac{1}{N} \langle\Psi| a^\dagger_{x',\sigma'} a_{x\sigma} |\Psi\rangle$ for lattice SCAWs (3.23):

$$\rho_{\sigma',\sigma}(x',x) = \sum_{m,n} \rho_{mn}(x',x) S_{mn}(\sigma',\sigma) \,, \qquad (3.28)$$

which has the same form as continuous models. The sectored spatial OBDM is now a multi-dimensional sectored summation

$$\rho_{mn}(x',x) = \frac{1}{N} \sum_{\Gamma_{mn}} \varphi^*(i_2, ..., i_m, x', i_{m+1}, ..., i_N) \varphi(i_2, ..., i_n, x, i_{n+1}..., i_N) \,, \qquad (3.29)$$

where

$$\Gamma_{mn} = i_2 < .... < i_m < x' < ... < i_n < x... < i_N \,. \qquad (3.30)$$

and $S_{mn}(\sigma',\sigma)$ has the same form as continuous models. The techniques used for calculating OBDM for continuous models in Chapter 4 also applies here.

Here we want to mention that the coupling constants in the spin-chain model are essential quantities in the effective spin-chain theory. They involves sector multi-dimensional integral for continuous models or summation for lattice models. The comparison of the continuous spinor quantum gas model and lattice Hubbard shows the spin-chain models arise from super-exchange interaction, thus it is naturally related to the itinerant quantum magnetism phenomenon.

There is also a spacial property for the continuous model, note that when discretizing the continuous model to lattice models, we need to specify a very small lattice constant, if we tune the lattice constant towards zero, the result lattice model will have filling goes to zero, the probability of double occupancy will go to zero. As a result, it is possible to map any continuous spinor quantum gas model to a hard core spinor gas model, which corresponds to the generalized Bose-Fermi mapping in Chapter 2.

Chapter 4

Strong Coupling Ansatz Wavefunctions

In this chapter, we discuss more properties of the Strong Coupling Ansatz Wavefunctions (SCAWs) first discussed in Section 2.1, Eq. (2.6). We rewrite the full form of SCAW in the following:

$$\Psi_{\varphi,\chi}(x_1,...x_N,\sigma_1,...\sigma_N) = \sum_{P \in S_N} (\pm 1)^P P(\varphi^1(x_1,...x_N)\chi(\sigma_1,...\sigma_N)). \qquad (4.1)$$

Where $\varphi^1 = \varphi\theta^1$ is an arbitrary spatial function only nonzero in θ^1 spatial sector define in Eq. (2.2). φ can be an arbitrary anti-symmetric function. $\Psi_{\varphi,\chi}$ is the (anti-)symmetric many-body wavefunction. For Bosons, plus sign is selected, while for Fermions, minus sign is selected. Thus the full wavefunction is symmetric for Bosons and anti-symmetric for Fermions. As discussed in Section 2.4, a SCAW can be mapped to a direct product of a spinless fermion wavefunction and a spin wavefunction:

$$\Psi_{\varphi,\chi} \leftrightarrow \varphi \otimes \chi \,, \qquad (4.2)$$

which is the foundation of the generalized Bose-Fermi mapping from the original (anti-)symmetric representation to the SCSR, and more details are in Chapter 2.

We organize this chapter as follows. We first provide an efficient way of calculating One-Body Density Matrices (OBDMs) in Section 4.1 and hence the momentum distribution, for the case when the spatial wavefunction φ is a slater determinant. We discuss translational invariant systems in Section 4.2, and show a relation of momentum distribution of spinor quantum gases and that of spinless anyon gases. We

discuss trapped systems in Section 4.3, where an more efficient way of calculating OBDMs for harmonic traps is provided. Finally in Section 4.4 we show that the momentum distribution of a single impurity moving in a background of strongly interacting spinless bosons, which was measured in a recent experiment [56], mimics that of a hard-core spinless anyon with a time-dependent statistical parameter.

4.1 One-Body Density Matrix and Hardcore Anyons

In this section we develop a technique to calculate the OBDM and the momentum distribution for a SCAW. This technique relies on a remarkable connection between the OBDM of the spinor gases and that of a spinless 1D hard-core anyon gases. It allows us to efficiently calculate the OBDM of the spinor system with particle numbers much larger than what was previously possible.

Given the OBDM, we can easily calculate the momentum distribution of the spinor system. Interestingly it is also related to the momentum distribution of the hard-core anyon gas. Our study not only provides a practical method for the calculation of the OBDM, but also provides significant new insights into the properties of 1D strongly interacting spinor quantum gases.

The expectation value of any single particle operators for spinor quantum gases system can be expressed in terms of OBDM.

$$\langle \Psi | \hat{O} | \Psi \rangle = \text{Tr} \left[\hat{O} \hat{\rho} \right], \tag{4.3}$$

Consider a spinor quantum gas with N atoms. The explicit form for a strong coupling ansatz wave function with a single spatial wave function φ (often referred to as the charge state in literature, which describes the particles distribution in position space) is written as Eq. (4.1). The corresponding OBDM associated with the many-

body wave function Ψ is defined as

$$\rho(x', x; \sigma', \sigma) = N \sum_{\sigma_1,...,\sigma_{N-1}} \int dx_1...dx_{N-1} \Psi^*(x_1, ..., x_{N-1}, x'; \sigma_1, ..., \sigma_{N-1}, \sigma')$$
$$\cdot \Psi(x_1, ..., x_{N-1}, x; \sigma_1, ..., \sigma_{N-1}, \sigma) . \tag{4.4}$$

Substituting Eq. (4.1) into Eq. (4.4), we have

$$\rho(x', x; \sigma', \sigma) = \sum_{\sigma_1 \cdots \sigma_{N-1}} \int dx_1 \cdots dx_{N-1} \varphi'^* \varphi \sum_{P'P} \theta'^{P'} \theta^P \otimes (P' \chi'^\dagger)(P\chi) , \tag{4.5}$$

where we have used the short-hand notation

$$\varphi' = \varphi(x_1, ..., x_{N-1}, x') , \varphi = \varphi(x_1, ..., x_{N-1}, x) ,$$

$$\chi' = \chi(\sigma_1, ..., \sigma_{N-1}, \sigma') , \chi = \chi(\sigma_1, ..., \sigma_{N-1}, \sigma) .$$

To evaluate the above equation, we need to order x' and x with respect to $x_1, ..., x_{N-1}$. For example, assuming $x' < x$, we can take $x' \in (x_{m-1}, x_m)$ and $x \in (x_{n-1}, x_n)$ with $m \le n$, and denote this ordering configuration as $\Gamma_{m,n}$, in which

$$\Gamma_{m,n} : \quad x_1 < ... < x_{m-1} < x' < x_m < ... < x_{n-1} < x < x_n < ... < x_{N-1} . \tag{4.6}$$

Once the ordering of x' and x are fixed, all permutations on $1 \cdots N - 1$ will lead to the same integral value, because these kind of permutations does not change either $\theta'^{P'} \theta^P$ or $(P' \chi'^\dagger)(P\chi)$. According to this observation, the OBDM (4.5) can be written as [22, 57](For a detailed derivation, see Appendix E)

$$\rho(x', x; \sigma', \sigma) = \sum_{m,n=1}^{N} \rho_{m,n}(x', x) S_{m,n}(\sigma', \sigma) . \tag{4.7}$$

Equation (4.7) takes a kind of "spin-charge" separated form: The spatial part

$$\rho_{m,n}(x', x) = (-1)^{n-m} N! \int_{\Gamma_{m,n}} dx_1...dx_{N-1} \, \varphi'^* \, \varphi , \tag{4.8}$$

depends only on the charge state φ. The information on the spin degrees of freedom is carried by the spin correlation function(Appendix E)

$$S_{m,n}(\sigma', \sigma) = (\pm 1)^{m-n} \langle \chi | S_m^{\sigma', \sigma}(m \cdots n) | \chi \rangle \, , \tag{4.9}$$

(again, ± 1 for bosonic and fermionic gases, respectively) where $S_m^{\sigma', \sigma}$ is a local $\mathrm{SU}(N)$ generator ($S^{\sigma', \sigma} | \sigma \rangle = | \sigma' \rangle$) on site m, and $(m \cdots n)$ is a loop permutation operator that permutes the indices in the wavefunction by $m \to m+1, m+1 \to m+2, ..., n-1 \to n, n \to m$(Appendix A). In the above, we have assumed that $m \leq n$. The case with $m \geq n$ can be obtained using the identity $\rho_{m,n}(x', x) = \rho_{n,m}(x, x')$ and $S_{m,n}(\sigma', \sigma) = S_{n,m}(\sigma, \sigma')$.

The difficulty of evaluating the OBDM lies in the fact that Eq. (4.8) involves an $(N-1)$-dimensional integral. With sophisticated numerical techniques, one may be able to carry out such an integral up to $\sim N = 20$ [57]. Here we develop a new method to evaluate $\rho_{m,n}(x', x)$, which relies on its discrete Fourier transform given by:

$$\rho_{m,n}(x', x) = N^{-2} \sum_{\kappa, \kappa'} \rho^{\kappa', \kappa}(x', x) \, e^{i\pi\kappa'm} \, e^{-i\pi\kappa n} \, , \tag{4.10}$$

where κ and κ' take a discrete set of values $2k/N$ with N consecutive integers k, and

$$\rho^{\kappa', \kappa}(x', x) = N \int dx_1 ... dx_{N-1} \prod_{j=1}^{N-1} A^{\kappa'*}(x_j - x') A^{\kappa}(x_j - x) \, \varphi'^* \, \varphi \, , \tag{4.11}$$

where $A^{\kappa}(x_i - x_j) \equiv e^{i\pi(1-\kappa)\theta(x_i - x_j)}$, with $\theta(x)$ being the Heaviside step function. Remarkably,

$$\Psi^{\kappa}(x_1, ..., x_N) = \left[\prod_{i<j} A^{\kappa}(x_j - x_i) \right] \varphi(x_1, ..., x_N) \, , \tag{4.12}$$

is the wave function of N hard-core spinless anyons [58, 59] with statistical parameter κ (we use the convention in Ref. [60–62]), whose OBDM, $\rho^{\kappa}(x', x) \equiv \rho^{\kappa, \kappa}(x', x)$, is given exactly by Eq. (4.11) with $\kappa' = \kappa$. The case with $\kappa = 0$ and 1 correspond to the

hard-core spinless bosons and the ideal spinless fermions, respectively. By defining a similar Fourier transform for the spin correlation function

$$S^{\kappa',\kappa} = N^{-2} \sum_{m,n=1}^{N} S_{m,n} e^{i\pi\kappa'm} e^{-i\pi\kappa n} \,,$$

we can rewrite Eq. (4.7), the OBDM of a strongly interacting spinor quantum gas, as

$$\rho(x',x;\sigma',\sigma) = \sum_{\kappa',\kappa} \rho^{\kappa',\kappa}(x',x) S^{\kappa',\kappa}(\sigma',\sigma) \,. \tag{4.13}$$

There has been an extensive study of the properties of 1D hard-core spinless anyon gases [58–82] (and the references therein). In particular, their OBDM and momentum distributions have been calculated. We can take advantage of these results to evaluate Eq. (4.13) in a very efficient way. In the following, we present two examples, one concerns a homogeneous system with translational invariance and the other a harmonically trapped system. And for both of these two cases, we consider φ as the ground state slater determinant.

4.2 Translational Invariant System

For a translational invariant system with length L (periodic boundary condition is assumed), the OBDM $\rho(x',x;\sigma',\sigma)$ depends only on $y \equiv x - x'$, and Eqs. (4.7) and (4.13) are reduced to

$$\begin{aligned} \rho(y;\sigma',\sigma) &= \sum_{r=0}^{N-1} \rho_r(y)\, S_r(\sigma',\sigma) \\ &= \sum_{\kappa} \rho^{\kappa}(y) S^{\kappa}(\sigma',\sigma) \,, \end{aligned} \tag{4.14}$$

where r in the first line is understood as $n-m$, so from Eq. (4.9) we have $S_r(\sigma',\sigma) = (\pm1)^r \langle\chi|S_m^{\sigma',\sigma}(m...m+r)|\chi\rangle$ which is independent of m, and in the second line $S^{\kappa} = N^{-1}\sum_{r=0}^{N-1} S_r e^{-i\pi\kappa r}$ only depends on spin. To ensure the boundary condition, we

need to impose the selection rule $(1...N)\chi = (\mp 1)^{N-1}\chi$ on the spin state χ with ∓ 1 for bosonic and fermionic gases, respectively. After Fourier transform with respect to y, the corresponding momentum distribution for the spinor quantum gas can be obtained as

$$\rho_\sigma(p) = \sum_\kappa \rho^\kappa(p) \, S^\kappa(\sigma, \sigma) \,, \tag{4.15}$$

where $\rho^\kappa(p)$ is the momentum distribution for the hard-core anyon system. Note that ρ^κ and S^κ are periodic in κ with period 2. Hence we may restrict κ in the range $[-1, 1]$.

The OBDM for the homogeneous hard-core anyon gas, $\rho^\kappa(y)$, has an analytic expression in the form of the Toeplitz determinant [60–62]. Its momentum distribution, $\rho^\kappa(p)$, is investigated in Ref. [62]. It is shown that $\rho^\kappa(p)$ is peaked at $p = \kappa\hbar k_F$, where $k_F = N\pi/L$ is the Fermi momentum, for $\kappa \in (-1, 1)$. Whereas for $\kappa = \pm 1$, the system becomes an ideal spinless Fermi gas whose momentum distribution is characterized by the Fermi sea. Examples of $\rho^\kappa(p)$ for $N = 201$ are shown in Fig. 4.2(c).

To find the OBDM and the momentum distribution of a spinor gas, all we need to do is to calculate the spin correlation functions $S_r(\sigma', \sigma)$ or $S^\kappa(\sigma', \sigma)$ and plug it into Eqs. (4.14) and (4.15). For 1D system, Matrix Product State (MPS) is a representation that efficiently captures the bipartite entanglement, and many powerful methods based on this representation such as Density Matrix Renormalization Group (DMRG) and Time-Evolving Block Decimation (TEBD) have been developed to calculate the ground state and the time evolution. We calculate the ground state $S_r(\sigma', \sigma)$ using the infinite system size TEBD (iTEBD) method [83, 84]. We first calculate the A, B tensors (two sites in one unit cell), which are building blocks in Matrix Product States (MPS), using iTEBD. Note that $S_r(\sigma', \sigma)$ is the correlation function containing a loop permutation operator $(m...m + r)$, so we use the tensor contraction geome-
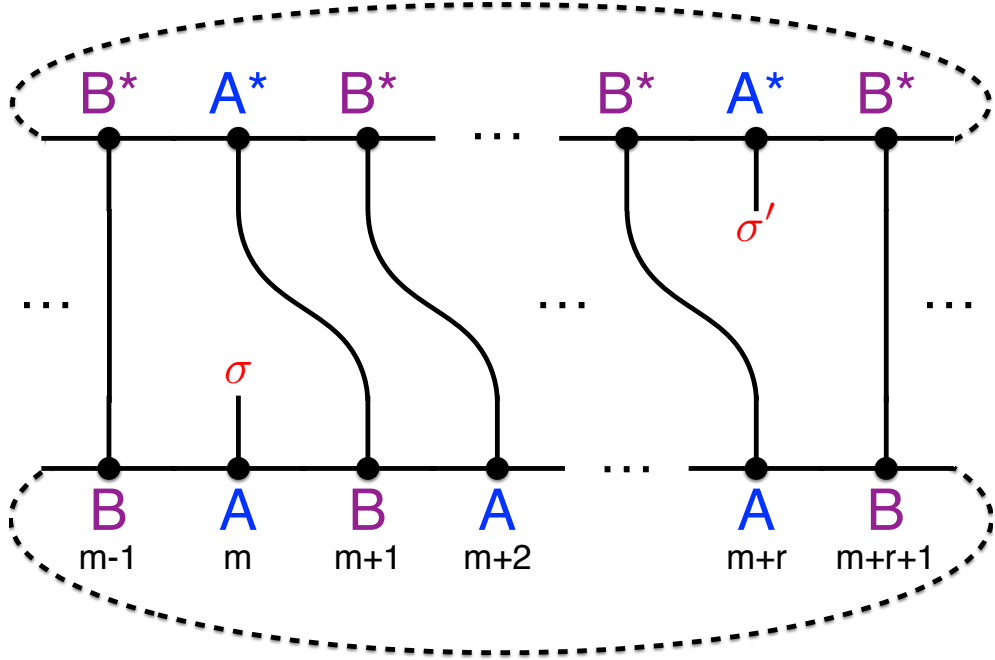
Figure 4.1 : (color online) The tensor contraction geometry for calculating $S_r(\sigma', \sigma)$ for an even r case. A and B tensors, which are building blocks in MPS (two sites in a unit cell), are calculated using the iTEBD method. Note that for a finite periodic boundary condition system, we also need to contract the remaining tensors outside the correlation range m to $m + r$. Starting from the mth site with either A tensor or B tensor gives the same result.

try schematically shown in Fig. 4.1 to calculate $S_r(\sigma', \sigma)$, and then take the Fourier transform to obtain $S^\kappa(\sigma', \sigma)$.

As examples, we consider a spin-1/2 and a spin-1 Fermi gases with spin independent interaction with $N = 201$. The corresponding spin-chain models in the strong interaction limit are the SU(2) and the SU(3) Sutherland models, respectively [23]. The spin correlation functions $S_r = \sum_\sigma S_r(\sigma, \sigma)$ and $S^\kappa = \sum_\sigma S^\kappa(\sigma, \sigma)$ are plotted in Fig. 4.2(a) and (b), respectively. The total momentum distribution functions $\rho(p) = \sum_\sigma \rho_\sigma(p)$ for the spinor gas are shown in Fig. 4.2(d). The spinor quantum gas

in strongly repulsive regime has been studied within the context of spin-incoherent Luttinger liquid [85], and the ground state momentum distribution for SU(2) case has been studied in Ref. [86–88], the result in Fig. 4.2(d) can be compared with Fig. 3 in Ref. [86] which is for a lattice system and for up to 32 sites with a quarter filling (note that their definition of k_F differs from ours by a factor of 2). Here we want to mention that a sophisticated method developed in Ref. [88] can be used to efficiently calculate $\rho(p)$ for homogeneous spin-1/2 fermions, but our method is more flexible and much more general as it deals with bosonic or fermionic systems with arbitrary spin.

4.3 Trapped System

For trapped systems, the OBDM is calculated using Eq. (4.13), where $\rho^{\kappa',\kappa}(x',x)$ is defined with Eq. (4.11). Unlike in the homogeneous system, we now need both the diagonal elements with $\kappa = \kappa'$ and the off-diagonal elements with $\kappa \neq \kappa'$, the latter of which can be regarded as a straightforward generalization of the OBDM of a spinless anyon gas. For the case that φ is a slater determinant composed of single particle wave functions $\phi_j(x)$ with $j = 1, 2, ..., N$ simply being labels, which means we can separate the coordinate x as

$$
\begin{aligned}
&\varphi(x_1, ..., x_{N-1}, x) \\
=&\frac{1}{\sqrt{N!}} \sum_P (-1)^P P(\phi_1(x_1)\phi_2(x_2)...\phi_{N-1}(x_{N-1})\phi_N(x)) \\
=&\frac{1}{\sqrt{N!}} \sum_{n=1}^N (-1)^{N-n}\phi_n(x)\det\left[\phi_{1,...,n-1,n+1,...,N}^{x_1,...,x_{N-1}}\right] ,
\end{aligned} \tag{4.16}
$$

similarly for $\varphi^*(x_1, ..., x_{N-1}, x')$. We need to substitute them into Eq. (4.11). First combine the fully symmetric direct product function $\prod_{j=1}^{N-1} A^\kappa(x_j - x)$ with
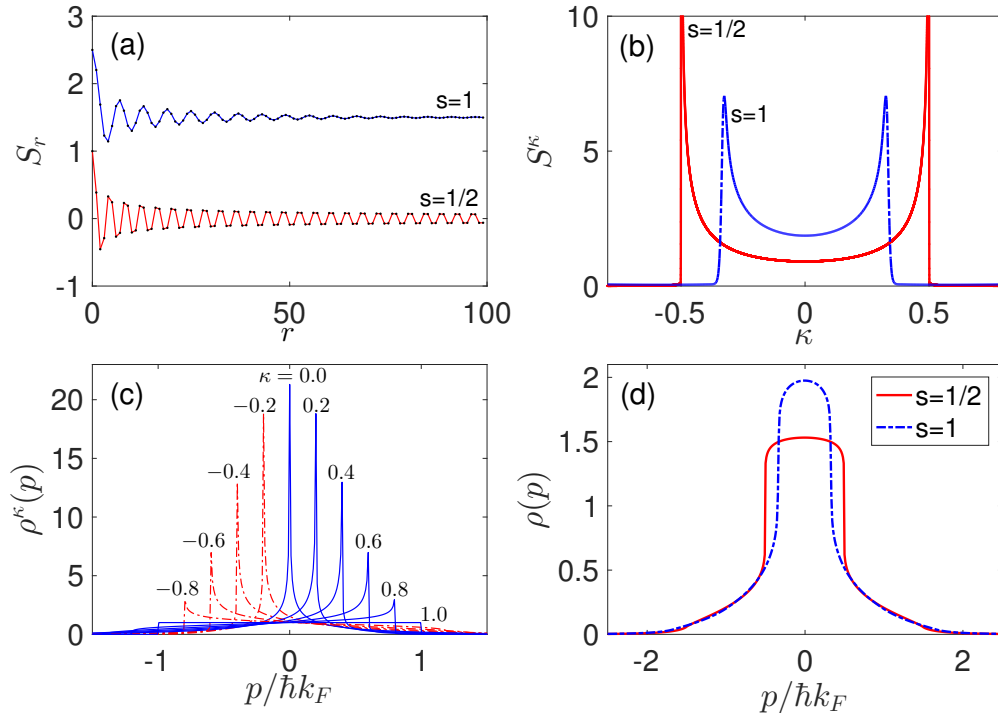
Figure 4.2 : (color online) Spin correlation function and momentum distribution of translational invariant system. **(a)** S_r calculated by iTEBD for an infinite chain. **(b)** S^κ obtained by Fourier transform of S_r with r up to 10000. **(c)** Momentum distribution of hard-core anyon gas $\rho^\kappa(p)$ for N=201. **(d)** Momentum distribution (summed over all spin components) of the spinor gases for N=201 particles. Note that in Eq. (4.15), $\rho^\kappa(p)$ and S^κ are not generally real valued as in **(b)(c)**, but we can rearrange $\rho_r(y)$ and S_r to make them real. For a system with periodic boundary condition, for odd (even) N, $\rho^\kappa(p)$ and S^κ are only purely real (imaginary) when $\kappa = 2m/(N-1)$ with integer m. In Eq. (4.15), we use $\kappa = 2m/N$. But we can redefine $\rho^\kappa(p)$ and S^κ to make them real by rearranging $\rho_r(y)$ and S_r to make them mirror symmetric about $y = 0$ and $r = 0$. For small number of particles, this leads to small oscillations in $\rho^\kappa(p)$ and S^κ(no effect on $\rho(p)$). But these oscillations tend to vanish in the thermodynamic limit.

$\det\left[\phi_{1,...,n-1,n+1,...,N}^{x_1,...,x_{N-1}}\right]$ to form a new determinant

$$\prod_{j=1}^{N-1} A^{\kappa}(x_j - x)\det\left[\phi_{1,...,n-1,n+1,...,N}^{x_1,...,x_{N-1}}\right] \tag{4.17}$$

$$=\det\left[(A^{\kappa}(x) \circ \phi)_{1,...,n-1,n+1,...,N}^{x_1,...,x_{N-1}}\right],$$

where $A^{\kappa}(x) \circ \phi$ means using $A^{\kappa}(t - x)\phi_k(t)$ as basis of the slater determinant. Next using the identity

$$\int dx_1...dx_{N-1}\det\left[(A^{\kappa'*}(x') \circ \phi)_{1,...,m-1,m+1,...,N}^{x_1,...x_{N-1}}\right]$$

$$\cdot \det\left[(A^{\kappa}(x) \circ \phi)_{1,...,n-1,n+1,...,N}^{x_1,...x_{N-1}}\right] \tag{4.18}$$

$$=(N-1)!\det\left[\hat{\Phi}^{(m,n)}\right],$$

which can be easily proved, where (m, n) stands for minor, which is the determinant of a matrix after deleting its mth row and n^{th} column, and the matrix $\hat{\Phi}$ depends on κ', κ, x', x, with its elements given by

$$\hat{\Phi}_{k,l}^{\kappa',\kappa}(x', x) = \int_{-\infty}^{\infty} dt A^{\kappa'*}(t - x')A^{\kappa}(t - x)\phi_k^*(t)\phi_l(t), \tag{4.19}$$

where $\phi_{k,l}$ are single-particle wave functions and $k, l = 1, 2, ..., N$. Finally putting Eqs. (4.16) $\sim$ (4.18) together, Eq. (4.11) can be written into a form with only minors of a determinant:

$$\rho^{\kappa',\kappa}(x', x) = \sum_{m,n}(-1)^{m-n}\phi_m^*(x')\phi_n(x)\det\left[\hat{\Phi}^{(m,n)}\right]. \tag{4.20}$$

 The expression Eq. (4.3) is much simpler than the previous formulas for OBDM as reported in Ref. [57], which rely on the calculation of Taylor coefficients of matrix determinants using sophisticated methods [2, 57, 89–91].

4.3.1   Harmonically Trapped System

For the most experimentally relevant harmonically trapped systems, an even simpler form of the OBDM can be obtained as follows. Note that wave function φ of a har-

monically trapped spinless fermion can be written into a Vandermonde determinant
form:

$$
\begin{aligned}
\varphi(x_1, ..., x_N) &= \frac{1}{\sqrt{N!}} \det \left[\phi_{0,1,...,N-1}^{x_1,...,x_N} \right] \\
&= C_N^{1/2} \prod_{j=1}^{N} e^{-x_j^2/2} \prod_{1 \le j < k \le N} (x_j - x_k),
\end{aligned} \tag{4.21}
$$

where $\phi_{0,1,...,N-1}^{x_1,...,x_N}$ means the slater determinant uses single particle harmonic oscillator
wave functions $\phi_k(x)(k = 0, 1, ..., N-1)$ as basis. And

$$
C_N = \frac{2^{N(N-1)/2}}{\pi^{N/2} \left[\prod_{n=1}^{N} n! \right]} \tag{4.22}
$$

is a normalization constant. This leads to

$$
\varphi(x_1, ..., x_{N-1}, x) = C_N^{1/2} e^{-x^2/2} \prod_{j=1}^{N-1} (x_j - x) \prod_{j=1}^{N-1} e^{-x_j^2/2} \prod_{1 \le j < k \le N-1} (x_j - x_k), \tag{4.23}
$$

which after substituting into Eq. (4.11), and using the $N-1$ version of Eq. (4.21),
we have

$$
\begin{aligned}
&\rho^{\kappa',\kappa}(x', x) \\
&= N C_N e^{-\frac{x'^2 + x^2}{2}} \int dx_1 ... dx_{N-1} \prod_{j=1}^{N-1} A^{\kappa'*}(x_j - x')(x_j - x') A^{\kappa}(x_j - x)(x_j - x) \\
&\quad \cdot \prod_{1 \le j < k \le N-1} (x_j - x_k)^2 \prod_{j=1}^{N-1} e^{-x_j^2} \\
&= \frac{N C_N e^{-\frac{x'^2 + x^2}{2}}}{C_{N-1}(N-1)!} \int dx_1 ... dx_{N-1} \prod_{j=1}^{N-1} A^{\kappa'*}(x_j - x')(x_j - x') A^{\kappa}(x_j - x)(x_j - x) \\
&\quad \cdot \left(\det \left[\phi_{0,1,...,N-2}^{x_1,...,x_{N-1}} \right] \right)^2 .
\end{aligned} \tag{4.24}
$$

Now by using a similar procedure as in arbitrary trapping potential case that leads to
Eq. (4.3), we can combine the product of $\prod_{j=1}^{N-1} A^{\kappa'*}(x_j - x')(x_j - x') A^{\kappa}(x_j - x)(x_j - x)$
into the square of a determinant to form a square of a new determinant, and then

carry out the $(N-1)$-dimensional integral. Finally we arrive at the following:

$$\rho^{\kappa',\kappa}(x',x) = \frac{e^{-(x'^2+x^2)/2}}{\pi^{1/2}}\det\left(\hat{B}\right) , \qquad (4.25)$$

where the elements of the matrix $\hat{B}$ are

$$\begin{aligned}\hat{B}_{k,l}^{\kappa',\kappa}(x',x) &= 2/\sqrt{(k+1)(l+1)} \\ &\times \int_{-\infty}^{\infty} dt\, A^{\kappa'*}(t-x')A^{\kappa}(t-x)(t-x')(t-x)\phi_k^*(t)\phi_l(t),\end{aligned} \qquad (4.26)$$

where $\phi_{k,l}$ are single particle eigen wave functions of harmonic oscillator, and $k,l = 0,1,...,N-2$.

The OBDM of a harmonically trapped hard-core spinless anyon gas $\rho^\kappa(x',x) = \rho^{\kappa,\kappa}(x',x)$ have been investigated previously [78–80] (for hard-core spinless Bose gas, see Ref. [81,82]).

4.4 Impurity in a Tonks-Girardeau Gas

As a concrete example, we consider a recent experiment [56] where Bloch oscillation of a single impurity atom moving in the background of a strongly interacting spinless Bose gas (i.e., the Tonks-Girardeau gas) is observed. Here, we explain this phenomenon using the strong coupling ansatz with the spin-chain model theory, which is a different perspective from previous theoretical studies [92–95].

We model the system as a spin-1/2 Bose gas with atomic mass m, confined in a harmonic trap with trapping potential ω, with one spin-↓ atom as the impurity and $(N-1)$ spin-↑ atoms as the background. Strong repulsive interaction exists between the background atoms, and also between the background and the impurity atoms. In this strong interaction regime, we can write down a spin-chain model. However, for this particular system with one single impurity, we can model the dynamics of the impurity atom as if it hops on an effective lattice under the influence of a constant

force F. It can be easily proved that the Hilbert space of this one atom hopping model and that of the spin-chain model governed by Hamiltonian 3.1 with one spin impurity are equivalent. The Hamiltonian of the one atom hopping model takes the following form (setting $\hbar = m = \omega = 1$)

$$
\begin{aligned}
H_{sc} = & -\frac{\pi}{\sqrt{2N}\gamma_i} \sum_{j=1}^{N-1} C_j \left[c_j^\dagger c_{j+1} + h.c. \right] \\
& + \left[\frac{1}{\pi}\sqrt{2N} \right]^3 \mathcal{F} \sum_{j=1}^{N-1} D_j n_j ,
\end{aligned}
\tag{4.27}
$$

where $\gamma_i = mg_i/\hbar^2 n_{1D}$ is the dimensionless interaction constant, with $n_{1D} = \sqrt{2N}/\pi$ the density at trap center, and g_i the contact interaction strength between the impurity and the background atoms.[1] H_{sc} is a single-atom Hamiltonian. $c_j^\dagger$ and c_j are creation and annihilation operators for this single atom, and $n_j = c_j^\dagger c_j$ are local density operators. The first line of (4.27) represents the kinetic term and the second line the force term. The coupling coefficients C_j can be calculated using a special local density approximation method.[2] The force on the impurity is modeled as a magnetic gradient and represented by the second line in (4.27) where $\mathcal{F} = mF/\hbar^2 n_{1D}^3$ and $D_j = C_{j-1} - C_j$ (assuming $C_0 = C_N = 0$) [91].

We take the initial spin state to be the ground state of Hamiltonian (4.27) in the absence of the force term, which subsequently evolves in time under the full Hamilto-

---

[1] The exchange between two background atoms only contributes a constant energy shift, which can be ignored. This is why the interaction strength between the background atoms do not appear in the Hamiltonian (4.27).

[2] C_i can be very well approximated by a local density approximation(LDA) method as reported in Ref. [91]. In [57], C_i has been calculated up to $N = 60$ particles by an exact method, an method similar to those used in [2, 89, 90]. And we have checked that the relative difference between LDA results and those reported in [57] tend to vanish as $N \to \infty$. And we also want to note here that Ref. [25] gives a very simple approximated expression $C_j \propto j(N - j)$ with great accuracy.

nian (4.27). With the instantaneous spin state obtained by solving the Schrödinger equation [3], and using the method outlined above, we can calculate the momentum distribution of the impurity spin which we plot on the left panel of Fig. 4.3. The initial momentum distribution is peaked at $p = 0$ as expected. This peak moves towards the Fermi point $\hbar k_F$ as the impurity is under the influence of the force. When the peak reaches $\hbar k_F$, it disappears and re-emerges at the other Fermi point $-\hbar k_F$. Thus the impurity atom carries out the Bloch oscillation. Our calculation agrees qualitatively with the experiment of Ref. [56].

Another interesting aspect of this experiment is that the measured momentum distribution of the impurity atom is approximately the momentum distribution of a hard-core anyon gas with a time-dependent statistical parameter κ. To see this, let us ignore the trapping potential, which is not essential for the Bloch oscillation dynamics, and assume that the system is homogeneous for simplicity. In this case, the initial spin state has exactly zero momentum with $S^\kappa = \delta_{\kappa,0}/N$. If γ_i is sufficiently large, we may ignore the hopping term, i.e., the first line of Hamiltonian (4.27). Under this approximation, the spin correlation function evolves simply as $S^\kappa(t) = \delta_{\kappa, Ft/\hbar k_F}/N$. According to Eq. (4.15), the momentum distribution of the impurity atom at time t is thus given by

$$\rho(p, t) = \frac{1}{N} \rho^{Ft/\hbar k_F}(p) \,,$$

---

[3]Here we assume that the charge state of the system is frozen, which is given by the ground state Slater determinant of N spinless fermions in the harmonic trap. When the interaction strength γ_i is not very large and/or the force term is too large, this assumption becomes invalid and the dynamics may couple different charge manifolds. This situation, which better describes the experiment of Ref. [56], can be modeled using the multi-branch spin-chain model developed in our previous work [91]

which is exactly the momentum distribution of a hard-core anyon gas with a time-dependent statistical parameter $\kappa = Ft/\hbar k_F$. On the right panel of Fig. 4.3, we replotted the momentum distribution of the impurity atom obtained above at several different times (solid lines), and compared them with the momentum distribution of a homogeneous hard-core anyon gas with its density given by n_{1D}, particle number N, and $\kappa = Ft/\hbar k_F$ (dash-dotted lines). Good qualitative agreement can be seen. The main difference is that the distribution of the trapped impurity atom has a rounded peak, which can be mainly attributed to the effect of the trapping potential.
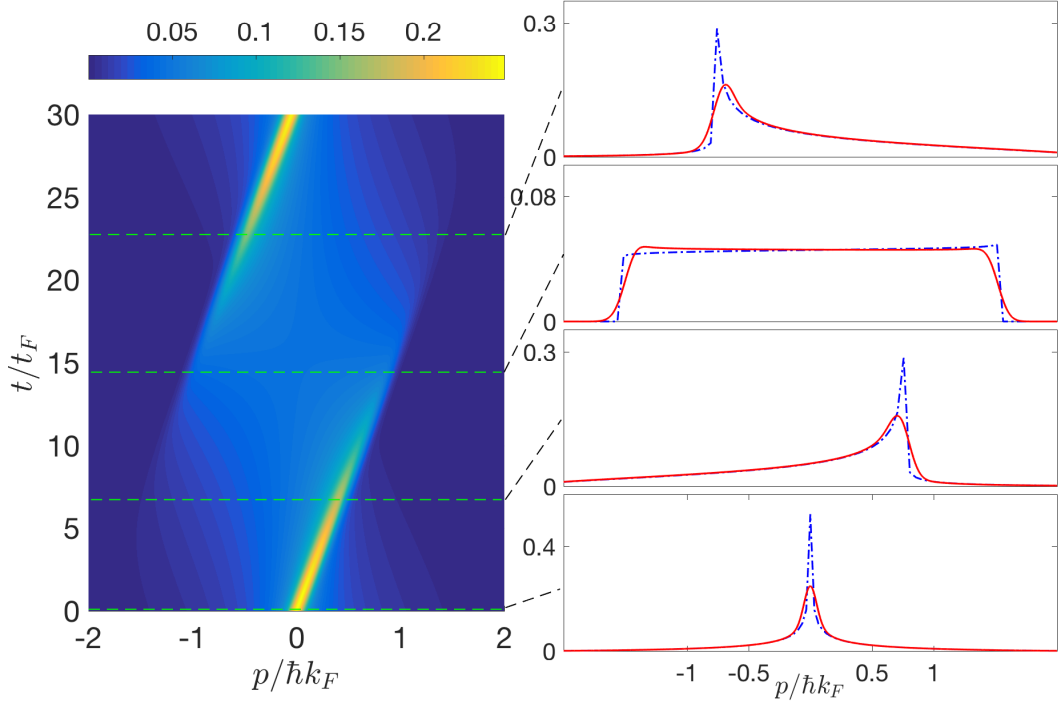
Figure 4.3 : (color online) Left panel: evolution of the momentum distribution of the impurity atom. Here we take $N = 60$, $\gamma_i = 12$, and $\mathcal{F} = 1$. $t_F = \hbar/E_F = 1/N$, and $k_F = n_{1D}\pi = \sqrt{2N}$ is the Fermi momentum. All quantities are expressed in the dimensionless unit system defined by $\hbar = m = \omega = 1$. Right panel: the solid lines replot the momentum distribution of the impurity atom from the left panel at four different times; the dash-dotted line is the momentum distribution of a homogeneous hard-core anyon gas, $\rho^\kappa(p)/N$, with statistical parameter $\kappa = Ft/\hbar k_F$. The anyon gas consists N particles confined in a region with length L (periodic boundary condition is assumed) such that its density is given by $N/L = n_{1D}$.

Chapter 5

Numerical Methods

In one-dimension, several numerical methods have given good precision results, such as Matrix Product State (MPS) bases methods including DMRG, TEBD, and Monte Carlo based methods including Variational Monte Carlo (VMC). In this section, we will discuss the numerical methods used for solving 1D spinor quantum gases and related systems.

5.1 Matrix Product States

MPS based methods are powerful in 1D and works especially well when the entanglement spectrum decays fast. This happens when the system has a finite energy gap at thermodynamic limit. When the entanglement spectrum decays slower than exponential, results with good precision can also be obtained through interpolation. In this section, we will discuss MPS based method for 1D continuous models.

5.1.1 MPS for Continuous Models

For continuous models, we first discretize them as in Eq. (1.2), then write the operators into Matrix Product Operators, and perform imaginary time evolution on a MPS. The parameters in the MPS are then optimized in the imaginary time evolution process. The ground state can be obtained in this way. After obtaining the ground state, we can do real time evolution on the ground state to study its dynamics. The results for few spin-1/2 Fermions are in Fig. 3.7.

5.1.2 iTEBD for Loop Permutation Correlation

Infinite size TEBD (iTEBD) can be used for calculating infinite system size translational invariant system. Two tensors are optimized in an alternative way, and correlation functions such as loop correlation operators can be calculated by contracting several replication of the two tensors, an example is in Fig. 4.1.

5.2 Variational Monte Carlo and Deep Learning

Recently Deep Learning (DL) has been very successful in many areas such as Computer Vision (CV), Natural Language Processing (NLP), Reinforcement Learning (RL) and other Artificial Intelligence applications. This is largely due to an integration of representational power of state-of-the-art designed deep network architectures, scalable learning algorithms and novel computer architectures [11] such as GPUs.

In physics, one of the most powerful numerical methods to solve quantum many-body problems is the Variational Monte Carlo (VMC) method. In VMC, a variational wavefunction is proposed to approximate the ground state (or low energy excited states), which is usually based on physical insights. And stochastic optimization is performed to minimize the energy functional. The energy functional and its derivatives involve a multi-dimensional integral (or summation) which can not be evaluated directly. So stochastic approximations for those quantities is performed by sampling state configurations using the Markov-Chain Monte Carlo (MCMC) method. Similar to a DL method for the image classification problem, where an image is the input into a neural network and the probability of the image being a certain class is the output, a quantum many-body state configuration is the input into a variational wavefunction, the output is the wavefunction value. Both of the two problems are about using a

Deep Neural Network (DNN) to approximate another function to be studied. So considering the success of various DNN architectures in Computer Vision, it is naturally to develop DNN architectures for approximating quantum many-body wavefunctions. And also by utilizing the current novel computer architectures, the efficiency of the algorithm will be dramatically improved.

Another advantage of developing neural network architectures is that previously in VMC algorithm, the variational wavefunctions are often proposed by physical insights about the system. If we can find some DNN architectures that are very general to approximate many kinds of wavefunctions, we will say there is some kind of machine intelligence that automatically solves certain aspects of quantum many-body problems. Also from those network architectures, we may also learn some new insights about the quantum many-body systems. Just as we can lean some insights from mean field theories.

Comparing with supervised learning for image classification, the VMC algorithm is more similar to the policy gradient method in RL, where a total reward value as a functional of a multi-dimensional policy function is minimized through stochastic sampling. However, the nature of Markov-Chain process makes the VMC algorithm not straightforward to be parallelized, thus not straightforward to run on the novel distributed computer architectures. To overcome this, we first do MCMC sampling of the states, then use an Off-Policy algorithm to update the parameters in the model with the sampled states and their local variables.

In this section, we first discuss the Off-Policy VMC algorithm that can utilize the current distributed computing architectures, such as GPUs. Then discuss various network architectures. And then the results of the Off-Policy VMC algorithm on SU(N) spin chains with multi-layer convolutional neural networks.

5.2.1 Off-Policy Variational Monte Carlo Algorithm

In Variational Monte Carlo(VMC) algorithm, the energy functional

$$E = \frac{\langle \Psi | H | \Psi \rangle}{\langle \Psi | \Psi \rangle} \tag{5.1}$$

is minimized in a stochastic way, such that the derivatives of E over parameters w in the variational wavefunction Ψ is approximated by

$$\partial_w E \approx 2\mathrm{Re} \left[\overline{E \cdot \partial_w \mathrm{ln}\Psi} - \overline{E} \cdot \overline{\partial_w \mathrm{ln}\Psi} \right] , \tag{5.2}$$

where the statistical average of an operator is defined as an average over all the sampled states

$$\overline{O} = \frac{1}{M} \sum_s O_s , \tag{5.3}$$

where M is the number of samples, s is usually sampled using a Markov-Chain that following probability proportional to $\Psi_s^* \Psi_s$, O_s is the local variable defined as

$$O_s = \frac{\sum_{s'} O_{s,s'} \Psi_{s'}}{\Psi_s} , \tag{5.4}$$

where $O_{s,s'}$ is the matrix elements of operator O. So that $\overline{E} = \sum_s E_s / M$ where $E_s = \sum_{s'} H_{s,s'} \Psi_{s'} / \Psi_s$, $\overline{\partial_w \mathrm{ln}\Psi} = \sum_s \partial_w \mathrm{ln}\Psi_s / M$, and $\overline{E \cdot \partial_w \mathrm{ln}\Psi} = \sum_s E_s \partial_w \mathrm{ln}\Psi_s / M$. E_s and $\partial_w \mathrm{ln}\Psi_s$ are called local energy and local derivative, respectively. After obtained an approximation Eq. (5.2), gradient based optimization algorithm can be used to update the parameters in the variational wavefunction Ψ, for example using Gradient Descent algorithm

$$w \leftarrow w - \alpha \partial_w E , \tag{5.5}$$

where α acts as the learning rate. In traditional VMC algorithm, the parameter is updated iteratively. In every iteration step, M states are sampled, and Eq. (5.2) is evaluated using those sampled states, then using Eq. (5.5), parameters are updated,

then next iteration begins. This means in every iteration parameters are only updated once. The traditional VMC is efficient because previously most of the variational wavefunctions are somewhat simple. In the Markov Chain update, usually local flips or swaps are performed, and the ratio of wavefunctions after and before the update can usually be calculated very efficiently. This makes the traditional VMC algorithm efficient in every iteration step, so many iterations can be performed to allow the algorithm converge. However, if we want to use DNNs as variational wavefunction, due to the complex architecture of DNNs, the Markov Chain sampling can not be performed efficiently, even if only using local updates, and also a single Markov Chain can not be calculated in parallel, which makes the sampling in every iteration step inefficient. And if we choose a small learning rate α, every iteration step only updates the parameters a little bit, so the algorithm takes long time to converge.

On the other hand, inspired by the Off-Policy method in the policy gradient algorithm in Reinforcement Learning, we can actually update the parameters many times with one set of samples. However, we can not simply use Eq. (5.3) for every optimization step, because after one step of updating parameters, the wavefunction changed, and by definition we can only use Eq. (5.3) when the probability distribution of states $\Psi_s^*\Psi_s$. Instead, we use an importance sampling method to calculate the statistical average in Eq. (5.3) using states under a different distribution from Ψ^2.

$$\overline{O} = \frac{C}{M} \sum_i \frac{|\Psi_{s_i}|^2}{|\Psi_{s_i}^0|^2} O_{s_i}, \tag{5.6}$$

where C is a normalization factor, because we assume the variational wavefunctions are not normalized. Formally,

$$C = \frac{\sum_s |\Psi_s^0|^2}{\sum_s |\Psi_s|^2}, \tag{5.7}$$

i.e. the ratio of the normalization for Ψ^0 and Ψ. Note that the summation is over

all states, which is exponentially many for quantum many-body problems. Here we need to deal with the undefined normalization for Ψ and Ψ^0. We simply assume the following identity, and from which can approximate C.

$$\frac{C}{M} \sum_i \frac{|\Psi_{s_i}|^2}{|\Psi^0_{s_i}|^2} = 1 \tag{5.8}$$

In summary, the importance sampling method for VMC algorithm has the following steps. Randomly initialize model parameters in the variational wavefunction. Sample a batch of states using the current wavefunction, Ψ^0. Iteratively do the following until algorithm converge. Calculate local energies and local derivatives for the sampled states. Calculate the expectation values in Eq. (5.3) using importance sampling Eq. (5.6) Update model parameters using Eq. (5.5)

Note that in the above algorithm, the local derivatives can be calculated by using auto differentiation in the current deep learning framework. For example in Tensorflow [96], we can define an effective loss function of the following form

$$L = \overline{E \cdot \ln\Psi} - \overline{E} \cdot \overline{\ln\Psi} \tag{5.9}$$

where the gradient can only flow back through $\ln\Psi$. So in every Off-Policy updating of the model parameters, the computation is similar to that of supervised learning optimization.

Fig. 5.1 shows a comparison of the iteration steps needed for the traditional VMC algorithm and the Off-Policy VMC algorithm to obtain a good energy. The number of optimization steps equals one means only update parameter once per iteration, which corresponds to traditional VMC algorithm. The Off-Policy algorithm uses much fewer steps to converge a good energy. And we would like to comment here that on CPU, the Off-Policy VMC algorithm does not have obvious speed up, but using GPU Eq. (5.2) can be computed much more efficient than using CPU, thus the
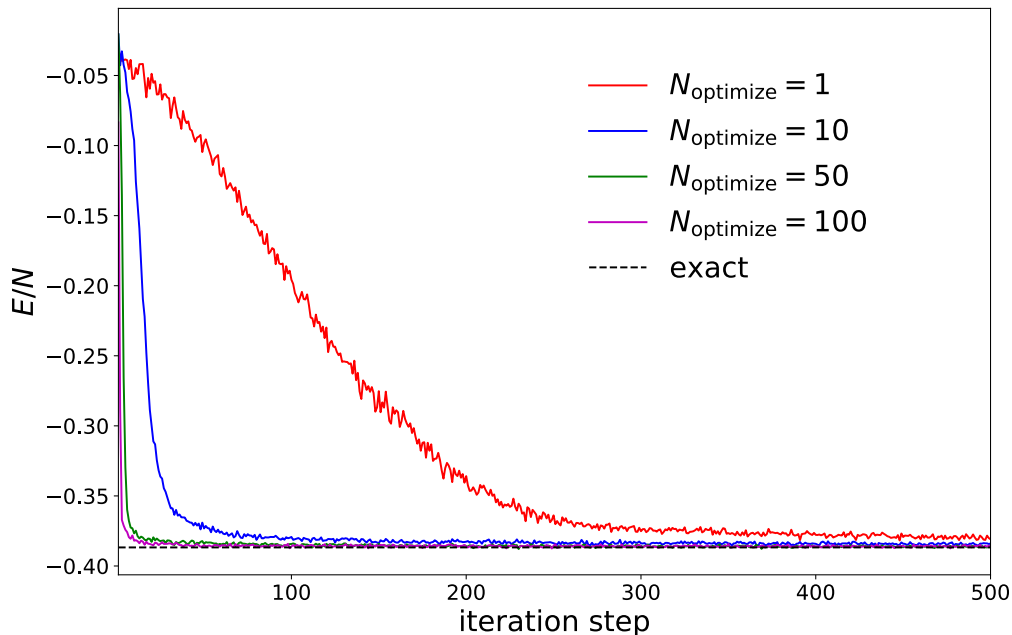
Figure 5.1 : (color online) Comparison of energy versus interaction step curves in the training process for different number of optimization steps (N_{optimize}) in every iteration. The system is a 60 sites SU(2) homogeneous spin-chain. We use 8 convolutional layers, and every layer has 8 filters with kernel size 3. $N_{\mathrm{optimize}} = 1$ corresponds to traditional VMC algorithm, i.e. update parameter only once in every iteration.

Off-Policy VMC will be much faster than traditional VMC on GPUs. In experiments, we observed at least one order of magnitude speed up using a Nvidia K80 GPU with 11G memory.

5.2.2   Neural Network Architectures

With the Off-Policy VMC algorithm running on distributed computing architecture hardwares such as GPUs, it is possible to train a DNN to represent quantum many-body wavefunctions given the Hamiltonian only. In this section, we review the neural network architectures for this purpose.

(Convolutional) Restricted Boltzmann Machines

Restricted Boltzmann Machine (RBM) has been first used in VMC algorithm in Ref. [97]. The RBM is a graphical model, and is a special case of the general Boltzmann Machine. The Boltzmann Machine is composed of a number of nodes, for clarity we assume each node has only binary values, 1 and -1. The probability of a given configuration, a assignment of the binary values to nodes, is given by

$$P(\vec{s}) = \frac{1}{\mathbb{Z}} e^{-\sum_{i<j} W_{ij} s_i s_j - \sum_i b_i s_i} \tag{5.10}$$

where $\mathbb{Z} = \sum_{\vec{s}} e^{-\sum_{i<j} W_{ij} s_i s_j - \sum_i b_i s_i}$ is the partition function acts as a normalization. W_{ij} are the weights (or coupling) that connecting node i and j, b_i is the bias (or on site potential) on node i. The form of the Boltzmann Machine probability distribution over state configurations is the same as the classical Ising models. This distribution has been served as variational functions to approximation some probability distributions.

The Restricted Boltzmann Machine has one more constraint that it is a bipartite Boltzmann Machine. The nodes can be separated into two groups, the visible nodes $\vec{v}$ and the hidden nodes $\vec{h}$. There is no direct weight that link two nodes within a same group. So the probability distribution can be written as

$$P(\vec{v}, \vec{h}) = \frac{1}{\mathbb{Z}} e^{-\sum_{i,j} W_{ij} v_i h_j - \sum_i a_i v_i - \sum_j b_j h_j} \tag{5.11}$$

i is the index for the visible node and j is the index for the hidden node. As usual $\mathbb{Z}$ is the partition function. Many RBM has been stacked together and form a deep model, which is the one of the first deep learning models used in computer vision area [98]. And novel sampling methods are also provided such as contrastive divergence algorithm [99]. For approximating quantum many-body wavefunctions, the hidden nodes

are integrated out, the remaining function of the visible nodes is thus

$$\Psi(\vec{v}) = e^{-\sum_i a_i v_i} \prod_j 2\cosh\left[\sum_i W_{ij} v_i + b_j\right] \tag{5.12}$$

Where $\vec{v}$ is now a state configuration.

Later it turns out that multi-layer convolutional neural networks can lead better results for many tasks. In this section we also consider convolutional RBM, which is the connection edge between the visible and hidden layer is of a convolutional form.

$$P(\vec{v}, \vec{h}) \frac{1}{\mathbb{Z}} e^{-\sum_i a_i v_i - \sum_j b_j h_j - \sum_i \sum_{k=-\lfloor \Delta/2 \rfloor}^{\lfloor \Delta/2 \rfloor} W_{ki} v_{i+k} h_i}, \tag{5.13}$$

where W_k is only a filter of size Δ (for notation simplicity, Δ is an odd integer). For clarity, in Eq. (5.13), we assume the number of visible and hidden nodes are the same. And the wavefunction by tracing off $\vec{h}$ is

$$\Psi(\vec{v}) = \frac{1}{\mathbb{Z}} e^{-\sum_i a_i v_i} \prod_i 2\cosh\left[\sum_{k=-\lfloor \Delta/2 \rfloor}^{\lfloor \Delta/2 \rfloor} W_{ki} v_{i+k} + b_i\right] \tag{5.14}$$

And we can further let the number of hidden nodes equals to α (an integer) times the number of visible nodes, and put every α hidden nodes into a group, and also impose translational symmetry on a_i and b_j, then the above Eq. (5.14) can be written into a convolutional form with multiple filters

$$\Psi(\vec{v}) = \frac{1}{\mathbb{Z}} e^{-a\sum_i v_i} \prod_i \prod_{f=1}^{\alpha} 2\cosh\left[\sum_{k=-\lfloor \Delta/2 \rfloor}^{\lfloor \Delta/2 \rfloor} W_k^f v_{i+k} + b^f\right], \tag{5.15}$$

where f is the index of filters, and $a = a_i$, $W_k^f = W_{ki}^f$, $b^f = b_i^f$ due to translational symmetry. The translational symmetric network architecture in Ref. [97] corresponds to the convolutional RBM with kernel size Δ equals to the system size, i.e. the fully connected case.

(Convolutional) Neural Networks

The convolutional RBM Eq. (5.15) contains a product of cosh functions. However, if we take the logarithmic of the wavefunction

$$\ln\Psi = \ln\mathbb{Z} - a\sum_i v_i + \sum_i \sum_{f=1}^{\alpha} \sigma\left(\sum_{k=-\lfloor\Delta/2\rfloor}^{\lfloor\Delta/2\rfloor} W_k^f v_{i+k} + b^f\right) \qquad (5.16)$$

where $\sigma(x) = \ln(2\cosh(x))$. The first term is a constant, the second term is a linear transform of the input state configuration, the last term is actually a one hidden layer convolutional neural network with activation function $\sigma(x)$, and also the weights of the hidden units to output is fixed to one, and there is no bias for the output. The activation function looks similar to the Rectified Linear unit (ReLu) function, but is symmetric and smooth around origin. However, according to the universal representation theory, many activation functions can have similar representation power, thus activation function may be not crucial. In this section, we use convolutional neural networks (CNN) to approximate many-body wavefunctions. One reason to use CNNs is that the Hamiltonians we are considering usually only have local interactions. And many systems whose groundstates have correlation functions decay very fast with respect to distance.

Fully Convolutional Neural Networks

In this work we explore the most simple and general network architectures, multi-layer neural networks with Rectified Linear Units (ReLU) activations, which has been used in computer vision studies and are proved to be effective. Since most quantum many-body systems contains only local interactions, CNNs are natural to use. In variational studies of quantum many-body wavefunctions, one of the simplest classes of variational wavefunctions is the mean field wavefunction. For spin system, mean

field wavefunctions are direct products of local spin wavefunctions $\Psi(\sigma_1, \sigma_2, ..., \sigma_N) = \prod_{i=1}^{N} \phi(\sigma_i)$. If we take a logrithim of the mean field wavefunction, we can obtain

$$\ln\Psi(\sigma_1, \sigma_2, ..., \sigma_N) = \sum_{i=1}^{N} \ln\phi(\sigma_i), \tag{5.17}$$

which can be regarded as a CNN with one hidden layer and kernel size 1. Then the feature maps of the hidden layer is reduce summed along the spatial dimension. We would like to keep this feature of mean field wavefunction even we are considering multi layer CNNs. So from the last hidden layer to the output, we perform a reduce sum along the spatial dimension, and then a small fully connected network to obtain the output. So the network is a Fully Connected Network (FCN). To simplify the study, we keep every CNN layer having the same kernel size, number of output channels. The number of input channels are the same except for the first CNN layer, whose number of input channels is decided by the encoding of input state. In this work, we consider two kinds of state encodings, value encoding and one-hot encoding. In value encoding, we use the values of local spins directly. In one-hot encoding, we encode the local spin states into a boolean vector. For example, the $|1\rangle$ state of a spin-1 local spin is encoded as $(0, 1, 0)$. In Fig. 5.2, we show the architectures of the network. Each magenta rectangular object corresponds to a convolutional filter with ReLu activation function. The number of channels of the input tensor is decided by the state encoding.

5.2.3   Imaginary Phases of Wavefunctions

The most general form is to use neural networks to approximate both the real and imaginary phases of the wavefunction

$$\Psi = e^{x+iy} \tag{5.18}$$
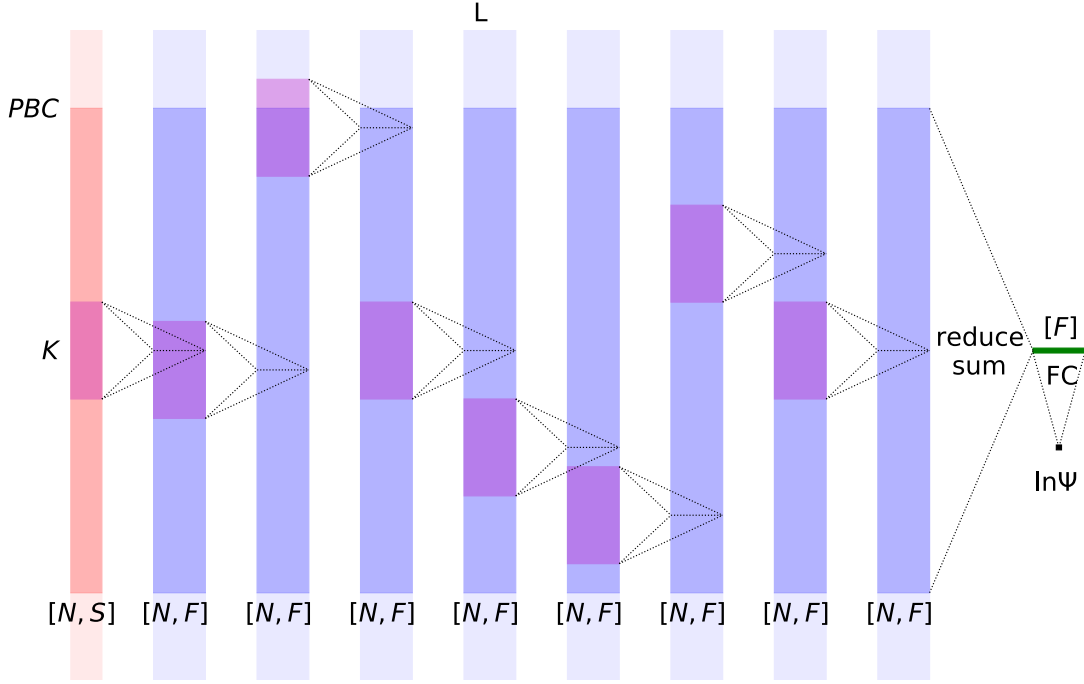
Figure 5.2 : (color online) Fully Convolutional Neural Network (FCNN) Architecture.

where two networks or a single network with two outputs should be used to approximate x and y, respectively.

When using two networks(or one network with two outputs) for representing x and y in Eq. (5.18), the stochastic approximation of the derivatives of the energy functional with respect to model parameters can be written as

$$\partial_w E = 2\mathrm{Re}\left[\overline{E^r \cdot \partial_w x} - \overline{E^r} \cdot \overline{\partial_w x} + \overline{H^i \cdot \partial_w y}\right],\qquad(5.19)$$

where the local energies

$$H_s^i = \sum_{s'} H_{ss'} e^{x_{s'} - x_s} \cos(y_{s'} - y_s),$$

$$H_s^r = \sum_{s'} H_{ss'} e^{x_{s'} - x_s} \sin(y_{s'} - y_s),$$

(5.20)

are the real and imaginary part of the local energy. For the case that we don't know the phase of the wavefunction, y should be optimized together with x, which is

numerically hard. However, when we know the exact phase of a wavefunction, only x need to be optimized. In the following, we only consider the case when we know the phase of the wavefunction.

5.2.4   One-Dimensional SU(N) Spin-Chains

In this section, we consider the following SU(N) symmetric model with site dependent couplings

$$H = \sum_i C_i \hat{P}_{i,i+1} \,, \tag{5.21}$$

where $\hat{P}_{i,i+1}$ is the spin exchange operator that $\hat{P}_{i,i+1} |\alpha, \beta\rangle = |\beta, \alpha\rangle$. We consider periodic boundary condition. C_i are some site dependent couplings. For Homogeneous cases $C_i = C$, Eq. (5.21) can be exactly solved using Bethe Ansatz [23]. We use the Off-Policy VMC with multi-layer Convolutional Neural Network to solve this model.

The ground state wavefunction of the Hamiltonian 5.21 is not positive definite. However, we can do a unitary transformation to make the wavefunction positive definite. When exchange two different spins, change a sign of the exchange operator, i.e. change $\hat{P}$ to $\hat{\tilde{P}}$ that

$$\hat{\tilde{P}} |\alpha, \beta\rangle = \begin{cases} |\beta, \alpha\rangle & \alpha = \beta \\ -|\beta, \alpha\rangle & \alpha \neq \beta \end{cases} \tag{5.22}$$

if we change the $\hat{P}$ operator to $\hat{\tilde{P}}$, the Hamiltonian 5.21 will have the exact same eigen spectrum, but the ground state wavefunction is positive definite.

First consider translational invariant cases, where Bethe Ansatz exact solutions are available. Bethe Ansatz can solve the energy spectrum efficiently, but it is hard to calculate wavefunction values or correlation functions. Variational wavefunctions such as DNN can efficient calculate the wavefunction values at any given state, or

calculate any physical measurables through sampling a batch of states. In this section, we explore multi-layer FCNNs with different numbers of sites N, numbers of spin components S, numbers of layers L, numbers of filters F and kernel sizes K.

5.2.5 Ground State Energy

Fig. 5.3 shows the results of different number of spin components with $N = 60$. Fig. 5.3(a)(b) uses value state encoding. For example a $S = 3$ system, the spin states can be labeled as $0, 1, 2$, and they are encoded into values $-1/2, 0, 1/2$. In Fig. 5.3(a), we use single hidden layer networks and keep number of filters fixed, increasing the kernel size, the energy results gets better. But for larger spin, the results are not so good (actually unstable). In Fig. 5.3(b), we keep the number of filters and kernel sizes fixed, increasing the number of layers, the energy results also get better and will eventually better than single hidden layer results. But for larger spin, it still shows saturation. But as can be seen from the inset figure of Fig. 5.3(b), the energy results can be improved by increasing the number of filters or the kernel size. The results in Fig. 5.3(a)(b) shows when using value encoding of of spin states, DNNs will give better results than shallow NNs.

However, we can use different encodings of a spin state, which will keep the FCNN architecture of the network. Fig. 5.3(c)(d) use one-hot state encoding. For example, the spin states $0, 1, 2$ of a $S = 3$ system are encoded into boolean vectors $(1, 0, 0), (0, 1, 0), (0, 0, 1)$. As can be seen in Fig. 5.3(c), even single layer network will give good results comparing with multi-layers with value encoding. And as in Fig. 5.3(d), multi-layer network with one-hot encoding can also give good results. And the results can also be further improved by increasing the number of filters or kernel size.
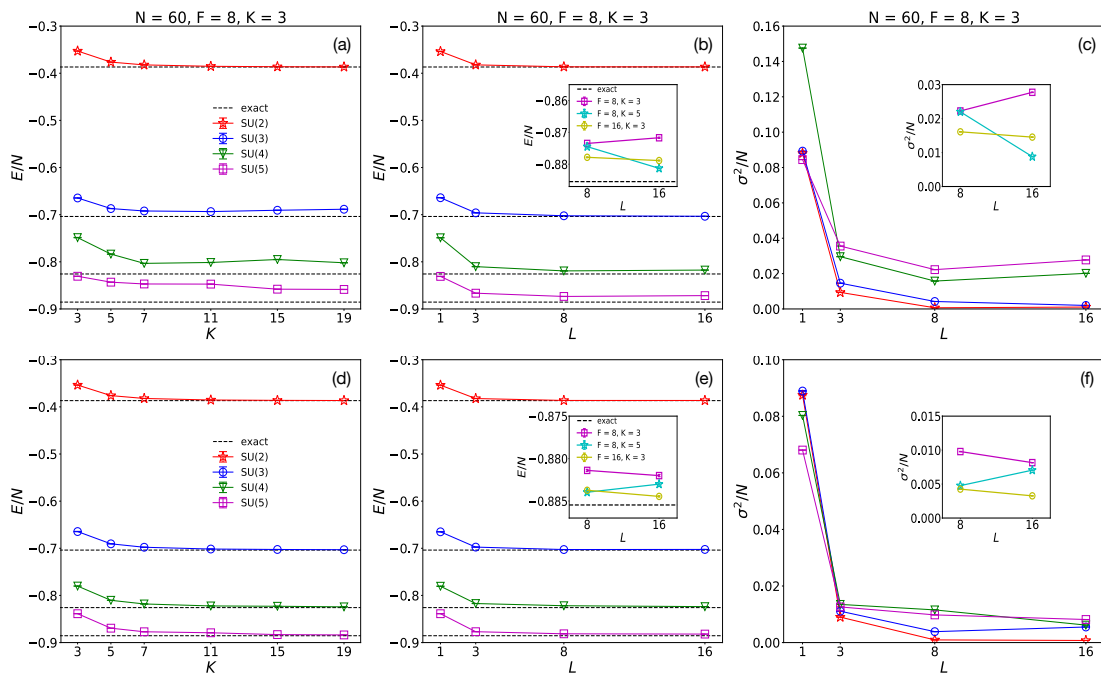
Figure 5.3 : (color online) The ground state energies and variances for different network architectures and state encodings. (a)(b)(c) are for state value encoding. (d)(e)(f) are for state one-hot encoding. (c)(e) are the energy variances.

5.2.6 Loop Permutation Correlation Functions

The states of a strongly interacting spinor Fermi gases [100] can be described by a strong coupling ansatz wavefunction [22, 25, 91, 101, 102]. Its one-body density matrix can be written into a summation of spin-charge direct product form [22, 101, 102]:

$$\rho(x', x) = \sum_{m,n=1}^{N} \rho_{m,n}(x', x) S_{m,n} , \qquad (5.23)$$

where the spin part is a spin loop permutation correlation function,

$$S_{m,n}(\sigma', \sigma) = (-1)^{m-n} \langle \chi | (m \cdots n) | \chi \rangle , \qquad (5.24)$$

where $(m \cdots n)$ is a loop permutation operator that permutes the indices in the wavefunction by $m \to m+1, m+1 \to m+2, ..., n-1 \to n, n \to m$. In this section, we consider translational invariant system, so we can define $S_r = S_{m,m+r}$. Fig. 5.4(a) shows the loop permutation correlation functions S_r of FCNN wavefunctions for a $N = 60$ systems [103]. Fig. 5.4(b) shows the discrete Fourier transform of S_r. As can be seen, the S_r and S_k results can consistent with previous studies. The peak in S_k at $\pm 1/S$ suggests the singularities of momentum distributions of strongly interacting spinor Fermi gases at k_F/S [86, 101], where $k_F = n\pi$ is the Fermi momentum, and n is the particle density.

5.2.7 Transfer Learning

The network architecture is a fully convolutional neural network, which allows us the use the same set of parameters for different system size. This is the way transfer learning does. In Fig. (5.5), we first train a CNN on system size 40, SU(2), then used the trained parameter as initialization parameter to train on system size 100, SU(2). We found that comparing with random initialization for system size 100, SU(2), using
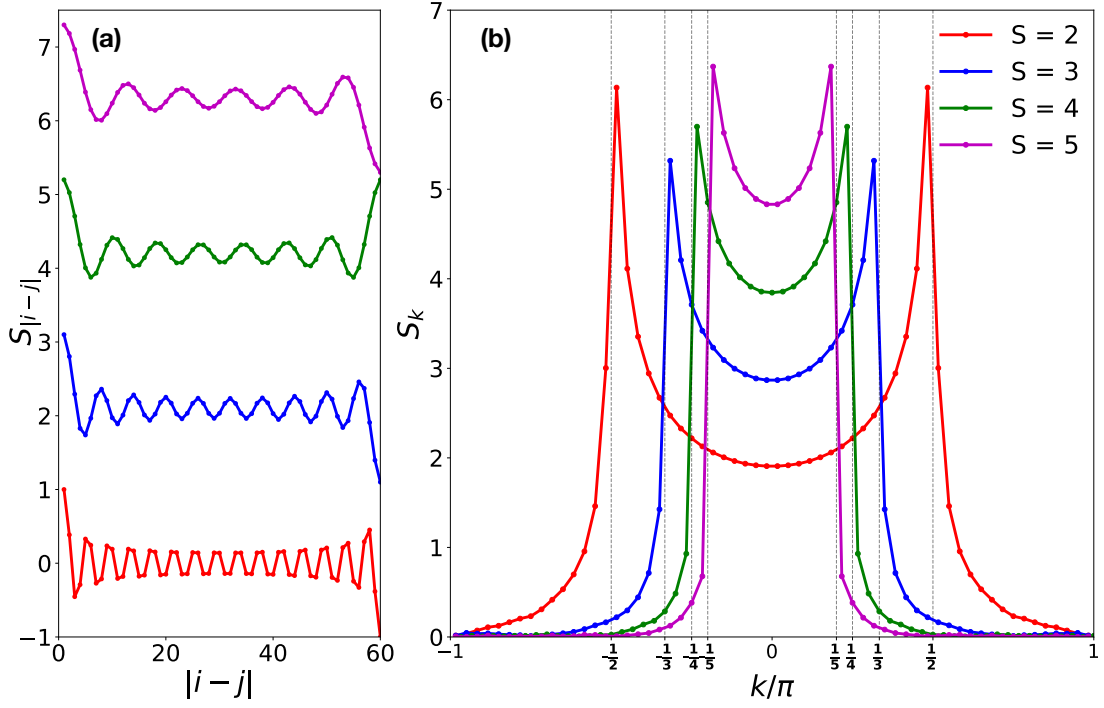
Figure 5.4 : (color online) Loop permutation correlation functions (a) for S_r and (b) for S_k.

parameters trained on system size 40, SU(2) will initially has much lower energy. And also in experiment, we found the training process is stable than random initialization, which may due to for small system size, the Markov Chain sampling will run for a larger ratio of the whole Hilbert space, and thus the parameters are less likely to overfit on a small ratio of the whole Hilbert space, which is often the case when system size is larger.
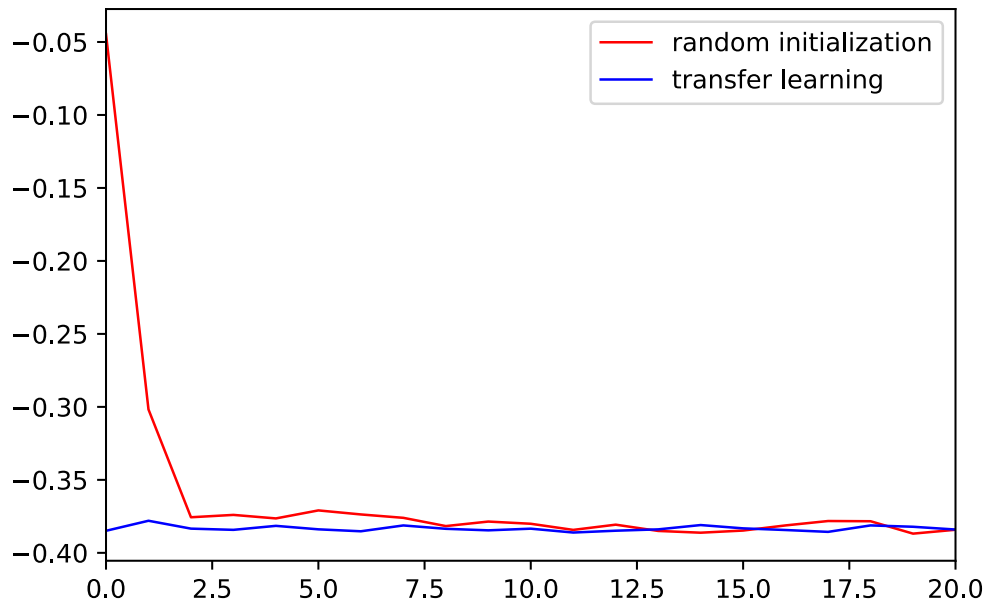
Figure 5.5 : (color online) Transfer learning, first train a network on system size 40 SU(2) spin-chain, then use the parameters as initialization for system size 100, SU(2). Comparing with random initialization, transfer learning will have much lower initial energy, and also be more stable.

Chapter 6

Summary

In this dissertation, we studied the spinor quantum gases system starting from Hamiltonian 1.1. By establishing a generalized Bose-Fermi mapping theory, we map the original symmetric (Bosons) or anti-symmetric (Fermions) system to a direct product system of spinless Fermions and spin chain, using the Spin-Charge Separated Representation (SCSR). By doing so, we can obtain a p-wave pseudopotential with interaction strength the inverse of the original s-wave contact interaction strength. So it is convenient to study the physics at large interaction. By doing perturbation theory on the mapped p-wave pseudopotential, we can obtain effective spin-chain models describing the spin degrees of freedom of the spinor quantum gases at large interaction. By extending the single-branch spin chain model to multi-branch spin-chain model, we can incorporate spatial degrees of freedom into the spin-chain models, which allows us to study the dynamics and collective excitations more precisely. We also studied the properties of the Strongly Coupling Ansatz Wavefunctions (SCAWs), including One-Body Density Matrix (OBDM) and momentum distribution. Through relating the OBDM of spinor gases to that of hardcore anyon gases, we obtained a very efficient method for calculating the OBDM and thus momentum distributions.

Chapter 7

Epilogue

Quantum many-body physics has been studied for a long time, but still many things to be understood. Many of them are related to the structure of quantum many-body wavefunctions. Some systems can be solved exactly using certain form of wavefunctions such as Bethe Ansatz, but many others can not. In this work, we studied the generalized Bose-Fermi mapping, studied Strong Coupling Ansatz Wavefunctions, related it with spin-charge separation, obtained effective spin-chain models which can help to better understand the wavefunction structures of spinor quantum gases at large interaction. Through studying the OBDM of spinor quantum gases, we found a relation of it with that of spinless hardcore anyon gases. On the other hand, variational wavefunctions could be an effective way to study the structure of the quantum many-body wavefunctions. For example, the success of mean field theories shows the system can be described by mean field wavefunctions. If there is some way that can produce variational wavefunctions automatically, it may help us to gain new understandings of the quantum many-body systems. This is just the spirit of Deep Learning Artificial Intelligence, in which deep neural networks are used for representing complex multi-dimension functions, and features are automatically extracted from one layer to the next layer. In this dissertation, we developed an VMC algorithm with Off-Policy optimization that allows training deep neural networks for representing quantum many-body wavefunctions. It helps exploring deep neural networks as new kinds of variational wavefunctions for quantum many-body systems.

Appendix A

Conventions for Permutation Operators

This appendix contains the convention about the permutation operators and its action on spatial and spin wave functions. A permutation operator P can be expressed as

$$
\begin{pmatrix}
1 & 2 & \cdots & N \\
P_1 & P_2 & \cdots & P_N
\end{pmatrix},
\tag{A.1}
$$

which means that the original particle index i, after the permutation, is changed into P_i. The action of the permutation operator P on a spatial wave function is defined by

$$
P\,\psi(x_1, x_2 \cdots x_N) = \psi(x_{P_1}, x_{P_2} \cdots x_{P_N})\,.
\tag{A.2}
$$

Similarly its action on a spin wave function is defined by

$$
P\,\chi(\sigma_1, \sigma_2 \cdots \sigma_N) = \chi(\sigma_{P_1}, \sigma_{P_2} \cdots \sigma_{P_N})\,,
\tag{A.3}
$$

where σ_i stands for the spin state for ith particle. The spin wave function χ is a rank-N SU(n) tensor with $n = 2s + 1$, if all the particles are spin-s particles.

A general spin state can be written as superposition of basis tensors (or spin Fock states). A basis tensor $|f_1 f_2 \cdots f_N\rangle$ means the i'th spin is in f_i state, and can be written as:

$$
|f_1 f_2 \cdots f_N\rangle = \sum_{\sigma_1, \ldots, \sigma_N} \delta_{\sigma_1 f_1} \delta_{\sigma_2 f_2} \cdots \delta_{\sigma_N f_N} |\sigma_1 \sigma_2 \cdots \sigma_N\rangle\,,
\tag{A.4}
$$

i.e. its wavefunction is a product of delta symbols. By definition, the permutation operator acting on a spin state by permuting the indices of its wavefunction, so acting on a spin basis yields

$$
\begin{aligned}
P \left| f_1 f_2 \cdots f_N \right\rangle &\leftrightarrow P \delta_{\sigma_1 f_1} \delta_{\sigma_2 f_2} \cdots \delta_{\sigma_N f_N} \\
&= \delta_{\sigma_{P_1} f_1} \delta_{\sigma_{P_2} f_2} \cdots \delta_{\sigma_{P_N} f_N} \\
&= \delta_{\sigma_1 f_{P_1^{-1}}} \delta_{\sigma_2 f_{P_2^{-1}}} \cdots \delta_{\sigma_N f_{P_N^{-1}}} \\
&\leftrightarrow \left| f_{P_1^{-1}} f_{P_2^{-1}} \cdots f_{P_N^{-1}} \right\rangle ,
\end{aligned}
\tag{A.5}
$$

i.e. the indices change on basis is inverse to that on wavefucntion.

We denote $\mathcal{E}_{i,j}$ as the exchange permutation operator, which simply exchanges indices $i \leftrightarrow j$:

$$
\mathcal{E}_{i,j} \left| f_1 \cdots f_i \cdots f_j \cdots f_N \right\rangle = \left| f_1 \cdots f_j \cdots f_i \cdots f_N \right\rangle .
\tag{A.6}
$$

We also denote the symbol $(m \cdots n)$ as a loop permutation operator, which, if $m \leq n$, permutes the indices of the wavefunction forwardly

$$
\begin{pmatrix}
1 & \cdots & m & m+1 & \cdots & n-1 & n & \cdots N \\
1 & \cdots & m+1 & m+2 & \cdots & n & m & \cdots N
\end{pmatrix},
\tag{A.7}
$$

and if $m \geq n$, permutes the indices of the wavefunction backwardly

$$
\begin{pmatrix}
1 & \cdots & n & n+1 & \cdots & m-1 & m & \cdots N \\
1 & \cdots & m & n & \cdots & m-2 & m-1 & \cdots N
\end{pmatrix}.
\tag{A.8}
$$

Note under a same permutation operator, the indices change of a spin basis is inverse to the indices change of its spin wavefunction (A.5). So the loop permutation operator's action on a spin basis is, for exmaple, $m \leq n$,

$$
\begin{aligned}
(m \cdots n) &\left| f_1 \cdots f_m f_{m+1} \cdots f_{n-1} f_n \cdots f_N \right\rangle \\
&= \left| f_1 \cdots f_n f_m \cdots f_{n-2} f_{n-1} \cdots f_N \right\rangle .
\end{aligned}
\tag{A.9}
$$

Appendix B

Multi-Branch Spin-Chain Model Recursion Relation from SO(2,1) Algebra

In this appendix, we discuss the SO(2, 1) algebra for spinless fermions in Harmonic trap. The spinless fermion wavefunctions can be constructed by generators of the SO(2, 1) algebra. And also the p-wave pseudopotential V_p (Eq. (2.30)) shows some symmetries with those generators. Combining those we derive a recursion relation for the spin-chain models in different branches (Section 3.3). We use the same convention as in [49]. The generators for the center-of-mass (COM) harmonic oscillator algebra and the SO(2,1) algebra can be made of generators from Schrödinger algebra, for which all the commutation relations are known [49]. The operators we use include

$$K = \int dx\, x n(x) \,, \quad P = \int dx\, j(x) \tag{B.1}$$

$$H = -\frac{1}{2} \int dx\, \psi^\dagger(x) \partial^2 \psi(x) \,, \quad C = \int dx\, \frac{x^2}{2} n(x) \,, \quad D = \int dx\, x j(x) \tag{B.2}$$

where $j(x) = -\frac{i}{2}(\psi^\dagger(x)\partial\psi(x) - \partial\psi^\dagger(x)\psi(x))$ is the current density. Here K represents the COM coordinate, P the total momentum, H the kinetic energy, C the trapping potential, and D the generator for scaling transformation. Again we have used the trap units with $\hbar = m = \omega = 1$. We can define COM ladder operators (without normalization) Q and $Q^\dagger$, and COM Hamiltonian H_0^c as

$$Q = \frac{K + iP}{\sqrt{2}} \,, \quad Q^\dagger = \frac{K - iP}{\sqrt{2}} \,, \quad H_0^c = \frac{\{Q, Q^\dagger\}}{2N} \,. \tag{B.3}$$

These three operators form a harmonic oscillator algebra for the COM motion.

The operators for the relative motion can be constructed as:

$$B = \frac{1}{2}[H - C + iD] - \frac{Q^2}{2N}, \tag{B.4}$$

$$B^\dagger = \frac{1}{2}[H - C + iD] - \frac{Q^{\dagger 2}}{2N}, \tag{B.5}$$

$$H_0^{\mathrm{i}} = H + C - H_0^{\mathrm{c}}, \tag{B.6}$$

which form a closed SO(2,1) algebra as they obey the following commutation relations:

$$[H_0^{\mathrm{i}}, B] = -2B, \quad [H_0^{\mathrm{i}}, B^\dagger] = 2B^\dagger, \quad [B, B^\dagger] = H_0^{\mathrm{i}}. \tag{B.7}$$

These three operators only act on the internal degree of freedom. As a result, the internal degrees of freedom can be classified into irreducible representations (IRs) of this SO(2,1) algebra. Each IR is a tower of states with energy level spacing 2. Together with the COM harmonic algebra, we can construct several lowest excited manifolds by acting $Q^\dagger$ and $B^\dagger$ on the ground state manifold. The five lowest manifolds are listed in Table B.1.

degeneracy	charge states				
5	$Q^{\dagger 4}\,\lvert 0\rangle$	$Q^{\dagger 2}B^\dagger\,\lvert 0\rangle$	$B^{\dagger 2}\,\lvert 0\rangle$	$Q^\dagger\,\lvert \alpha\rangle$	$\lvert \beta\rangle$
3	$Q^{\dagger 3}\,\lvert 0\rangle$	$Q^\dagger B^\dagger\,\lvert 0\rangle$	$\lvert \alpha\rangle$		
2	$Q^{\dagger 2}\,\lvert 0\rangle$	$B^\dagger\,\lvert 0\rangle$			
1	$Q^\dagger\,\lvert 0\rangle$				
1	$\lvert 0\rangle$				

Table B.1 : Several lowest manifolds constructed by acting ladder operators $Q^\dagger$ and $B^\dagger$ on the ground state. $\lvert 0\rangle$ stands for the ground state. $\lvert \alpha\rangle$ and $\lvert \beta\rangle$ stand for the beginning states of other SO(2,1) towers.

We know that the fourth manifold is three-fold degenerate, but from $Q^\dagger$ and $B^\dagger$ we can only construct two states. So we need to introduce a new state denoted as

$|\alpha\rangle$ having the property $Q|\alpha\rangle = B|\alpha\rangle = 0$. This is where another SO(2,1) IR tower begins. Similarly we need to introduce $|\beta\rangle$ for the fifth excited manifold. The basis of each manifold can be constructed in this way by acting $Q^\dagger$ and $B^\dagger$ on lower states and introducing beginning states for new towers.

When we want to write down the first order perturbation of V_p in the nth manifold, we may need to calculate matrix elements whose most general form is

$$\frac{\langle\alpha_0, \chi| Q^p B^m V_p B^{\dagger n} Q^{\dagger q} |\beta_0, \chi'\rangle}{\sqrt{\langle\alpha_0, \chi| Q^p B^m B^{\dagger m} Q^{\dagger p} |\alpha_0, \chi\rangle \langle\beta_0, \chi'| Q^q B^n B^{\dagger n} Q^{\dagger q} |\beta_0, \chi'\rangle}} \tag{B.8}$$

where χ and χ' stands for two spin states. α_0 and β_0 stands for two arbitrary beginning states of two SO(2,1) IR towers and also with no COM excitation. They are excited by $B^\dagger$ and $Q^\dagger$ to the energy of the manifold we are considering. Since we are doing first order perturbation, the relation of $E_{\alpha_0} + p + 2m = E_{\beta_0} + q + 2n$ must be hold.

Equation (B.8) can be simplified as follows. Since Q commute with V_p and B, Eq. (B.8) is only nonzero when $p = q$ and Q operators in the numerator and denominator are canceled. So we only need to consider

$$H_{\text{sc},\alpha_0\beta_0,mn} = \frac{\langle\alpha_0, \chi| B^m V_p B^{\dagger n} |\beta_0, \chi'\rangle}{\sqrt{\langle\alpha_0, \chi| B^m B^{\dagger m} |\alpha_0, \chi\rangle \langle\beta_0, \chi'| B^n B^{\dagger n} |\beta_0, \chi'\rangle}} \tag{B.9}$$

where $E_{\alpha_0} + 2m = E_{\beta_0} + 2n$ must be hold. It is possible that $\alpha \neq \beta$ and $H_{\text{sc},\alpha\beta,mn}$ nonzero, under this case V_p will couple different charge states. In the first four manifolds listed in Table B.1, we do not need to consider this as it can be straightforwardly shown that matrix elements of V_p between two different states within the same manifold all vanish. However, this is no longer true for the fifth and higher manifolds since $\langle\beta| V_p B^{\dagger 2} |0\rangle$ in general is nonzero. If we are only concerned with the first 4 manifolds, we can further simplify Eq. (B.9) to

$$H_{\text{sc},m} = \frac{\langle 0, \chi| B^m V_p B^{\dagger m} |0, \chi'\rangle}{\langle 0, \chi| B^m B^{\dagger m} |0, \chi'\rangle} \tag{B.10}$$

where 0 stands for the charge ground state. Equation (B.10) can be written into a recursion relation [50] by using the known commutation relations of operators in the Schrödinger algebra [49]. Since all we use to derive this recursion relation is using commutation relations among the operators defined in Eqs. (B.1) and (B.2), as well as V_p, and their action on the charge degree of freedom, in the following we suppress the spin states χ and χ'. By switching B and V_p twice and denoting $\langle ... \rangle = \langle 0|...|0\rangle$, we can arrive at

$$
\begin{aligned}
H_{\mathrm{sc},m} &= \frac{\left\langle B^m H_p B^{\dagger m}\right\rangle}{\left\langle B^m B^{\dagger m}\right\rangle} \\
&= \frac{\left\langle B^{m-1}(H_p B + [B, H_p])B^{\dagger m}\right\rangle}{\left\langle B^m B^{\dagger m}\right\rangle} \\
&= H_{\mathrm{sc},m-1} + \frac{\left\langle B^{m-1}[B, H_p]B^{\dagger m}\right\rangle}{\left\langle B^m B^{\dagger m}\right\rangle} \\
&= H_{\mathrm{sc},m-1} + \frac{\left\langle B^{m-1}(B^{\dagger}[B, H_p] + [[B, H_p], B^{\dagger}])B^{\dagger m-1}\right\rangle}{\left\langle B^m B^{\dagger m}\right\rangle} \\
&= H_{\mathrm{sc},m-1} + \frac{\left\langle B^{m-1} B^{\dagger m-1}\right\rangle^2}{\left\langle B^{m-2} B^{\dagger m-2}\right\rangle \left\langle B^m B^{\dagger m}\right\rangle}[H_{\mathrm{sc},m-1} - H_{\mathrm{sc},m-2}] \\
&\quad + \frac{\left\langle B^{m-1}[[B, H_p], B^{\dagger}]B^{\dagger m-1}\right\rangle}{\left\langle B^m B^{\dagger m}\right\rangle}
\end{aligned}
\tag{B.11}
$$

Let us next consider the last term. Since Q commutes with V_p and B, we can ignore all the Q parts in B [see Eq. (B.4)]. Consider the commutator $[B, H_p]$. First let us prove $[C, V_p] = 0$. Since V_p is in first quantized form, we also use the first quantized form of C, with which we have

$$
[C, H_p] = \left[\sum_{i=1}^N \frac{1}{2}x_i^2, -\frac{4N!}{g}\sum_{i=1}^{N-1}\overleftarrow{\partial}_i \delta(x_i - x_{i+1})\theta^1 \overrightarrow{\partial}_i \otimes \hat{P}_i^{s,a}\right]
\tag{B.12}
$$

In this expression, note that each term in the spatial part of V_p only acts on relative coordinate $x_{ii+1} = x_i - x_{i+1}$, and C can also be separated into one part containing relative coordinates x_{ii+1} and another part containing the COM coordinate $\sum x_i/N$.

The nonzero contribution can only come from the commutator

$$\left[x^2, \overleftarrow{\partial}\,\delta(x)\theta(x)\,\overrightarrow{\partial}\right] = 2x\delta(x)\theta(x)\,\overrightarrow{\partial} - \overleftarrow{\partial}\,\delta(x)\theta(x)2x\,, \qquad \text{(B.13)}$$

which is 0 since $x\delta(x) = 0$. Here we have also ignored the regularization point splitting in ∂_-, since in the derivation of the recursion formula, we only need to consider continuous wavefunctions. Therefore we have proved that

$$[C, H_p] = 0\,. \qquad \text{(B.14)}$$

Next we consider V_p's scaling dimension. Since V_p is made of two spatial derivatives and a delta function (also a θ function whose scaling dimension is 0), it has scaling dimension 3, which means

$$[D, V_p] = i\Delta_{V_p}V_p, \quad \Delta_{V_p} = 3\,. \qquad \text{(B.15)}$$

Using Eqs. (B.14) and (B.15), the commutator $[B, H_p]$ can be written as

$$[B, H_p] = \frac{1}{2}\left[H, H_p\right] + \frac{1}{2}\Delta_{H_p}H_p\,. \qquad \text{(B.16)}$$

Now consider its commutation relation with $B^\dagger$

$$\begin{aligned}
&\left[\left[B, H_p\right], B^\dagger\right] \\
=&\frac{1}{4}\left[\left[H, H_p\right] + \Delta_{H_p}H_p, H - C + iD\right] \\
=&\frac{1}{4}\left[\left[H, H_p\right] + \Delta_{H_p}H_p, H_{\text{osc}}\right] - \frac{1}{2}\left[\left[H, H_p\right], C\right] + \frac{1}{4}\left[\left[H, H_p\right], iD\right] + \frac{1}{4}\Delta_{H_p}^2 H_p\,.
\end{aligned} \qquad \text{(B.17)}$$

In the second step we have used $[C, V_p] = 0$ and $[D, V_p] = i\Delta_{V_p}V_p$. And we introduce $H_{\text{osc}} = H + C$ which is the harmonic oscillator Hamiltonian. Using Jacobi identity followed by the commutation relations $[C, H] = iD$, $[D, H] = 2iH$, $[C, V_p] = 0$ and

$[D, V_p] = i\Delta_{V_p} V_p$, the second and third terms of Eq. (B.17) can be written as

$$[[H, H_p], C] = -[[H_p, C], H] - [[C, H], H_p]$$

$$= -[iD, H_p] = \Delta_{V_p} V_p,$$

$$[[H, H_p], iD] = -[[H_p, iD], H] - [[iD, H], H_p]$$ (B.18)

$$= -[\Delta_{H_p} H_p, H] + [2H, H_p]$$

$$= -[\Delta_{H_p} H_p, H_{\text{osc}}] + [2H_{\text{osc}}, H_p].$$

Since we are going to calculate $\langle 0| B^{m-1}[[B, H_p], B^\dagger] B^{\dagger m-1} |0\rangle$ and $B^{\dagger m-1} |0\rangle$ is an eigenstate of H_{osc}, all the terms which are commutators with H_{osc} vainsh. Only the second and forth term in Eq. (B.17) remain. Finally the last term in Eq. (B.11) can be written as

$$\frac{\langle B^{m-1}[[B, H_p], B^\dagger] B^{\dagger m-1}\rangle}{\langle B^m B^{\dagger m}\rangle} = \frac{1}{4}\Delta_{H_p}(\Delta_{H_p} - 2)\frac{\langle B^{m-1} B^{\dagger m-1}\rangle}{\langle B^m B^{\dagger m}\rangle} H_{\text{sc},m-1}$$ (B.19)

The normalization can also be easily evaluated by using $[B, B^\dagger] = H_0^{\text{i}}$, from which we have

$$S_m = \frac{\langle B^{m+1} B^{\dagger m+1}\rangle}{\langle B^m B^{\dagger m}\rangle} = (m+1)(m + E_0^{\text{i}}).$$ (B.20)

where $E_0^{\text{i}} = N^2/2 - 1/2$ is the ground state internal energy. Putting Eqs. (B.11), (B.19), and (B.20) together, a recursion relation is obtained

$$H_{\text{sc},m} - H_{\text{sc},m-1} = \frac{(m-1)(m-2+E_0^{\text{i}})}{m(m-1+E_0^{\text{i}})}[H_{\text{sc},m-1} - H_{\text{sc},m-2}]$$

$$+ \frac{1}{4}\frac{\Delta_{H_p}(\Delta_{H_p} - 2)}{m(m-1+E_0^{\text{i}})} H_{\text{sc},m-1}.$$ (B.21)

The spin chain Hamiltonian for the first excited manifold and for the dipole state of the second excited manifold, which correspond to $m = 0$, are the same as ground state spin chain Hamiltonian (when a constant shift is neglected):

$$H_{\text{sc}}^{(1)} = H_{\text{sc}}^{(Q)} = H_{\text{sc},0} = H_{\text{sc}}^{(0)}.$$ (B.22)

The spin chain Hamiltonian for breathing state of the second excited manifold, which corresponds to $m = 1$, is proportional to the ground state spin chain Hamiltonian:

$$H_{\text{sc}}^{(B)} = H_{\text{sc},1} = \left[1 + \frac{3}{2(N^2 - 1)}\right] H_{\text{sc},0} = \left[1 + \frac{3}{2(N^2 - 1)}\right] H_{\text{sc}}^{(0)}. \tag{B.23}$$

We stress here that we cannot obtain a similar recursion formula like Eq. (B.21) for the most general matrix elements $H_{\text{sc},\alpha_0\beta_0,mn}$ (Eq.(B.9)) for arbitrary α_0 and β_0 case. This is because V_p may couple different charge states within the same manifold and the eigenstates of the perturbative spin chain model will no longer be a direct product state of spatial and spin wave function. To study the entanglement properties of spin and charge is an interesting problem.

Appendix C

Methods for Calculating Coupling Coefficients

The expression for coupling coefficients in effective spin-chain models of Eq. (3.2) and Eq. (3.12) involves multi-dimensional integrals usually without closed form solutions. In this Appendix, we provide methods for calculating those coupling coefficients across various level of approximations.

C.1   Harmonic Conjecture

For Particles in a harmonic trap, there is a Harmonic Conjecture [25] for approximating the coupling coefficients $C_i^{(0)}$ for the effective spin-chain model in ground state branch Eq. (3.2).

$$C_i^{(0)} = K \, \frac{-(i - N/2)^2 + N^2/4}{N(N-1)/2} \, , \tag{C.1}$$

where K is the Tan contact for the AFM state corresponding to $(N_\uparrow, N_\downarrow) = (N-1, 1)$. In Fig. C.1, we plot the exactly calculated $C_i^{(0)}$ using Monte Carlo integral for $N = 8$ and 13 (symbols), in comparison with the above expression (lines), and find good agreement. Hence, at least for harmonic trapped systems, once we know the Tan contact, all the $C_i^{(0)}$ coefficients can be obtained approximately using Eq. (C.1). We can see that the Harmonic Conjecture can efficiently capture the values of $C_i^{(0)}$ to a somewhat good precision. In Section C.3, we provide a more precise approximation for $C_i^{(0)}$ using Local Density Approximation.
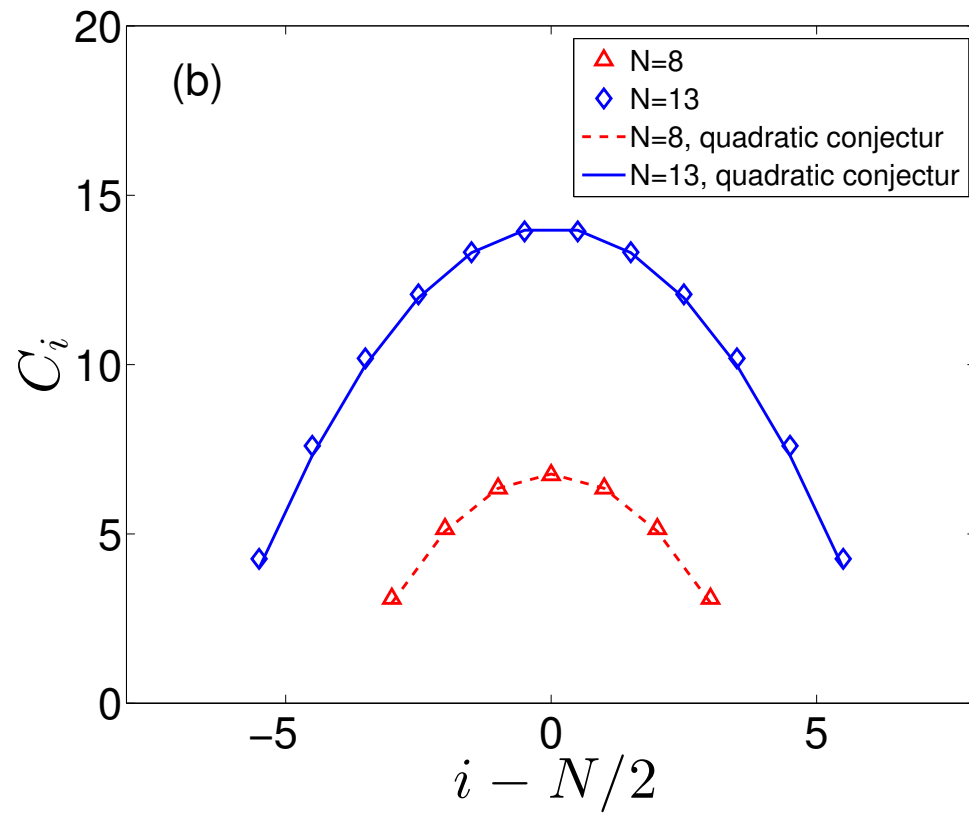
Figure C.1 : (color online) Dimensionless coefficients $C_i^{(0)}$ for $N = 8$ and 13, calculated using the Monte Carlo integral method (Veges Algorithm [1]). The solid lines are obtained using the Harmonic Conjecture approximate expression (C.1).

C.2 Monte Carlo Integral

The form of Eq. (3.2) and Eq. (3.12) involves multi-dimensional integral, so Monte Carlo integral is naturally a good numerical method to calculate those coefficients. Examples of $N = 8$ and 13 are shown in Fig. C.1. However, Monte Carlo method intrinsically has high variance for larger number of particles. Coordinate transformation may help to some extent. Another issue is for coupling coefficients in higher branch spin-chain models Eq. (3.12), the integrand involves excited state wavefunctions which are fast oscillating. Monte Carlo method will have low performance for calculating those fast oscillating integrals.

C.3 Local Density Approximation

C.3.1 General Trapping Potential

When the average particle spacing is much smaller than the characteristic length of the variation of the trapping potential, locally the particles feel they are in a homogeneous system. This usually happens when trapping potential is slow varying, or the density of particles is high. In this case, Local Density Approximation(LDA) may be used to obtain a good approximation for the coupling coefficients $C_i^{(0)}$ in ground state branch spin-chain models. For a infinite homogeneous system, $C_i^{(0)} = C^{(0)}$ is a single constant and has the following form

$$C^{(0)} = \frac{\pi^2}{3} n_{\mathrm{TG}}^3 \,, \tag{C.2}$$

where n_{TG} is the density of the Tonks-Girardeau gas, which is also the density of spinless fermions with same particle number as the total particle number of the spinor gas. From Eq. (C.2), we can see the coupling coefficients is proportional to the density cube. For a inhomogeneous system that LDA is applicable, the density is a function

of spatial coordinate x. We assume the following expression for the local coupling coefficients:

$$C_i^{(0)} = \frac{\pi^2}{3} n_{\text{TG}}^3(y_i), \quad i = 1, 2, ..., N - 1, \tag{C.3}$$

The expression Eq. (C.3) is inspired by [24, 31, 104, 105], but a key point is that the coupling coefficients at index i, which is for the spin exchange for particle i and $i+1$, is evaluated using the density at position y_i. The physical meaning of y_i is the average location for the 'boundary' between particle i and $i+1$. With this meaning, combining with the Tonks-Girardeau density profile $n_{\text{TG}}(x)$, the y_i are naturally defined as

$$\int_{-\infty}^{y_i} dx \, n_{\text{TG}}(x) = i, \tag{C.4}$$

which is the average boundary of the ith and $(i + 1)$th particle. From Eq. (C.4) we can solve y_i, and after substitute y_i into Eq. (C.3), we can obtain the local coupling coefficients $C_i^{(0)}$.

C.3.2 Harmonic Trapping Potential

For harmonic trapped system, $n_{\text{TG}}(x) = \frac{1}{\pi}\sqrt{2N - x^2}$ is the Tonks-Girardeau density profile which is the same as the density profile of a spinless Fermi gas. $n_{\text{TG}}(x)$ is nonzero only within range $[-\sqrt{2N}, \sqrt{2N}]$. Eq. (C.4) can be exactly integrated. Equations. (C.3) and (C.4) are equivalent to

$$C_i^{(0)} = \frac{1}{3\pi} (2N)^{3/2} \sin^3\left(\frac{\alpha_i}{2}\right), \tag{C.5}$$

where α_i is the solution of equation

$$\alpha_i - 2\pi \frac{i}{N} = \sin(\alpha_i). \tag{C.6}$$

The comparison with the exact $C_i^{(0)}$ calculated by a similar method as calculating $\rho^{(i)}(z)$ in [2] is shown in Fig. C.2, from which we see that even for very few particles the LDA results agree with the exact values very well.
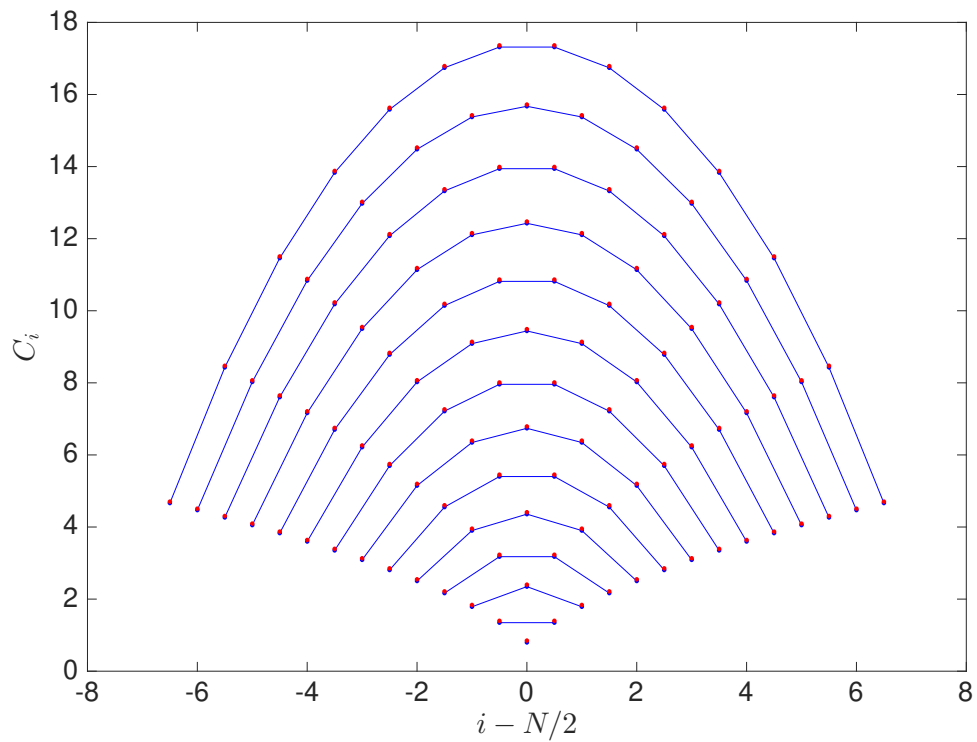
Figure C.2 : (color online) The red dots represent results from the LDA approximation for $C_i^{(0)}$ using Eqs. (C.5) and (C.6). The blue solid lines are exact integral of $C_i^{(0)}$ by a method similar to calculating $\rho^{(i)}(z)$ in [2]. The comparison are for particle numbers run from 2 (bottom) to 15 (top).

C.3.3 Thermodynamic Limit

For repulsively interacting bosons the ground state energy is

$$E_g^{\text{boson}} = -\frac{2}{g} \sum_{i=1}^{N-1} C_i^{(0)} . \tag{C.7}$$

Taking $N \to \infty$, using the LDA result Eq. (C.5) for $C_i^{(0)}$, and converting the sum into an integral:

$$\begin{aligned}
E_g^{\text{boson}} &\approx -\frac{1}{g} \frac{(2N)^{5/2}}{3\pi} \int_0^1 d\beta \sin^3\left[\frac{\alpha(\beta)}{2}\right] \\
&= -\frac{1}{g} \frac{128\sqrt{2}}{45\pi^2} N^{5/2} \approx -\frac{1}{g} 0.408 N^{5/2} ,
\end{aligned} \tag{C.8}$$

where $\beta = i/N \in (0,1)$. This result is consistent with the previous result obtained for spinless bosons near the TG limit [39, 51, 52], which gives another indication that our LDA approximation for $C_i^{(0)}$ is excellent.

C.4 Using One-Body Density Matrix

We can also take advantage the result of Section 4.1 by using a relation of the coupling coefficients and the expansion of $\rho_{m,m\pm1}(x,y)$ at small distance $x \approx y$. Finally we would like to point out there are also other methods [90] for calculating the local exchange coefficients C_i with various computational complexities.

Appendix D

Green's Function Methods for Few Spinor Particles.

Green's function method can be used for solving the Hamiltonian Eq. (1.1) up to a few particles [26]. Consider a Schrödinger equation

$$(\hat{H}_0 + \hat{V}) |\Psi\rangle = E |\Psi\rangle , \tag{D.1}$$

where $\hat{H}_0$ and $\hat{V}$ can be regarded as unperturbated Hamiltonian and perturbation Hamiltonian, respectively. The eigenstates and eigenenergies of $\hat{H}_0$ can be easily calculated. If we can obtain the form of

$$\frac{1}{E - \hat{H}_0} , \tag{D.2}$$

then we can write down the following equation for the eigenstate $|\Psi\rangle$

$$|\Psi\rangle = \frac{1}{E - \hat{H}_0} \hat{V} |\Psi\rangle . \tag{D.3}$$

Equation D.3 is actually the Lippmann-Schwinger equation, which is an integral equation. Sometimes, if $\hat{V}$ has a special form, Eq. (D.3) can be simplified. Take a single particle with a delta function barier $V(x) = g\delta(x)$ as an example, if we write Eq. (D.3) into spatial coordinate form

$$\Psi(x') = \int_{-\infty}^{\infty} dx \, \langle x'| \frac{1}{E - \hat{H}_0} |x\rangle \, V(x)\Psi(x)$$
$$= G(E; x', 0)g\Psi(0), \tag{D.4}$$

where $G(E; x', 0) = \langle x' | \frac{1}{E - \hat{H}_0} | x \rangle$ is the Green's function. Note that in Eq. (D.4), the special form of delta function barrier $V(x) = g\delta(x)$ reduce the integral by one dimension. In later sections, we will see if we use Green's function method to solve few particle system governed by Hamiltonian Eq. (1.1), the delta function contact interaction will always reduce the integral in the Lippmann-Schwinger equation by one dimension.

D.1 Green's Function Method for Two Particles

The Hamiltonian of two particles in a one dimensional harmonic trap with a spin dependent magnetic gradient is

$$H = -\frac{1}{2}\frac{\partial^2}{\partial x_1^2} - \frac{1}{2}\frac{\partial^2}{\partial x_2^2} + \frac{1}{2}x_1^2 + \frac{1}{2}x_2^2 + g\delta(x_1 - x_2) - Gx_1\sigma_1^z - Gx_2\sigma_2^z. \qquad (D.5)$$

In the absence of the magnetic gradient (i.e., $G = 0$), there exists an exact solution to the problem [33]. Here we generalize this solution in the presence of the magnetic gradient. To this end, we make a transformation of operators by making spatial and spin coordinates operators into Jacobi coordinates:

$$X_1 = \frac{x_1 - x_2}{\sqrt{2}}, \ X_2 = \frac{x_1 + x_2}{\sqrt{2}}, \ S_1 = \frac{\sigma_1^z - \sigma_2^z}{\sqrt{2}}, \ S_2 = \frac{\sigma_1^z + \sigma_2^z}{\sqrt{2}}. \qquad (D.6)$$

The transformation rules of other operators such as $\partial/\partial x$ can be obtained from them. The Hamiltonian can be separated into the center-of-mass motion part and the relative motion part:

$$H = -\frac{1}{2}\frac{\partial^2}{\partial X_2^2} + \frac{1}{2}X_2^2 - GS_2X_2 - \frac{1}{2}\frac{\partial^2}{\partial X_1^2} + \frac{1}{2}X_1^2 - GS_1X_1 + \frac{g}{\sqrt{2}}\delta(X_1). \qquad (D.7)$$

For center-of-mass motion, it is a simple harmonic oscillator with center shifted by GS_2. For relative motion, it is a simple harmonic oscillator with center shifted by

GS_1 plus a δ-function potential at the origin. We can first let particle 1 to be spin up and particle 2 to be spin down, then anti-symmetrize the wave function in the end. In this case, $S_2 = 0$ and $S_1 = \sqrt{2}$ are fixed. The eigen wave functions for the center-of-mass motion are still simple harmonic oscillator eigen-functions. What matters is the relative motion part. After a coordinate shift $X_1 - GS_1 \rightarrow X_1$, The relative motion Hamiltonian can be written as

$$H_{\text{rel}} = -\frac{1}{2}\frac{\partial^2}{\partial X_1^2} + \frac{1}{2}X_1^2 + \frac{g}{\sqrt{2}}\,\delta(X_1 + GS_1)\,, \tag{D.8}$$

which includes a simple harmonic oscillator part and a δ-function source term. For this relative Hamiltonian, use the one-body Green's function

$$G(E; X_1, X_1') = \sum_{i=0}^{\infty}\frac{1}{E - E_i}\phi_i(X_1)\phi_i^*(X_1')\,, \tag{D.9}$$

where $E_i = i+1/2$ and ϕ_i are the single particle harmonic oscillator eigen-energies and eigen-wave functions, respectively. The corresponding Lippmann-Schwinger equation for the relative wavefunction is given by

$$\begin{aligned}
\varphi(X_1) &= \int dX_1 G(E; X_1, X_1')\frac{g}{\sqrt{2}}\,\delta(X_1 + GS_1)\varphi(X_1') \\
&= \frac{g}{\sqrt{2}}\,G(E; X_1, -GS_1)\varphi(-GS_1)\,.
\end{aligned} \tag{D.10}$$

We just got the expression for the relative wave function, where $\varphi(-GS_1)$ is a constant can be determined by normalization of $\varphi(X_1)$. And the relative energy must satisfy

$$G(E; -GS_1, -GS_1) = \frac{\sqrt{2}}{g}\,. \tag{D.11}$$

Note that, when $G = 0$, the Green's function method fails at $E = E_i$, and for $E \neq E_i$ the left hand side of Eq. (D.11) has an analytical form [33]. Actually the solution of fully symmetric spin wave function (necessarily assoticated with fully anti-symmetric spatial wave function) which has $E = E_i$ should be complemented to the Green's

function solution. However, for $G \neq 0$, there is no such pathological behavior for the Green's function method. Also to be noted is that for one E, there could be only one $1/g$ for which Eq. (D.11) is satisfied. This means, for relative motion, there could be only one bound state. However, this is no longer true for three particles, because the Lippmann-Schwinger equation for three particles is an integral equation and there can exist infinitely many bound states for three particles' relative motion.

Finally, substitute back $X_1 \to X_1 - GS_1$, after anti-symmetrization, the total wavefunction for two fermions is given by

$$\frac{1}{\sqrt{2}} \Psi_{cm}(X_2) \left[\varphi(X_1 - G\sqrt{2}) \left|\uparrow\downarrow\right\rangle - \varphi(-X_1 - G\sqrt{2}) \left|\downarrow\uparrow\right\rangle \right] . \tag{D.12}$$

The center-of-mass separation between the two spins, $\Delta = \langle x_1 \sigma_1^z + x_2 \sigma_2^z \rangle / 2$, can be calculated as

$$\Delta = \frac{1}{\sqrt{2}} \int dX_1 X_1 \left| \varphi(X_1) \right|^2 + G , \tag{D.13}$$

where $\varphi(X_1)$ is decided by Eq. (D.10), which dependents on G and E, where E is dependent on G and $1/g$ by Eq. (D.11). The first term in Eq. (D.13) is from interplay between the interaction and the magnetic gradient, while the second term in Eq. (D.13) is due to the harmonic trap shift induced by the magnetic gradient.

D.2 Green's Function Method for Three Particles

For three particles, consider spin-independent interaction.

$$H = \sum_{i=1}^{3} \left(-\frac{1}{2} \frac{\partial^2}{\partial x_i^2} + \frac{1}{2} x_i^2 - G x_i \sigma_i^z \right) + g \sum_{i<j} \delta(x_i - x_j) . \tag{D.14}$$

After defining the Jacobi coordinates

$$\begin{aligned}
X_1 &= \frac{x_2 - x_3}{\sqrt{2}}, \ X_2 = \frac{x_2 + x_3 - 2x_1}{\sqrt{6}}, \ X_3 = \frac{x_1 + x_2 + x_3}{\sqrt{3}}, \\
S_1^z &= \frac{\sigma_2^z - \sigma_3^z}{\sqrt{2}}, \ S_2^z = \frac{\sigma_2^z + \sigma_3^z - 2\sigma_1^z}{\sqrt{6}}, \ S_3^z = \frac{\sigma_1^z + \sigma_2^z + \sigma_3^z}{\sqrt{3}},
\end{aligned} \tag{D.15}$$

to separating the center of mass motion and relative motion, the Hamiltonian(D.14) can be written as

$$
\begin{aligned}
H = &-\frac{1}{2}\sum_{i=1}^{3}\left[\frac{\partial^2}{\partial X_i^2} - (X_i - GS_i^z)^2\right] + g\sqrt{\frac{2}{3}}\delta(\frac{1}{\sqrt{3}}X_1 + X_2) \\
&+ g\sqrt{\frac{2}{3}}\delta(\frac{1}{\sqrt{3}}X_1 - X_2) + g\sqrt{\frac{1}{2}}\delta(X_1) - \frac{3}{2}G^2 \, .
\end{aligned}
$$
(D.16)

first assume $\sigma_1^z = 1$, $\sigma_2^z = -1$, and $\sigma_3^z = -1$, then symmetrize the wavefunction at the end. This means $S_1^z = 0$, $S_2^z = -\frac{4}{\sqrt{6}}$, and $S_3^z = -\frac{1}{\sqrt{3}}$. We can further make a shift of coordinates such that every particle feels the same trapping potential as for the two particle case. And note if the eigenfunction has symmetry $\varphi(X_1, X_2) = -\varphi(-X_1, X_2)$, we can drop the $\delta(X_1)$ term. The relative Hamiltonian now becomes

$$
\begin{aligned}
H_{rel} = &-\frac{1}{2}\left[\frac{\partial^2}{\partial X_1^2} - X_1^2\right] - \frac{1}{2}\left[\frac{\partial^2}{\partial X_2^2} - X_2^2\right] \\
&+ g\sqrt{2}\delta(\sqrt{3}X_2 - 2\sqrt{2}G + X_1) + g\sqrt{2}\delta(\sqrt{3}X_2 - 2\sqrt{2}G - X_1)
\end{aligned}
$$
(D.17)

We can use Green's function method to solve this two degree of freedom Hamiltonian. The Lippmann-Schwinger equation after integrating out the delta function interactions now can be written into a linear integral equation.

$$
\varphi(\sqrt{3}X_2 - 2\sqrt{2}G, X_2) = g\sqrt{2}\int dX_2' K(X_2, X_2')\varphi(\sqrt{3}X_2' - 2\sqrt{2}G, X_2') \,,
$$
(D.18)

where the kernel is

$$
\begin{aligned}
K(X_2, X_2') = &G(\sqrt{3}X_2 - 2\sqrt{2}G, X_2; \sqrt{3}X_2' - 2\sqrt{2}G, X_2') \\
&- G(\sqrt{3}X_2 - 2\sqrt{2}G, X_2; -\sqrt{3}X_2' + 2\sqrt{2}G, X_2') \,,
\end{aligned}
$$
(D.19)

where the two body Green's function is defined as

$$
G(X_1, X_2; X_1', X_2') = \sum_{i,j}\frac{1}{E - E_{ij}}\phi_i(X_1)\phi_i(X_1')\phi_j(X_2)\phi_j(X_2') \,,
$$
(D.20)

which can be calculated efficiently with great precision for harmonic trapped system.

Appendix E

One-Body Density Matrix of Strong Coupling Ansatz Wavefunction

In this appendix, we consider the One-Body Density Matrix(OBDM) for Strong Coupling Ansatz Wavefunctions Eq. (4.1). A SCAW is one-to-one mapped to a direct product of spatial and spin wavefunctions, correspondingly, we want to obtain some spin-charge separated form for its OBDM. Given a many-body wave function Ψ, the one-body density matrix is defined as:

$$
\rho_{\sigma'\sigma}(x', x) = \sum_{\sigma_2\cdots\sigma_N} \int dx_2\cdots dx_N \, \Psi^*(x', x_2\cdots x_N, \sigma', \sigma_2\cdots\sigma_N)
$$
$$
\cdot\Psi(x, x_2\ldots x_N, \sigma, \sigma_2\cdots\sigma_N). \tag{E.1}
$$

Consider Fermionic system first, the wave function takes the form of Eq. (4.1),

$$
\Psi = \sum_P (-1)^P P\left[\varphi\theta^1 \otimes \chi\right] = \varphi\sum_P \left[\theta^P \otimes \chi\right], \tag{E.2}
$$

where $\theta^P = P\theta$(For permutation operator acting on spatial and spin wavefunctions, see Appendix A) is the sector function (generalized step function) for the sector labled by permutation operator P, the one-body density matrix can be written as

$$
\rho_{\sigma'\sigma}(x', x) = \sum_{\sigma_2\cdots\sigma_N} \int dx_2\cdots dx_N \varphi'^*\varphi \sum_{P'P} \theta'^{P'}\theta^P \otimes (P'\chi'^*)(P\chi), \tag{E.3}
$$

where we define

$$
\varphi = \varphi(x, x_2\cdots x_N), \ \ \varphi'^* = \varphi^*(x', x_2\cdots x_N)
$$
$$
\theta^P = P\theta(x, x_2\cdots x_N), \ \theta'^{P'} = P'\theta(x', x_2\cdots x_N) \tag{E.4}
$$
$$
\chi = \chi(\sigma, \sigma_2\cdots\sigma_N), \ \ \ \chi'^* = \chi^*(\sigma', \sigma_2\cdots\sigma_N)
$$

for short. A permutation P can be written as $P_{2\dots N} \cdot (1\cdots m)$, where $(1\cdots m)$ is the loop permutation operator between indices 1 and m defined in Appendix A, and $P_{2\dots N}$ is a permutation operator acting on indices $2, 3 \cdots N$. This means first move particle 1 to position m by a loop permutation, and then permute the remaining $N-1$ particles. Similarly, P' can be written as $P' = P'_{2\dots N} \cdot (1\cdots n)$. The summation over P' and P can then be written into another form:

$$
\begin{aligned}
\rho_{\sigma'\sigma}(x',x) =& \sum_{\sigma_2\cdots\sigma_N} \int dx_2 \cdots dx_N \varphi'^* \varphi \sum_{m,n} \sum_{\substack{P'_{2\dots N}, \\ P_{2\dots N}}} \theta'^{P'_{2\dots N}\cdot(1\cdots m)} \theta^{P_{2\dots N}\cdot(1\cdots n)} \\
& \otimes [P'_{2\dots N} \cdot (1\cdots m)\chi'^*] [P_{2\dots N} \cdot (1\cdots n)\chi] \\
=& \sum_{\sigma_2\cdots\sigma_N} \int dx_2 \cdots dx_N \varphi'^* \varphi \sum_{mn} \sum_{P_{2\dots N}} \theta'^{P_{2\dots N}\cdot(1\cdots m)} \theta^{P_{2\dots N}\cdot(1\cdots n)} \\
& \otimes [P_{2\dots N} \cdot (1\cdots m)\chi'^*] [P_{2\dots N} \cdot (1\cdots n)\chi] \\
=& \sum_{mn} (N-1)! \int dx_2 \cdots dx_N \varphi'^* \varphi \theta'^{(1\cdots m)} \theta^{(1\cdots n)} \\
& \otimes \sum_{\sigma_2\cdots\sigma_N} [(1\cdots m)\chi'^*] [(1\cdots n)\chi] \ .
\end{aligned}
\tag{E.5}
$$

The second equal sign follows the fact that if $P'_{2\dots N} \neq P_{2\dots N}$,

$$
\theta'^{P'_{2\dots N}}(x_2\cdots x_m, x'\cdots x_N)\theta^{P_{2\dots N}}(x_2\cdots x_n, x\cdots x_N) = 0 \,,
\tag{E.6}
$$

and the third equal sign uses the fact that $\sum_{\sigma_2\cdots\sigma_N}\int dx_2\cdots dx_N$ is invariant under $P_{2\dots N}$. So the one-body density matrix can be separated into a spatial part and a spin part

$$
\rho_{\sigma'\sigma}(x',x) = \sum_{m,n} \rho_{m,n}(x',x) S_{m,n}(\sigma',\sigma) \,,
\tag{E.7}
$$

where the spatial part

$$
\begin{aligned}
\rho_{m,n}(x',x) &= (-1)^{(m-n)}(N-1)! \int dx_2 \cdots dx_N \ \varphi'^* \varphi \ \theta'^{(1\cdots m)} \theta^{(1\cdots n)} \\
&= (-1)^{(m-n)}(N-1)! \int_{\Gamma_{mn}} dx_2 \cdots dx_N \ \varphi'^* \varphi \,,
\end{aligned}
\tag{E.8}
$$

is simply the one-body density matrix of a system of spinless fermions for the spatial sector $\Gamma_{mn} = x_2 < x_3 \cdots x_m < x' \cdots x_n < x \cdots x_N$ ($m < n$, for example). And the spin part

$$
\begin{aligned}
S_{m,n}(\sigma',\sigma) &= (-1)^{(m-n)} \sum_{\sigma_2 \cdots \sigma_N} [(1 \cdots m)\chi^*] \, [(1 \cdots n)\chi] \\
&= (-1)^{(m-n)} \langle \chi | c_m^\dagger(\sigma')(m \cdots n)c_n(\sigma)|\chi\rangle ,
\end{aligned}
\tag{E.9}
$$

where $(m \cdots n)$ is the loop permutation operator(Appendix A), and $c_m^\dagger(\sigma)$ can be regarded as fermion (or hard core boson) creation operators, which is just a formal symbol to select out the spin states. The matrix element of $c_m^\dagger(\sigma')(m \cdots n)c_n(\sigma)$ between two spin bases $|f_1' f_2' \cdots f_N'\rangle$ and $|f_1 f_2 \cdots f_N\rangle$ is

$$
\begin{aligned}
&\langle f_1' \cdots f_N'| \, c_m^\dagger(\sigma')(m \cdots n)c_n(\sigma) \, |f_1 f_2 \cdots f_N\rangle \\
&= \langle f_1' \cdots f_N'| \, c_m^\dagger(\sigma') \, |f_1 \cdots f_m \cdots 0 \cdots f_N\rangle \, \delta_{f_n,\sigma} \\
&= \langle f_1' \cdots f_N'| \, c_m^\dagger(\sigma') \, |f_1 \cdots 0 f_m \cdots f_{n-1} \cdots f_N\rangle \, \delta_{f_n,\sigma} \\
&= \langle f_1' \cdots f_N'|f_1 \cdots \sigma' f_m \cdots f_{n-1} \cdots f_N\rangle \, \delta_{f_n,\sigma} \\
&= \delta_{f_m',\sigma'}\delta_{f_{m+1}',f_m}\delta_{f_{m+2}',f_{m+1}} \cdots \delta_{f_n',f_{n-1}}\delta_{f_n,\sigma} ,
\end{aligned}
\tag{E.10}
$$

where on the second and third line '0' is a placeholder for a spin 'annihilated' by $c_n(\sigma)$

Note that we have added a $(-1)^{(m-n)}$ sign in front of the spatial part of the OBDM $rho_{m,n}(x',x)$. This is to guarantee that if φ is strictly positive in spatial sector θ^1, $\rho_{m,n}(x',x)$ is strictly positive for any m and n. For Bosons, simply change the spin part of the OBDM to bosonic one by $S_{m,n}^B = (-1)^{m-n} S_{m,n}^F$.

Appendix F

Magnetic Gradient Term in Spin-Chain Model

When adding some single-particle terms into the original Hamiltonian, we need to calculate some other geometric constants. For example, if we consider the presence of a spin-dependent magnetic gradient, then the total Hamiltonian is given by

$$H = \sum_{i=1}^{N} \left[-\partial_i^2/2 + V(x_i) - G x_i \sigma_i^z \right] + g \sum_{i<j} \delta(x_{ij}) , \tag{F.1}$$

where G is the strength of the magnetic gradient. The corresponding spin chain Hamiltonian for the ground manifold(See Section 3.3) now takes the form

$$H_{\text{sc}}^{(0)} = E^{(0)} - \frac{1}{g} \sum_{i=1}^{N-1} C_i^{(0)} \left(1 \pm \mathcal{E}_{i,i+1} \right) - G \sum_{i=1}^{N} D_i^{(0)} \sigma_i^z , \tag{F.2}$$

where

$$D_i^{(0)} = N! \int dx_1 ... dx_N \, x_i |\varphi_0|^2 \theta^1, \quad i = 1, 2, ..., N \tag{F.3}$$

Here we would like to note an interesting relation between $C_i^{(0)}$ and $D_i^{(0)}$ for a harmonically trapped system. $D_i^{(0)}$ has a physical meaning of the average position of i'th particle, which naturally leads to a LDA expression:

$$D_i^{(0)} = \int_{y_{i-1}}^{y_i} dx \, x \, n_{\text{TG}}(x) = C_{i-1}^{(0)} - C_i^{(0)} , \tag{F.4}$$

where the physical meaning of y_i is the average boundary between particle i and $i + 1$(Eq. (C.4)). This relation can even be numerically proven to be true for exact $C_i^{(0)}$ and $D_i^{(0)}$ for arbitrary particle numbers N without envoking the LDA.

Bibliography

[1] T. Hahn, "Cuba - a library for multidimensional numerical integration," *Comput.Phys.Commun.*, vol. 168, pp. 78–95, 2005.

[2] F. Deuretzbacher, K. Fredenhagen, D. Becker, K. Bongs, K. Sengstock, and D. Pfannkuche, "Exact solution of strongly interacting quasi-one-dimensional spinor bose gases," *Phys. Rev. Lett.*, vol. 100, p. 160405, 2008.

[3] H. Bethe, "On the theory of metals. i. eigenvalues and eigenfunctions of the linear atom chain," *Zeitschrift für Physik,*, vol. 71, pp. 205–226, 1931.

[4] M. D. Girardeau, "Relationship between systems of impenetrable bosons and fermions in one dimension," *Journal of Mathematical Physics*, vol. 1, pp. 516–523, Nov 1960.

[5] T. Giamarchi, *Quantum physics in one dimension.* Oxford University Press, December 2003.

[6] E. H. Lieb and W. Liniger, "Exact analysis of an interacting bose gas. i. the general solution and the ground state," *Physical Review*, vol. 130, no. 4, pp. 1605–1616, 1963.

[7] M. Gaudin, "Un systeme a une dimension de fermions en interaction," *Physics Letters A*, vol. 24, no. 1, pp. 55 – 56, 1967.

[8] C. N. Yang, "Some exact results for the many-body problem in one dimension with repulsive delta-function interaction," *Physical Review Letters*, vol. 19, no. 23, pp. 1312–1315, 1967.

[9] X.-W. Guan, M. T. Batchelor, and C. Lee, "Fermi gases in one dimension: From bethe ansatz to experiments," *Rev. Mod. Phys.*, vol. 85, p. 1633, 2013.

[10] M. D. G. E. M. Wright and J. M. Triscari, "Ground-state properties of a one-dimensional system of hard-core bosons in a harmonic trap," *Physical Review A*, vol. 63, p. 033601, 2001.

[11] J. L. Hennessy and D. A. Patterson, "A new golden age for computer architecture," *Communications of the ACM*, vol. 62, pp. 48–60, Jan 2019.

[12] E. Haller, M. Gustavsson, M. Mark, J. Danzl, R. Hart, G. Pupillo, and H.-C. Nägerl, "Realization of an excited, strongly correlated quantum gas phase," *Science*, vol. 325, no. 5945, pp. 1224–1227, 2009.

[13] T. Kinoshita, T. Wenger, and D. Weiss, "Observation of a one-dimensional tonks-girardeau gas," *Science*, vol. 305, no. 5687, pp. 1125–1128, 2004.

[14] B. Paredes, A. Widera, V. Murg, O. Mandel, S. Fölling, I. Cirac, G. V. Shlyapnikov, T. W. Hänsch, and I. Bloch, "Tonks–girardeau gas of ultracold atoms in an optical lattice," *Nature*, vol. 429, pp. 277–281, May 2004.

[15] T. Cheon and T. Shigehara, "Realizing discontinuous wave functions with renormalized short-range potentials," *Physics Letters A*, vol. 243, no. 3, pp. 111 – 116, 1998.

[16] T. Cheon and T. Shigehara, "Fermion-boson duality of one-dimensional quantum particles with generalized contact interactions," *Physical Review Letters*, vol. 82, no. 12, pp. 2536–2539, 1999.

[17] M. Girardeau, H. Nguyen, and M. Olshanii, "Effective interactions, fermi-bose duality, and ground states of ultracold atomic vapors in tight de broglie waveguides," *Opt. Commun*, 2004.

[18] M. D. Girardeau, "Theory of spinor fermi and bose gases in tight atom waveguides," *Physical Review A*, vol. 70, no. 2, 2004.

[19] D. Muth, M. Fleischhauer, and B. Schmidt, "Discretized versus continuous models of p-wave interacting fermions in one dimension," *Physical Review A*, vol. 82, p. 013602, 2010.

[20] C. J. Pethick and H. Smith, *Bose–Einstein Condensation in Dilute Gases*. Cambridge University Press, 2008.

[21] C. Menotti and S. Stringari, "Collective oscillations of a one-dimensional trapped bose-einstein gas," *Physical Review A*, vol. 66, no. 4, 2002.

[22] L. Yang, L. Guan, and H. Pu, "Strongly interacting quantum gases in one-dimensional traps," *Phys. Rev. A*, vol. 91, p. 043634, 2015.

[23] B. Sutherland, "Model for a multicomponent quantum system," *Physical Review B*, vol. 12, no. 9, pp. 3795–3805, 1975.

[24] F. Deuretzbacher, D. Becker, J. Bjerlin, S. M. Reimann, and L. Santos, "Quantum magnetism without lattices in strongly interacting one-dimensional spinor gases," *Phys. Rev. A*, vol. 90, p. 013611, 2014.

[25] J. Levinsen, P. Massignan, G. M. Bruun, and M. M. Parish, "Strong-coupling ansatz for the one-dimensional fermi gas in a harmonic potential," *Science Advances*, vol. 1, p. e1500197, 2015.

[26] S. E. Gharashi and D. Blume, "Correlations of the upper branch of 1d harmonically trapped two-component fermi gases," *Phys. Rev. Lett.*, vol. 111, p. 045302, 2013.

[27] T. Fukuhara, Y. Takasu, M. Kumakura, and Y. Takahashi, "Degenerate fermi gases of ytterbium," *Physical Review Letters*, vol. 98, no. 3, 2007.

[28] M. K. Tey, S. Stellmer, R. Grimm, and F. Schreck, "Double-degenerate bose-fermi mixture of strontium," *Physical Review A*, vol. 82, no. 1, 2010.

[29] B. J. DeSalvo, M. Yan, P. G. Mickelson, Y. N. M. de Escobar, and T. C. Killian, "Degenerate fermi gas of ^{8}7sr," *Physical Review Letters*, vol. 105, no. 3, 2010.

[30] G. Pagano, M. Mancini, G. Cappellini, P. Lombardi, F. Schäfer, H. Hu, X.-J. Liu, J. Catani, C. Sias, M. Inguscio, and et al., "A one-dimensional liquid of fermions with tunable spin," *Nature Physics*, vol. 10, pp. 198–201, Feb 2014.

[31] X.-W. G. M. T. Batchelor and M. Takahashi, "Ferromagnetic behavior in the strongly interacting two-component bose gas," *Physical Review A*, vol. 76, no. 4, p. 043617, 2007.

[32] N. Oelkers, M. Batchelor, M. Bortz, and X. Guan, "Bethe ansatz study of one-dimensional bose and fermi gases with periodic and hard wall boundary conditions," *J. Phys. A*, vol. 39, pp. 1073–1098, 2006.

[33] T. Busch, B.-G. Englert, K. Rzażewski, and M. Wilkens, "Two cold atoms in a harmonic trap," *Foundations of Physics*, vol. 28, pp. 549–559, Apr 1998.

[34] M. Barth and W. Zwerger, "Tan relations in one dimension," *Annals of Physics*, vol. 326, no. 10, pp. 2544 – 2565, 2011.

[35] C. N. Yang and Y.-Z. You, "One-dimensionalw-component fermions and bosons with repulsive delta function interaction," *Chinese Physics Letters*, vol. 28, p. 020503, Feb 2011.

[36] M. Olshanii, "Atomic scattering in the presence of an external confinement and a gas of impenetrable bosons," *Physical Review Letters*, vol. 81, no. 5, pp. 938–941, 1998.

[37] T. Bergeman, "Atom-atom scattering under cylindrical harmonic confinement: Numerical and analytic studies of the confinement induced resonance," *Physical Review Letters*, vol. 91, no. 16, 2003.

[38] L. Guan and S. Chen, "Super-tonks-girardeau gas of spin-1/2 interacting fermions," *Phys. Rev. Lett.*, vol. 105, p. 175301, 2010.

[39] G. E. Astrakharchik, "Local density approximation for a perturbative equation of state," *Physical Review A*, vol. 72, no. 6, p. 063620, 2005.

[40] X. Cui and T.-L. Ho, "Ground-state ferromagnetic transition in strongly repulsive one-dimensional fermi gases," *Physical Review A*, vol. 89, no. 2, p. 023611, 2014.

[41] U. Schollwoeck, "The density-matrix renormalization group in the age of matrix product states," *Annals of Physics*, vol. 326, p. 96, 2011.

[42] G. Vidal, "Efficient classical simulation of slightly entangled quantum computations," *Physical Review Letters*, vol. 91, no. 14, 2003.

[43] M. Tezuka and M. Ueda, "Ground states and dynamics of population-imbalanced fermi condensates in one dimension," *New J. Phys.*, vol. 055029, 2010.

[44] M. L. Wall and L. D. Carr, "Open source tebd," 2009.

[45] D. McKay and B. DeMarco, "Thermometry with spin-dependent lattices," *New J. Phys. 12 055013 (2010)*, 11 2009.

[46] P. Soltan-Panahi, J. Struck, P. Hauke, A. Bick, W. Plenkers, G. Meineke, C. Becker, P. Windpassinger, M. Lewenstein, and K. Sengstock, "Multi-component quantum gases in spin-dependent hexagonal lattices," *Nature Physics*, vol. 7, pp. 434–440, Feb 2011.

[47] L. P. Pitaevskii and A. Rosch, "Breathing modes and hidden symmetry of trapped atoms in two dimensions," *Physical Review A*, vol. 55, no. 2, pp. R853–R856, 1997.

[48] F. Werner and Y. Castin, "Unitary gas in an isotropic harmonic trap: Symmetry properties and applications," *Physical Review A*, vol. 74, no. 5, 2006.

[49] Y. Nishida and D. T. Son, "Nonrelativistic conformal field theories," *Physical Review D*, vol. 76, no. 8, 2007.

[50] S. Moroz, "Scale-invariant fermi gas in a time-dependent harmonic potential," *Physical Review A*, vol. 86, no. 1, 2012.

[51] Z. D. Zhang, G. E. Astrakharchik, D. C. Aveline, S. Choi, H. Perrin, T. H. Bergeman, and M. Olshanii, "Breakdown of scale invariance in the vicinity of the tonks-girardeau limit," *Physical Review A*, vol. 89, p. 063616, 2014.

[52] F. N. C. Paraan and V. E. Korepin, "Perturbative correction to the ground-state properties of one-dimensional strongly interacting bosons in a harmonic trap," *Physical Review A*, vol. 82, no. 6, p. 065603, 2010.

[53] A. G. Volosniev, D. V. Fedorov, A. S. Jensen, M. Valiente, and N. T. Zinner, "Strongly interacting confined quantum systems in one dimension," *Nature Communications*, vol. 5, p. 5300, 2014.

[54] A. G. Volosniev, D. Petrosyan, M. Valiente, D. V. Fedorov, A. S. Jensen, and N. T. Zinner, "Engineering the dynamics of effective spin-chain models for strongly interacting atomic gases," *Phys. Rev. A*, vol. 91, p. 023620, 2015.

[55] J. Spalek, "t-j model then and now: A personal perspective from the pioneering times," *Acta Physica Polonica A*, vol. 111, pp. 409–24, 2007.

[56] F. Meinert, M. Knap, E. Kirilov, K. Jag-Lauber, M. B. Zvonarev, E. Demler, and H.-C. Nägerl, "Bloch oscillations in the absence of a lattice," *Science*, vol. 356, pp. 945–948, 2017.

[57] F. Deuretzbacher, D. Becker, and L. Santos, "Momentum distributions and numerical methods for strongly interacting one-dimensional spinor gases," *Phys. Rev. A*, vol. 94, p. 023606, 2016.

[58] J.-X. Zhu and Z. D. Wang, "Topological effects associated with fractional statistics in one-dimensional mesoscopic rings," *Physical Review A*, vol. 53, no. 1, pp. 600–603, 1996.

[59] M. D. Girardeau, "Anyon-fermion mapping and applications to ultracold gases in tight waveguides," *Physical Review Letters*, vol. 97, p. 100402, 2006.

[60] P. Calabrese and M. Mintchev, "Correlation functions of one-dimensional anyonic fluids," *Phys.Rev.B*, vol. 75, p. 233104, 2007.

[61] R. Santachiara, F. Stauffer, and D. C. Cabra, "Entanglement properties and momentum distributions of hard-core anyons on a ring," *Journal of Statistical Mechanics: Theory and Experiment*, vol. 2007, pp. L05003–L05003, May 2007.

[62] R. Santachiara and P. Calabrese, "One-particle density matrix and momentum distribution function of one-dimensional anyon gases," *J. Stat.*, vol. Mech., p. P06005, 2008.

[63] A. Kundu, "Exact solution of double-delta function bose gas through interacting anyon gas," *Phys.Rev.Lett.*, vol. 83, pp. 1275–1278, 1999.

[64] M. Batchelor, X.-W. Guan, and N. Oelkers, "The 1d interacting anyon gas: low-energy properties and haldane exclusion statistics," *Phys. Rev. Lett.*, vol. 96, p. 210402, 2006.

[65] M. T. Batchelor and X. W. Guan, "Generalized exclusion statistics and degenerate signature of strongly interacting anyons," *Phys. Rev. B*, vol. 74, p. 195121, 2006.

[66] M. Batchelor, X.-W. Guan, and J.-S. He, "Bethe ansatz for 1d interacting anyons," *J. Stat.*, vol. Mech., p. P03007, 2007.

[67] M. Batchelor and X.-W. Guan, "Fermionization and fractional statistics in the strongly interacting one-dimensional bose gas," *Laser Phys. Lett.*, vol. 4, p. 77,

2007.

[68] O. I. Patu, V. E. Korepin, and D. V. Averin, "Correlation functions of one-dimensional lieb-liniger anyons," *J. Phys. A: Math. Theor.*, vol. 40, pp. 14963–14984, 2007.

[69] O. I. Patu, V. E. Korepin, and D. V. Averin, "One-dimensional impenetrable anyons in thermal equilibrium. i. anyonic generalization of lenard's formula," *J. Phys. A: Math. Theor.*, vol. 41, p. 145006, 2008.

[70] O. I. Patu, V. E. Korepin, and D. V. Averin, "One-dimensional impenetrable anyons in thermal equilibrium. ii. determinant representation for the dynamic correlation functions," *J. Phys. A: Math. Theor.*, vol. 41, p. 255205, 2008.

[71] O. I. Patu, V. E. Korepin, and D. V. Averin, "One-dimensional impenetrable anyons in thermal equilibrium. iii. large distance asymptotics of the space correlations," *J. Phys. A: Math. Theor.*, vol. 42, p. 275207, 2009.

[72] O. I. Patu, V. E. Korepin, and D. V. Averin, "One-dimensional impenetrable anyons in thermal equilibrium. iv. large time and distance asymptotic behavior of the correlation functions," *J. Phys. A: Math. Theor.*, vol. 43, p. 115204, 2010.

[73] M. Rigol and A. Muramatsu, "Universal properties of hard-core bosons confined on one-dimensional lattices," *Phys. Rev. A*, vol. 70, p. 031603(R), 2004.

[74] M. Rigol and A. Muramatsu, "Ground-state properties of hard-core bosons confined on one-dimensional optical lattices," *Phys. Rev. A*, vol. 72, p. 013604, 2005.

[75] T. M. Wright, M. Rigol, M. J. Davis, and K. V. Kheruntsyan, "Nonequilibrium dynamics of one-dimensional hard-core anyons following a quench: Complete relaxation of one-body observables," *Phys. Rev. Lett.*, vol. 113, p. 050601, 2014.

[76] Y. Hao, Y. Zhang, and S. Chen, "Ground-state properties of one-dimensional anyon gases," *Phys. Rev. A*, vol. 78, p. 023631, 2008.

[77] Y. Hao, Y. Zhang, and S. Chen, "Ground-state properties of hard-core anyons in one-dimensional optical lattices," *Phys. Rev. A*, vol. 79, p. 043633, 2009.

[78] Y. Hao, "Ground state properties of hard-core anyons in a harmonic potential," *Phys. Rev. A*, vol. 93, p. 063627, 2016.

[79] Y. Hao and Y. Song, "One-dimensional hard-core anyon gas in a harmonic trap at finite temperature," *The European Physical Journal D*, vol. 71, p. 135, Jun 2017.

[80] G. Marmorini, M. Pepe, and P. Calabrese, "One-body reduced density matrix of trapped impenetrable anyons in one dimension," *J. Stat.*, vol. Mech., p. 073106, 2016.

[81] T. Papenbrock, "Ground-state properties of hard core bosons in one-dimensional harmonic traps," *Phys. Rev. A*, vol. 67, p. 041601(R), 2003.

[82] P. J. Forrester, N. E. Frankel, T. M. Garoni, and N. S. Witte, "Finite one-dimensional impenetrable bose systems: Occupation numbers," *Physical Review A*, vol. 67, p. 043607, 2003.

[83] G. Vidal, "Classical simulation of infinite-size quantum lattice systems in one spatial dimension," *Phys. Rev. Lett.*, vol. 98, p. 070201, 2007.

[84] J. A. Kjäll, M. P. Zaletel, R. S. K. Mong, J. H. Bardarson, and F. Pollmann, "The phase diagram of the anisotropic spin-2 xxz model: an infinite system dmrg study," *Phys. Rev. B*, vol. 87, p. 235106, 2013.

[85] G. A. Fiete, "The spin-incoherent luttinger liquid," *Rev. Mod. Phys.*, vol. 79, p. 801, 2007.

[86] M. Ogata and H. Shiba, "Bethe-ansatz wave function, momentum distribution, and spin correlation in the one-dimensional strongly correlated hubbard model," *Physical Review B*, vol. 41, no. 4, pp. 2326–2338, 1990.

[87] V. V. Cheianov, H. Smith, and M. B. Zvonarev, "Low-temperature crossover in the momentum distribution of cold atomic gases in one dimension," *Physical Review A*, vol. 71, p. 033610, 2005.

[88] A. Imambekov and E. Demler, "Applications of exact solution for strongly interacting one dimensional bose-fermi mixture: low-temperature correlation functions, density profiles and collective modes," *Ann. Phys.*, vol. 321, p. 2390, 2006.

[89] N. J. S. Loft, O. V. Marchukov, D. Petrosyan, and N. T. Zinner, "Tunable self-assembled spin chains of strongly interacting cold atoms," *New J. Phys.*, vol. 18, p. 045011, 2016.

[90] N. J. S. Loft, L. B. Kristensen, A. E. Thomsen, A. G. Volosniev, and N. T. Zinner, "Conan – the cruncher of local exchange coefficients for strongly interacting confined systems in one dimension," *Computer Physics Communications*, vol. 209, pp. 171–182, 2016.

[91] L. Yang and H. Pu, "Bose-fermi mapping and multi-branch spin chain model for strongly interacting quantum gases in one-dimension: Dynamics and collective excitations," *Phys. Rev. A*, vol. 94, p. 033614, 2016.

[92] D. Gangardt and A. Kamenev, "Bloch oscillations in one-dimensional spinor gas," *Phys. Rev. Lett.*, vol. 102, p. 070402, 2009.

[93] M. Schecter, D. Gangardt, and A. Kamenev, "Dynamics and bloch oscillations of mobile impurities in one-dimensional quantum liquids," *Annals of Physics 327 (2012), pp. 639-670*, 05 2011.

[94] O. Gamayun, O. Lychkovskiy, and V. Cheianov, "Kinetic theory for a mobile impurity in a degenerate tonks-girardeau gas," *Phys. Rev. E*, vol. 90, p. 032132, 2014.

[95] M. Schecter, D. M. Gangardt, and A. Kamenev, "Quantum impurities: from mobile josephson junctions to depletons," *New J. Phys.*, vol. 18, p. 065002, 2016.

[96] M. Abadi, A. Agarwal, P. Barham, E. Brevdo, Z. Chen, C. Citro, G. S. Corrado, A. Davis, J. Dean, M. Devin, S. Ghemawat, I. Goodfellow, A. Harp, G. Irving, M. Isard, Y. Jia, R. Jozefowicz, L. Kaiser, M. Kudlur, J. Levenberg, D. Mané, R. Monga, S. Moore, D. Murray, C. Olah, M. Schuster, J. Shlens, B. Steiner, I. Sutskever, K. Talwar, P. Tucker, V. Vanhoucke, V. Vasudevan, F. Viégas, O. Vinyals, P. Warden, M. Wattenberg, M. Wicke, Y. Yu, and X. Zheng, "TensorFlow: Large-scale machine learning on heterogeneous systems," 2015. Software available from tensorflow.org.

[97] G. Carleo and M. Troyer, "Solving the quantum many-body problem with artificial neural networks," *Science*, vol. 355, p. 602, 2017.

[98] G. Hinton and R. Salakhutdinov, "Reducing the dimensionality of data with neural networks," *Science*, vol. 313, no. 5786, pp. 504–507, 2006.

[99] M. Á. Carreira-Perpiñán and G. E. Hinton, "On contrastive divergence learning," in *AISTATS*, 2005.

[100] For strongly interacting spinor Bose gases, all conclusions are the same except for a few sign changes [22, 101].

[101] L. Yang and H. Pu, "One-body density matrix and momentum distribution of strongly interacting one-dimensional spinor quantum gases," *Phys. Rev. A*, vol. 95, p. 051602, 2017.

[102] F. Deuretzbacher, D. Becker, J. Bjerlin, S. M. Reimann, and L. Santos, "Spin-chain model for strongly interacting one-dimensional bose-fermi mixtures," *Phys. Rev. A*, vol. 95, p. 043630, 2017.

[103] S_r is calculated by averaging the starting index m in $S_{m,m+r}$ by $S_r = 1/N \sum_m S_{m,m+r}$.

[104] K. A. Matveev, "Conductance of a quantum wire at low electron density," *Physical Review B*, vol. 70, no. 24, p. 245319, 2004.

[105] K. A. Matveev and A. Furusaki, "Spectral functions of strongly interacting isospin-1/2 bosons in one dimension," *Phys. Rev. Lett.*, vol. 101, p. 170403, 2008.